MODELING THE DYNAMICS OF OFFSHORE TIDAL SAND RIDGES

Bing Yuan

Bing Yuan

Institute for Marine and Atmospheric research Utrecht (IMAU)
Utrecht University
Princetonplein 5, 3584 CC Utrecht

PhD thesis, the Netherlands, 2017
The cover of the thesis was made based on the bathymetry data of the northwest European shelf seas obtained by using GeoMapApp.

ISBN: 978-90-393-6800-8

Printing: Ipskamp printing

MODELING THE DYNAMICS OF OFFSHORE TIDAL SAND RIDGES

Modelleren van de dynamica van getijde(zand)banken op het continentale plat

(met een samenvatting in het Nederlands)

Proefschrift

ter verkrijging van de graad van doctor aan de Universiteit Utrecht op gezag van de rector magnificus, prof.dr. G.J. van der Zwaan, ingevolge het besluit van het college voor promoties in het openbaar te verdedigen op

maandag 3 juli 2017 des middags te 4.15 uur

door

BING YUAN

geboren op 10 september 1987
te Xiaogan, China

PROMOTOR: Prof. dr. H.E. de Swart

This thesis was accomplished with financial support from China Scholarship Council (No. 201206250029).

CONTENTS

1

INTRODUCTION

This thesis focuses on linear and nonlinear dynamics of tidal sand ridges in the offshore area of shelf seas. In this chapter, first, in Section 1.1 the general geographical and physical aspects of shelf seas are introduced. Next, in Section 1.2 the characteristics of observed tidal sand ridges are described, followed by the motivation of research on these bedforms in Section 1.3. In Section 1.4, a brief review of previous studies on the dynamics of the bedforms is given. Last, in Section 1.5 the research questions are formulated and in Section 1.6 the outline of the thesis is presented.

1.1 GEOGRAPHICAL AND PHYSICAL ASPECTS OF SHELF SEAS

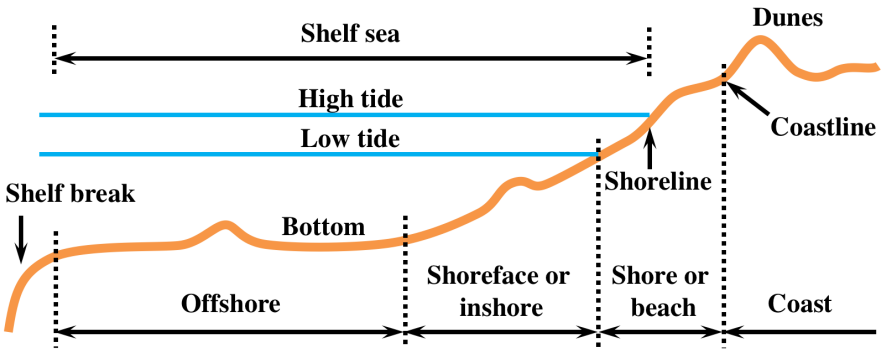

Figure 1.1: Sketch of a shelf sea. Modified after Shore Protection Manual (1984).

A shelf sea is a body of water, with depths of 0–200 m, which extends from the shoreline to the seaward end of the continental shelf, the shelf break. The latter marks

the beginning of the continental slope (average slope of order 0.1) that separates the shelf from the deep ocean (depths of several kilometers). Fig. 1.1 shows a sketch of a shelf sea. Examples of shelf seas are the East China Sea, located east of China, and the Celtic Sea off the south coast of Ireland. Semi-enclosed shelf seas also exist, e.g. the North Sea, which is bordered by Great Britain, Scandinavia, Germany, the Netherlands, Belgium, and France. Although shelf seas take up only approximately 8% of the total surface area of the world oceans (Yool and Fasham, 2001), they are of great value from both social and economic perspectives, and they play an important role in marine ecosystems and ocean dynamics (Simpson and Sharples, 2012). For instance, shelf seas are used for recreation and transportation, they provide natural resources such as oil, gas and minerals, and they are important regions for primary production from phytoplankton and for dissipation of tidal energy and wave energy.

Shelf seas are highly dynamic due to the joint presence of tides, waves and bottom changes in these waters. Often, shelf seas are divided into three parts (Fig. 1.1), i.e., the shore area (between the coastline and the water level of low tide), the shoreface or inshore area (cross-shore slopes of order 0.01 to 0.001) and the offshore area (cross-shore slopes less than 0.001). In the first two areas, typically wind generated surface waves with periods of order 10 seconds dominate the water motion, while tides induce changes in the water level on a time scale of several hours. In the offshore area, tides become more important while waves still play a role.

In shelf seas with a sandy bed, a variety of rhythmic bottom patterns are observed, with spacings λ (mean distance between successive crests) ranging from several decimeters to tens of kilometers. In the shore area, ripples with λ of order 10 cm, megaripples with λ of order 10 m and beach cusps with λ ranging between 1 and 100 m (Nelson and Voulgaris, 2015; Gallagher, 2011; van Gaalen et al., 2011, and references therein) are observed. In the shoreface area, besides ripples and megaripples, sand bars and sand waves with λ of order 100 m, and shoreface-connected sand ridges with λ ranging between 2 km and 10 km (Price et al., 2014; van Santen et al., 2011; Nnafie et al., 2014a, and references therein) occur. In the offshore area, megaripples and sand waves are still present. In addition, two types of large-scale bedforms occur, i.e., long bed waves with λ of 1–3 km (Knaapen et al., 2001; van Dijk et al., 2011) and tidal sand ridges with λ between 5–20 km (Off, 1963; Liu et al., 1998; Dyer and Huntley, 1999, and references therein).

1.2 CHARACTERISTICS OF OBSERVED TIDAL SAND RIDGES

As the focus of this thesis is on the dynamics of tidal sand ridges, some more details about these bedforms are presented here. Fig. 1.2 shows where they occur in the southern North Sea. Generally, tidal sand ridges have crests that are 5°–30° cycloni-

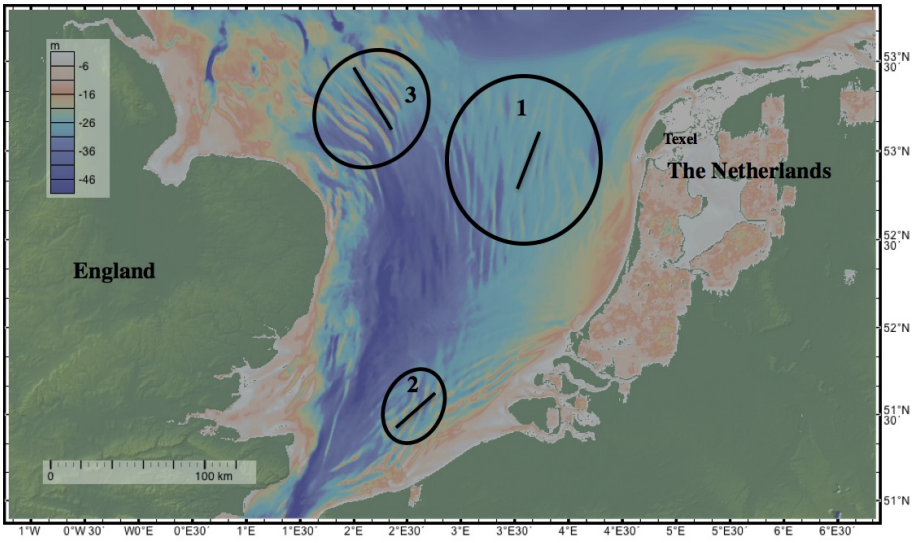

Figure 1.2: Bathymetry of the southern North Sea. The black circles indicate the areas where tidal sand ridges are located: 1) the Dutch Banks, 2) the Flemish Banks, and 3) the Norfolk Banks. Black lines inside the circles qualitatively indicate the principal direction of the tidal current based on Davies and Furnes (1980). The map is obtained using GeoMapApp (Ryan et al., 2009).

cally (clockwise in the Northern Hemisphere) rotated with respect to the principal direction of the tidal current (see Fig. 1.2), their height is in the order of 10 m, and they evolve on time scales of centuries. Although most of the observed ridges have nearly straight crest lines, ridges with meandering crest lines occur (e.g. in the region of the Norfolk Banks in Fig. 1.2). Both symmetrical and asymmetrical cross-crest (or

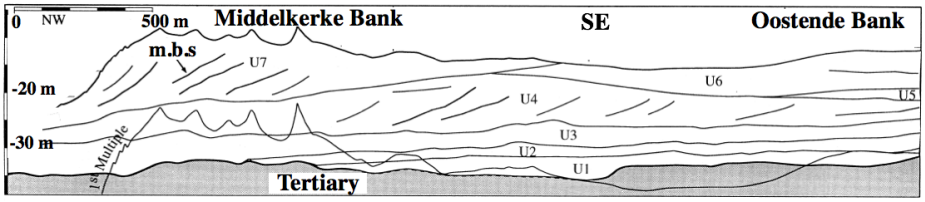

Figure 1.3: A cross-crest seismic profile (in the southeast direction, SE) of the Middelkerke Bank in the region of the Flemish Banks, after Trentesaux et al. (1999). The gray layer represents (solid) Tertiary (from 66 million to 2.6 million years ago) deposits and layers above are the (unconsolidated) Quaternary (from 2.6 million years ago to the present) deposits. The medium bounding surfaces (m.b.s, distinguishable from separation between layers of material of different sizes and densities) suggest that the ridge migrates to the northwest (NW).

cross-sectional) profiles of these ridges are detected. Here, the symmetry refers to the position of the crests. Asymmetrical ridge profiles indicate migration of the ridges in the direction of the crest towards the steepest slope. Fig. 1.3 shows an example of an asymmetrical cross-sectional profile of observed ridges in the region of the Flemish Banks, which suggests that the ridges migrate northwest. Small-scale bedforms with a spacing of order 100 m superimposed on the ridge are also identified. Over tidal sand ridges, variation of the surficial grain size is observed: usually the sediment at the crests (in the case of symmetrical profiles) or at the steeper sides (in the case of asymmetrical profiles) is coarser than that at the other parts of the ridges (Roos et al., 2007, and references therein).

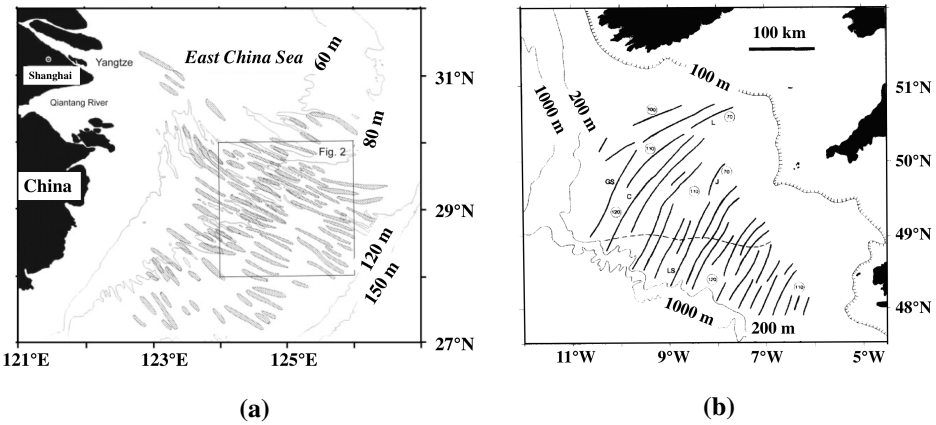

Figure 1.4: Tidal sand ridges in (a) the East China Sea (indicated by gray bars, reprinted from Liu et al., 2007) and (b) the Celtic Sea (indicated by thick continuous lines, reprinted from Belderson et al., 1986).

Tidal sand ridges occur in a wide range of water depths, for instance, the southern North Sea (20–40 m), the East China Sea (60–120 m, Fig. 1.4a) and the Celtic Sea (120–170 m, Fig. 1.4b). According to their present-day morphodynamic activity, ridges are classified as 'active', 'quasi-active' and 'moribund'. Active and moribund mean that sand transport is, respectively, present and absent in the entire area where the ridges occur, and quasi-active means that sand transport occurs in only part of the ridge area. Generally, active ridges are found in relatively shallow waters (10–50 m) where strong tidal currents occur (typically above 0.5 m/s), e.g., in the southern North Sea (Kenyon et al., 1981). In contrast, moribund ridges are observed in relatively deep waters (100–200 m) where tidal currents are weak (maximum velocity is insufficient to move the sand near bed), e.g., in the Celtic Sea (Stride et al., 1982), or in areas with limited availability of sand (limited thickness of the erodible bed). In shelf seas where the water depth and the current strength are between

those for active and moribund ridges, such as the East China Sea (Liu et al., 2007), quasi-active ridges occur. Usually active/quasi-active ridges have asymmetrical cross-sectional profiles, and smaller-scale bedforms such as sand waves are superimposed on them (see e.g. Fig. 1.3), while moribund ridges have almost symmetrical cross-sectional profiles and no small-scale bedforms superimposed on them.

1.3 MOTIVATION OF THIS STUDY

There are several reasons to explore the dynamics of tidal sand ridges. First, due to increasing demand of sand in human activities, such as land reclamation, beach nourishment and construction works, offshore large-scale bedforms are considered as potential sand resources for marine sand mining (Velegrakis et al., 2010). An example is sand mining from the Kwinte Bank (belonging to the Flemish Banks) on the Belgian Continental Shelf (Degrendele et al., 2010). Second, it should be noted that these bedforms provide habitats for marine organisms (van Dijk et al., 2012), while removal of sand will change the local environment and thereby have an impact on those organisms (van Dalfsen et al., 2000; Boyd et al., 2005; Kubicki et al., 2007). Third, these offshore bedforms dissipate wave energy during storms and thereby protect the coast (see e.g. Spencer et al., 2015). Moreover, active bedforms may cause damage to the underwater structures such as pipelines, telecommunication cables and electricity cables from offshore windmill parks (Roebert, 2014). Hence, knowledge of these seabed features and their dynamics is desirable for practical issues, such as strategic planning of marine sand mining (van Lancker et al., 2010), maintaining the balance of the marine ecosystem and assessment of the stability of underwater structures.

1.4 PRESENT KNOWLEDGE OF DYNAMICS OF TIDAL SAND RIDGES

1.4.1 *Initial formation of tidal sand ridges*

Generally there are two types of theories for the initial formation of tidal sand ridges (Pattiaratchi and Collins, 1987; Dyer and Huntley, 1999, and references therein). The first one is that ridges form directly due to local hydrodynamical or geological conditions. It means that ridges occur as a result of spatial variations in hydrodynamical conditions such as presence of secondary flow (see e.g. Off, 1963; Houbolt, 1968), or that ridges are generated during the post-glacial sea level rise in the presence of a relict core of sediment (see e.g. Berné et al., 1994, 1998). The second type of theory is based on the concept that ridges form due to positive feedbacks between water motion and erodible bed (through sand transport), i.e., morphodynamic self-organization (Blondeaux, 2001; Dodd et al., 2003; Coco and Murray, 2007, and re-

ferences therein). Small-amplitude bedforms can spontaneously grow, because they influence water motion in such a way that net convergence of sand transport takes place in the crest areas. It has been demonstrated in many studies that the latter theory is able to explain the formation of the other bedforms mentioned in Section 1.1. Compared to the first type of theories, the self-organization theory yields better explanations of many observed tidal sand ridges, so in this thesis, only the latter is considered.

To apply the self-organization theory to tidal sand ridges, the stability of a basic state is investigated, characterized by a spatially uniform tidal current (background tidal current) over a flat horizontal bed, with respect to bottom perturbations with small amplitudes. The latter consist of bottom modes, which are Fourier modes with arbitrary wavelength and orientation with respect to the principal current direction. A linear stability analysis concerns the initial behavior of the basic state. As initially the amplitude of the perturbation is small, the bottom modes evolve independently of each other, and their amplitudes grow or decay exponentially. The mode that grows fastest in the amplitude is called the fastest growing mode or the preferred mode/-bedform, which is expected to dominate the pattern of the bedform after some time.

Huthnance (1982a) was the first to apply the self-organization theory to the initial formation of tidal sand ridges by using linear stability analysis. He used depth-averaged shallow water equations for the tidal current, a bottom evolution equation that follows from mass conservation of sand, together with a simple sand transport formulation (cubic in velocity, including correction for favored downslope transport). He further assumed the background tidal current to be a block flow (constant flood current and constant ebb current) and neglected the Coriolis force. It turns out that linear stability analysis yields a wavelength λ_p and an orientation ϑ_p of the initially preferred bedform that are in fair agreement with those of observed ridges. Fig. 1.5 shows the contour plot of the dimensionless growth rate Γ of the bottom modes as a function of topographic wavenumber k and the angle ϑ between the principal current direction and the crests obtained in Huthnance (1982a). The reciprocal Γ^{-1} of the growth rate represents the e-folding growth time of the amplitude of the modes. The mode with the maximum growth rate corresponds to a bedform of which the spacing is 7.5 km (in a water depth of 30 m) and the angle between the crest and the principal current direction is 28°.

The results of Huthnance (1982a) reveal that the crucial aspect for the initial formation of tidal sand ridges is the deflection of the tidal current such that net accumulation of sand occurs above the crests. The deflection of the current is the result of the joint action of the background tidal current and the residual current that is generated by tide-topography interaction (see Zimmerman, 1980, 1981; Robinson, 1981). The sources of the residual current are frictional torques and (when accounted for) Coriolis torques that result from tidal flow moving over an uneven bottom.

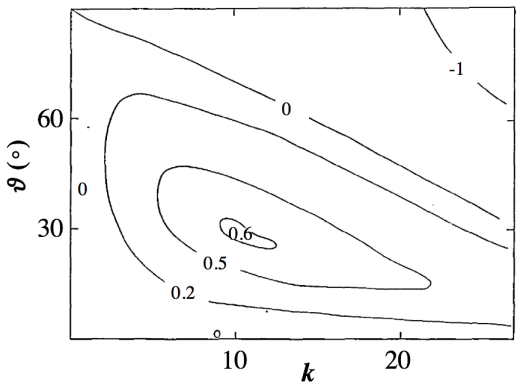

Figure 1.5: Contour plot of the dimensionless growth rate Γ of the bottom modes as a function of the dimensionless topographic wavenumber k and the angle ϑ between the principal current direction and the crests, from Huthnance (1982a). The growth rate is scaled by a typical morphological time scale of about 150 yr, and the wavenumber is scaled by a length scale of about 10 km. The Coriolis force was neglected and the plot is symmetric about $\vartheta = 0$.

Growing ridges have residual currents that always act with the background tidal current on the upstream side of the crest and act against the background tidal current on the downstream side. Consequently, more sand is transported towards the crest than that is transported away from the crest. Furthermore, Huthnance demonstrated that if the tidal current is symmetrical, i.e., the strength of flood and ebb is equal, sand accumulates exactly at the crests of the ridges. In contrast, if the current is asymmetrical, e.g. flood dominant (the maximum flood current is larger than the maximum ebb current), sand accumulates in the dominant current direction with respect to the crest, thereby affecting the growth of the ridges and causing the ridges to migrate.

After Huthnance (1982a), several other studies were conducted on the initial formation of tidal sand ridges. Instead of using a block flow, Hulscher et al. (1993) employed a background tidal current that is smooth, a semidiurnal lunar M_2 tidal current, which is the dominant tidal constituent in most shelf seas. In the case of a rectilinear tidal current (the end point of the velocity vector moves in a straight line in a tidal cycle), they obtained bedforms with a wavelength and an orientation that agree well with those of tidal sand ridges. Carbajal and Montaño (2001) explored the sensitivity of the wavelength λ_p and orientation ϑ_p of the initially preferred bedform to the initial water depth H_0 and the velocity amplitude of the tidal current U_0. By modifying the values of the parameters (H_0 and U_0) separately, they showed that λ_p increases as H_0 increases, and it also increases as U_0 increases. Roos et al. (2001) and Walgreen et al. (2002) imposed several rectilinear tidal constituents (residual current M_0, semidiurnal tide M_2 and quarter-diurnal tide M_4) to study the effect of asymmetrical tidal currents on the characteristics (migration rate, growth rate, wavelength and orientation) of tidal sand ridges. They confirmed the finding

in Huthnance (1982a) that the ridges migrate in the presence of asymmetrical tidal currents. Walgreen et al. (2004) and Roos et al. (2007) took into account the effect of grain sorting (spatial distribution of different grain sizes) over tidal sand ridges during their initial formation. Their results explain most of the observed grain size variation over the ridges. Blondeaux et al. (2009) considered elliptical tidal currents (horizontally the end point of the current velocity vector traces out an ellipse in a tidal cycle) and a formulation of sand transport that includes the critical shear stress for sand erosion (Miller et al., 1977, and references therein) and anisotropic bottom slope-induced sand transport (Talmon et al., 1995). They demonstrated that, under the conditions that the tidal current is elliptical and the maximum current velocity is just above the threshold for sand erosion, both tidal sand ridges and long bed waves emerge.

In the works mentioned above, depth-averaged tidal currents were used based on the fact that the water depth is much smaller than the horizontal scale of tidal sand ridges. The vertical flow structure was accounted for in Hulscher (1996) and Besio et al. (2006). In these studies, the initial formation of both tidal sand ridges and tidal sand waves was explained, and it was shown that including the vertical flow structure is necessary for the formation of tidal sand waves.

In the above cited studies, several simplifications in the bed shear stress, tidal forcing and the sand transport were observed. First, a linearized bed shear stress was employed (except in Besio et al., 2006; Blondeaux et al., 2009). Second, the tidal forcing employed was simple, i.e., only one tidal constituent was used or only rectilinear tidal currents were considered. In reality, in the horizontal plane tidal currents are elliptical rather than rectilinear (see e.g. Davies and Furnes, 1980). Moreover, they are composed of several other principal tidal constituents, such as the diurnal tide K_1 and the semidiurnal solar tide S_2, which together with M_2 give rise to a mixed semidiurnal tide and a spring-neap tide (Pugh, 1996), respectively. Third, the formulations of sand transport used in these studies were highly simplified, i.e., the threshold of sand erosion was neglected and isotropic bottom slope-induced sand transport was used (except in Besio et al., 2006; Blondeaux et al., 2009).

1.4.2 *Finite-height behavior of tidal sand ridges*

To study the characteristics of tidal sand ridges with a finite height, a nonlinear stability analysis is needed. In Huthnance (1982a), besides the initial formation of tidal sand ridges, finite-height equilibrium ridges were shown to exist, but rather strong simplifications were made. In his model, the topography only varied in one horizontal direction (1D configuration), the tidal current was modeled as a block flow, and the Coriolis force was neglected. Also, it was not shown how the ridges emerge in the course of time. Ridges only remained submerged in the case that either stirring of sand by surface waves, asymmetrical tidal currents or limited availability of sand

was considered. It was also shown that asymmetrical tidal currents give rise to asymmetrical equilibrium ridge profiles, and that the ridges migrate in the direction from their gentler side to their steeper side with respect to the crests.

The long-term evolution of topographies that varied in two horizontal dimensions (2D configuration) was investigated in Huthnance (1982b) by solving the vorticity equation (to obtain the current velocity) and the equation of bottom evolution numerically. The near-parallel depth contours in the equilibrium state for a single initial bump bottom perturbation suggested that arbitrarily long straight ridges would form in an infinite sea under spatially uniform tidal forcing. Note that the same simplifications in the forcing as those in Huthnance (1982a) were used, and the equilibrium state was only obtained under the condition of limited availability of sand.

Using a two-dimensional vertical model (2DV model) that accounts for currents in the vertical and one horizontal directions, Komarova and Newell (2000) investigated the nonlinear interaction between tidal sand waves with crests normal to the principal current direction and different wavelengths. They found that the nonlinear interaction between sand waves could generate bedforms with spacings similar to those of tidal sand ridges. However, the crests of the bedforms generated from the interaction between tidal sand waves were normal to the principal current direction, which are different from those of the observed ridges. Idier and Astruc (2003) determined the saturation height of tidal sand ridges by the growth rate of the initially

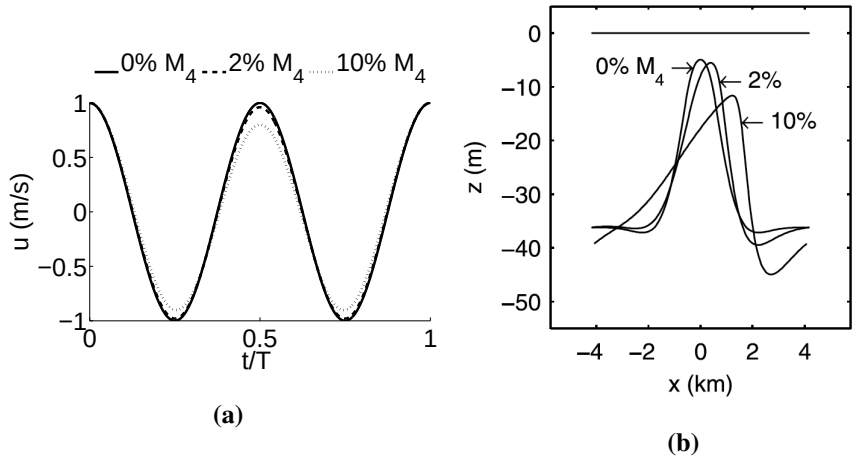

Figure 1.6: After Roos et al. (2004), (a) time evolution of velocity u of background symmetrical M_2 (solid line) and asymmetrical $M_2 + M_4$ (dashed and dotted lines, flood dominant) tidal currents in a tidal period T, the sum of the amplitudes of the currents is $U_{M_2} + U_{M_4} = U =$ 1 m/s and the percentage indicates U_{M_4}/U, and (b) modeled cross-sectional ridge profiles using bed load and the tidal currents in (a).

preferred bottom mode with different initial heights subject to a steady flow or a block flow. If the growth rate of the bottom mode with a certain height is zero, the ridge height is said to be saturated. In this way, the nonlinear interactions between bottom modes with different spacings were neglected, and the cross-sectional ridge profiles in time could not be obtained.

In Roos et al. (2004), a nonlinear morphodynamic model using a 1D configuration was presented and used to simulate the time evolution of the cross-sectional profiles of finite-height tidal sand ridges, and stirring of sand by wind waves was parametrically accounted for. In that study, unlike Huthnance (1982a,b), a rectilinear tidal current rather than a block flow was employed and unlimited availability of sand was assumed. Equilibrium ridges were shown to exist, and they were asymmetrical and migrated in the case of asymmetrical tidal currents (consisting of a semidiurnal tide M_2 together with either a residual current M_0 or an overtide M_4). Fig. 1.6 shows the symmetrical and asymmetrical (flood dominant) tidal currents used by Roos et al. (2004) and the modeled cross-sectional ridge profiles in their study. The ridges with asymmetrical profiles migrate in the flood direction (positive x-direction). It was also found that the modeled ridge height overestimated the observed ridge height of the Dutch Banks in the southern North Sea.

Using a 2DV model that accounts for interactions between sand ridges and sand waves, Tambroni and Blondeaux (2008) carried out a weakly nonlinear stability analysis to investigate the behavior of finite-height ridges. Their method is fast, but it is only applicable for tidal currents with large ellipticity ϵ (the ratio between the minor axis and the major axis of the tidal ellipse). Many tidal sand ridges are actually observed at locations where tidal currents are close to rectilinear ($\epsilon \sim 0$), for instance, in the southern North Sea (Collins et al., 1995). Interestingly, this study is the only one in which the effect of the critical bed shear stress for sand erosion on the evolution of finite-height ridges has been considered.

In the studies for the nonlinear evolution of tidal sand ridges mentioned above, the sea level and the characteristics of the background tidal current were kept constant in time. However, these bedforms evolve on a time scale of many hundreds of years, during which both the sea level and the characteristics of the tidal current change. Fig. 1.7 shows the time evolution of local sea level in the southern North Sea (Beets and van der Spek, 2000) and that of the eustatic (opposed to local) sea level (Fleming et al., 1998). It is seen from Fig. 1.7a that the sea level for the continental shelves of Belgium and the Netherlands at 8 ka BP (8000 years before present) was about 15 m lower than the present sea level. At the Last Glacial Maximum lowstand, the eustatic sea level was 125 ± 5 m lower than that in the present day (Fig. 1.7b). As the growth rate of the height of the ridges is in the same order of the rate of SLR, it is to be expected that SLR plays a role in the long-term evolution of these ridges. It seems plausible that present-day quasi-active/moribund ridges were initially formed during a low sea level (e.g., around 20 ka BP for ridges in the Celtic Sea), and sub-

sequently became less active or inactive as the sea level rose (Belderson et al., 1986; Yang, 1989; Scourse et al., 2009).

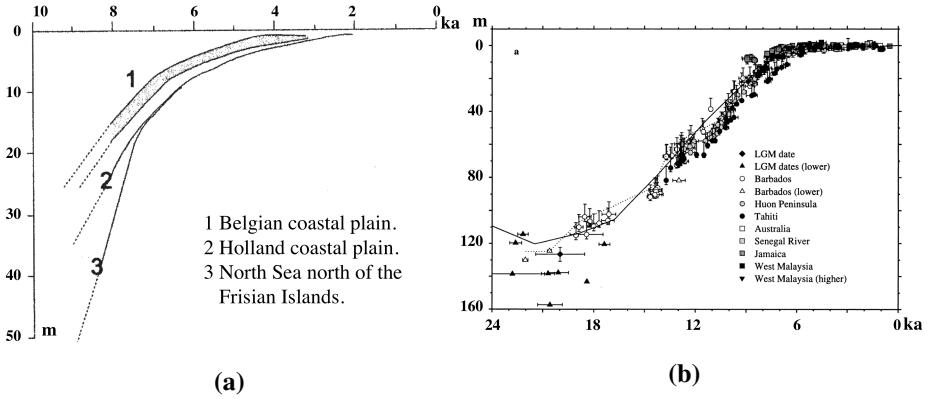

Figure 1.7: (a) Sea level rise in the southern North Sea during the Holocene, curve 1 is plotted as an envelope, after Beets and van der Spek (2000). (b) Estimated eustatic sea level from the Last Glacial Maximum to the present (solid line) from models, after Fleming et al. (1998).

Regarding the tidal current, van der Molen and de Swart (2001a) showed that during the Holocene period large variations of tidal conditions occurred in the southern North Sea. Fig. 1.8 shows modeled M_2 tidal current in the northwest European shelf sea from the Last Glacial Maximum to the present (Uehara et al., 2006), in which significant changes in the amplitude of the M_2 current were observed in the Celtic Sea. Since the strength of the tidal current determines the sand transport rate and the principal current direction affects the ridge orientation, variation in the strength and principal direction of the current also affects the evolution of the ridges.

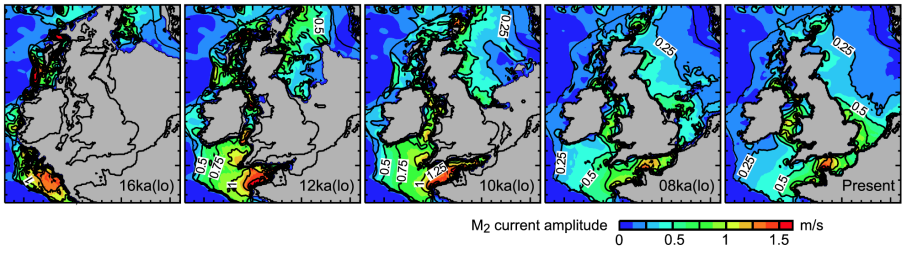

Figure 1.8: Modeled M_2 current amplitude in the northwest European shelf seas at 16, 12, 10, 8 ka BP (thousands years before present) and the present. Reprinted from Uehara et al. (2006).

Note that wave climate (wave height and wave period) also changes on the considered timescale (see e.g. van der Molen and de Swart, 2001b; Neill et al., 2009). It was demonstrated by Huthnance (1982b) and Roos et al. (2004) that bed erosion due to wave stirring prevents the crests of ridges from growing too close to the sea surface, as the near-bed wave orbital velocity is inversely proportional to the water depth.

1.5 RESEARCH QUESTIONS AND METHODOLOGY

As is described in Section 1.4, several aspects regarding the initial formation and long-term evolution of offshore tidal sand ridges remain unexplored, which are listed below. First, with regard to the initial formation of these bedforms, the sensitivity of their characteristics (growth rate, wavelength and crest orientation) to formulations of bed shear stress, sand transport and tidal forcing is not fully explored. Second, for these bedforms with a finite height, how their evolution is affected by assuming 1D or 2D configurations with unlimited sand, elliptical tidal current and critical bed shear stress for sand erosion has not been investigated. Third, the effect of changes in the sea level and tidal conditions on the long-term evolution of tidal sand ridges has not been considered.

The considerations above motivate the following specific research questions of this study.

1. How do the growth rate, wavelength and crest orientation of offshore tidal sand ridges depend on formulations for bed shear stress, sand transport (critical bed shear stress on/off, an-/isotropic slope-induced transport), and tidal forcing (ellipticity, diurnal/mixed/spring-neap tides)?
2. **(a)** What are the differences in the characteristics of finite-height tidal sand ridges, i.e., their shape and growth time, between cases using 1D and 2D configurations, assuming unlimited sand, rectilinear tides and no critical bed shear stress for sand erosion? If there are differences, why do they occur?
   (b) What is the effect of elliptical tides and critical bed shear stress for sand erosion on the characteristics of finite-height tidal sand ridges?
3. **(a)** How do SLR and variation in the strength and principal direction of the tidal current affect the characteristics (height and growth time) of active tidal sand ridges?
   (b) How and why do active ridges become quasi-active/moribund in the presence of SLR and tidal current variation?

To address these questions, an idealized nonlinear morphodynamic model was developed, based on the work of Caballeria et al. (2002) and Garnier et al. (2006). The model describes feedbacks between tidally forced depth-averaged currents and the sandy bed (through sand transport) in the offshore area of shelf seas. An open domain with no sloping bottom is used to mimic the open shelf.

There are several advantages to use a numerical model for the initial formation of tidal sand ridges. First, unlike linear stability models which employ the rigid-lid approximation, the time-dependent surface elevation is maintained in the present model. Second, linear stability models require explicit linearization of all equations and in particular for sand transport, which is often a laborious and delicate task. In the present model, this is not needed. Third, comparison of output of the numerical model with that of linear stability models is useful to validate the numerical model. If successful, the latter can be subsequently employed to investigate the long-term nonlinear evolution of these large-scale bedforms. This approach was also adopted to study the initial formation of other coastal bedforms, such as sand bars on planar beaches (Deigaard et al., 1999; Klein and Schuttelaars, 2005) and tidal sand waves (Borsje et al., 2013). Regarding the finite-height behavior of these ridge, there are two reasons to use an idealized model rather than other existing process-based models, e.g. Delft3D (Lesser et al., 2004) or MIKE21 (Warren and Bach, 1992). One reason is that the latter do not allow for periodic boundary conditions, whereas these bedforms are manifestations of rhythmic patterns. The other reason is that complex process based models require large computational effort for the long-term evolution of the bedforms.

1.6 OUTLINE OF THE THESIS

Based on the research questions listed in Section 1.5, the thesis is organized as follows. In Chapter 2, the focus is on research question 1. First, detailed description of the idealized nonlinear morphodynamic model is given. The way to apply the concept of linear stability analysis using the present model is also introduced. Several parameters are varied to examine whether they affect the initial formation of tidal sand ridges, i.e., linear versus nonlinear bottom friction, with or without critical bed shear stress for sand erosion, isotropic versus anisotropic slope-induced sand transport, tidal ellipticity and different tidal constituents.

Chapter 3 deals with research questions 2a and 2b. The model is similar as that of Chapter 2, but here the stirring of sand due to wind waves is also taken into account and a nonlinear rather than a linear stability analysis is conducted. First, the characteristics of finite-height tidal sand ridges with either 1D or 2D configurations are examined. Next, the sensitivity of the characteristics of the ridges to elliptical tides and critical bed shear stress for sand erosion is investigated. Furthermore, modeled ridges are compared with observed ridges in the southern North Sea.

In Chapter 4, research questions 3a and 3b are addressed. Changes in the sea level and characteristics of the tidal current are included in the model. Choosing the Dutch Banks in the southern North Sea as a prototype of active tidal sand ridges, the sensitivity of the height and growth time of the ridges to SLR and tidal current variation is investigated. Regarding the quasi-active/moribund ridges, the reason why

they occur is explored by studying the evolution of the ridges in the Celtic Sea subject to SLR and tidal current variation. Lastly, in Chapter 5, the results and conclusions from the previous chapters are summarized. Besides, an outlook for future research is given.

2

SENSITIVITY OF GROWTH CHARACTERISTICS OF TIDAL SAND RIDGES TO FORMULATIONS OF BED SHEAR STRESS, SAND TRANSPORT AND TIDAL FORCING

2.1 INTRODUCTION

It was mentioned in Chapter 1 that in studies on the initial formation of tidal sand ridges (Huthnance, 1982a; Hulscher et al., 1993; Carbajal and Montaño, 2001; Roos et al., 2001; Walgreen et al., 2002), several simplifications in the bed shear stress, tidal forcing and the sand transport were used. First, the bed shear stress was linearized. Second, the tidal forcing consisted of only one tidal constituent or only rectilinear tidal currents. Third, both the threshold of sand erosion and anisotropic bottom slope-induced sand transport were neglected for sand transport.

The aim in this chapter is to quantify the dependence of growth rate, wavelength and crest orientation of tidal sand ridges on formulations for (1) bed shear stress, (2) sand transport (critical shear stress on/off, an-/isotropic slope-induced transport), and (3) tidal forcing (ellipticity, diurnal/mixed tides, spring-neap tides). To fulfill this aim, based on Caballeria et al. (2002) and Garnier et al. (2006), an idealized nonlinear numerical morphodynamic model was developed, which governs feedbacks between tidally forced depth-averaged currents and the erodible sandy bed in an open domain that represents the offshore area of shelf seas. The main differences from the previous models concern the implementation of an open domain with no sloping bottom, periodic boundary conditions in both horizontal directions,

This chapter is based on:
Yuan, B., de Swart, H. E., Panadès, C., 2016. Sensitivity of growth characteristics of tidal sand ridges and long bed waves to formulations of bed shear stress, sand transport and tidal forcing: a numerical model study. *Continental Shelf Research* 127, 28–42.

tidal currents instead of wind- and wave-driven currents, and tidally-averaged sand transport.

This chapter is organized as follows. In Section 2.2, the morphodynamic model is introduced, after which the linear stability analysis is explained briefly, followed by a description of the numerical implementation and the setup of the simulations. Results are presented in Section 2.3 and subsequently discussed in Section 2.4. Finally, Section 2.5 contains the conclusions.

2.2 MATERIAL AND METHODS

2.2.1 *Model*

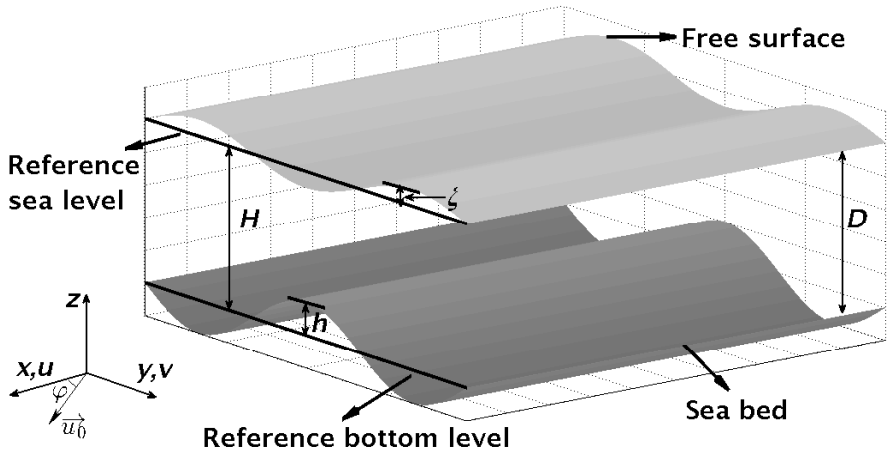

Figure 2.1: Sketch of the model geometry, also showing the spatially uniform tidal velocity vector $\vec{u}_0$ in its principal direction, and the angle φ between the principal direction of the tidal current and the x-axis. Other symbols are explained in the text.

The morphodynamic model consists of modules for the currents, sand transport and the bed evolution. Following Hulscher et al. (1993), the currents are assumed to be governed by the depth-averaged shallow water equations, which read

$$\frac{\partial D}{\partial t} + \nabla \cdot (D\vec{u}) = 0, \tag{2.1}$$

$$\frac{\partial \vec{u}}{\partial t} + (\vec{u} \cdot \nabla)\vec{u} + f\vec{e}_z \times \vec{u} = -g\nabla\zeta - \frac{\vec{\tau}_b}{\rho D}. \tag{2.2}$$

Here, D is the local water depth, given by $D = \zeta + H - h$, with ζ the surface elevation, H the undisturbed water depth and h the bed level with respect to the reference bottom level (Fig. 2.1). Vector $\vec{u}$ is the depth-averaged flow velocity, whose components in the x- and y-directions are u and v, respectively, and $\vec{e}_z$ is a unit vector in the vertical direction. Note that in the cross product $\vec{e}_z \times \vec{u}$, vector $\vec{u}$ is interpreted as a three-dimensional vector, with a zero vertical component, and that only the horizontal components of the cross product are considered. Furthermore, t is time, $\nabla = (\partial/\partial x, \partial/\partial y)$ is the horizontal nabla operator, $f = 2\Omega \sin\Phi$ is the Coriolis parameter, with Ω the angular frequency of the Earth and Φ the latitude. Finally, g is the gravitational acceleration, ρ is the constant water density, and $\vec{\tau}_b$ is the bed shear stress vector, for which specific formulations are given in Section 2.2.2.

Since tidal sand ridges are observed in the offshore area of shelf seas, an open domain with a flat bottom is used to mimic the offshore area. Eqs. 2.1 and 2.2 are considered in a finite domain $0 \leqslant x \leqslant L_x$, $0 \leqslant y \leqslant L_y$, which represents a small part of the offshore area. Typical values of L_x and L_y are 10–40 km, which are in the order of the wavelength of large-scale bedforms. The wavelength of the tidal waves L_t is approximately 400 km for a semidiurnal tide in water with a depth of the order of 10 m, hence it is assumed that L_x and L_y are much smaller than L_t. The assumption $L_x, L_y \ll L_t$ implies that, to a first approximation, the tidal wave is spatially uniform within the domain, which allows for imposing spatially uniform tidal forcing and periodic boundary conditions.

The tidal current is forced by a time-varying horizontal pressure gradient force per unit mass $\vec{F}_p$. The force is associated with the presence of a large-scale tidal wave, and $\vec{F}_p$ drives a spatially uniform tidal current $\vec{u}_0$ that obeys

$$\frac{\partial \vec{u}_0}{\partial t} + f\vec{e}_z \times \vec{u}_0 + \frac{\vec{\tau}_{b_0}}{\rho H} = \vec{F}_p, \qquad \vec{F}_p = -g\nabla\zeta_0. \tag{2.3}$$

Clearly, since the bed shear stress $\vec{\tau}_{b_0}$ is determined by $\vec{u}_0$, $\vec{F}_p$ defines $\vec{u}_0$, or vice versa. The assumptions underlying Eq. 2.3 are twofold. First, the magnitude of free surface variations ζ_0 is much smaller than the mean water depth H. Second, the large-scale tidal wave is unaffected by topographic variations that act on scales $L_x, L_y \ll L_t$.

Setting $\zeta = \zeta_0 + \tilde{\zeta}$ and $D = \tilde{D} + \zeta_0$, where $\tilde{\zeta}$ stands for the surface elevation induced by the varying topography, and recalling that $|\zeta_0| \ll H$, the continuity equation and the momentum equation are rewritten as (see Appendix 2.A for details)

$$\frac{\partial \tilde{D}}{\partial t} + \nabla \cdot (\tilde{D}\vec{u}) = 0, \tag{2.4}$$

$$\frac{\partial \vec{u}}{\partial t} + (\vec{u}\cdot\nabla)\vec{u} + f\vec{e}_z \times \vec{u} = -g\nabla\tilde{\zeta} + \vec{F}_p - \frac{\vec{\tau}_b}{\rho\tilde{D}}. \tag{2.5}$$

The components u_0 and v_0 of the spatially uniform tidal current $\vec{u}_0$ that results from the pressure gradient force $\vec{F}_p$ in the absence of bottom undulations are expressed as harmonic series:

$$u_0 = U_0 + \sum_i \left[a_i \cos(\omega_i t - \phi_i) \cos\varphi_i - b_i \sin(\omega_i t - \phi_i) \sin\varphi_i \right], \tag{2.6a}$$

$$v_0 = V_0 + \sum_i \left[a_i \cos(\omega_i t - \phi_i) \sin\varphi_i + b_i \sin(\omega_i t - \phi_i) \cos\varphi_i \right]. \tag{2.6b}$$

In these expressions, U_0 and V_0 are the horizontal components of the residual flow M_0 (not considered in this chapter), the subscript i represents different tidal constituents, with ω_i and ϕ_i being the angular frequency and phase of a tidal constituent. Furthermore, a_i and b_i are the sizes of semi-major and semi-minor axes of the tidal ellipse, and φ_i is the angle between the major axis of the tidal ellipse and the x-axis (Fig. 2.1). As in Hulscher et al. (1993) and Blondeaux et al. (2009), the ellipticity of the tidal constituent is defined as $\epsilon_i = b_i/a_i$. Positive (negative) ϵ_i means that the end point of the velocity vector of that constituent follows an ellipse in a counterclockwise (clockwise) sense.

The bed level evolution is governed by the mass conservation of sediment,

$$(1-p)\frac{\partial h}{\partial t} + \nabla \cdot \vec{q} = 0. \tag{2.7}$$

Here, $\vec{q}$ is the volumetric sand transport per unit width (formulations are given in Section 2.2.2), and p is the bed porosity (typically ~ 0.4). The evolution of tidally induced bedforms is, to a good approximation, related to convergence of net sand transport that results from averaging over a tidal cycle. This is because the evolution time scales of those bedforms are much larger than the tidal period. The justification for the approximation follows from scaling arguments and the averaging theory that is discussed in Sanders et al. (2007). Hence, the bed level is assumed to be fixed when computing the hydrodynamics over a tidal cycle, and Eq. 2.7 is averaged over the tidal period, which results in

$$(1-p)\frac{\partial h}{\partial t} + \nabla \cdot \langle \vec{q} \rangle = 0. \tag{2.8}$$

Here, $\langle \cdot \rangle = T^{-1} \int_0^T \cdot \, dt$ stands for tidal average, where T is the tidal period. For currents with more than one tidal constituent, the tidal period is calculated as the least common multiple of the periods of the tidal constituents. In summary, the final system to be solved consists of Eqs. 2.4, 2.5 and 2.8, with $\vec{F}_p$ chosen such that in the absence of bottom undulations the tidal current is described by Eq. 2.6.

2.2.2 *Formulations of bed shear stress and sand transport*

To check the sensitivity of the initial formation of tidal sand ridges to using a linearized/nonlinear bed shear stress, two formulations for the bed shear stress $\vec{\tau}_b$ are employed, i.e. a quadratic formulation

$$\vec{\tau}_b = \rho C_d \vec{u}|\vec{u}|, \tag{2.9}$$

and a linear formulation

$$\vec{\tau}_b = \rho r \vec{u}. \tag{2.10}$$

In these expressions, C_d ($\sim 10^{-3}$) is the drag coefficient, and r is the linear friction coefficient given by $r = 8/(3\pi)C_d U_{max}$. The latter expression is derived from Lorentz linearization of the bed shear stress (Zimmerman, 1982). Here U_{max} is the maximum velocity of the basic flow $\vec{u}_0$. Linear and nonlinear bed shear stress were also considered by Roos et al. (2008), but they did not systematically investigate the differences in the resulting growth characteristics of the bedforms.

Regarding sand transport, a bed load formulation is used. Suspended load is not considered, as Besio et al. (2006) found that for coarse sand and a moderate tidal current, the contribution of suspended load to the growth of the bedforms is negligible. The formulation for sand transport used is that of Fredsøe and Deigaard (1992), which is also used in Blondeaux et al. (2009):

$$\vec{q} = \frac{30Q_C}{\mu_d \pi}(\theta-\theta_c)(\sqrt{\theta}-0.7\sqrt{\theta_c})\left(\frac{\vec{u}}{|\vec{u}|}-\nabla h\cdot\mathbf{G}\right)\mathscr{H}(\theta-\theta_c). \tag{2.11}$$

Here, $Q_C = \sqrt{(s-1)gd^3}$ is the characteristic sand transport rate, where s is the ratio of densities of non-cohesive sand and water (s=2.6 is used), and d is the uniform grain size. The coefficient μ_d (0.32–0.75) is the dynamic friction coefficient of the bed material. The Shields parameter θ is given by

$$\theta = \frac{|\vec{u}|^2}{(s-1)gdC'^2}, \tag{2.12}$$

and θ_c is the critical Shields parameter. The typical value of θ_c ranges between 0.03 and 0.06. For a given θ_c, the critical depth-averaged velocity U_c for sand erosion can be obtained from Eq. 2.12. Using the Heaviside function $\mathscr{H}$ guarantees that sand transport only takes place when $\theta > \theta_c$. Furthermore, C' is the grain-related conductance coefficient given by $C' = 2.5\ln(11H/2.5d)$. The dimensionless tensor $\mathbf{G}$ (Seminara, 1998) is related to the slope-induced sand transport. For isotropic sand transport, the tensor $\mathbf{G} = \Lambda\mathbf{I}$, where Λ is called the bed slope coefficient and $\mathbf{I}$ is the unit tensor. For anisotropic sand transport, in a reference frame $(\mathbf{s},\mathbf{n})$ in which $\mathbf{s}$ is

aligned with the bed shear stress and **n** is normal to that direction, the elements of **G** read

$$G_{ns} = G_{sn} = 0, \qquad G_{ss} = \frac{\theta_c}{\mu_d}\frac{1}{|\vec{q}_0|}\frac{d|\vec{q}_0|}{d\theta}, \qquad G_{nn} = \frac{k_G}{\sqrt{\theta}}. \tag{2.13}$$

Here, $|\vec{q}_0|$ is the modulus of the sand transport rate $\vec{q}$ over a flat bed ($h = 0$ in Eq. 2.11), and k_G is an empirical coefficient that has values in the range of 0.5–0.6. By using the expression of θ (Eq. 2.12), $\vec{q}$ is written as

$$\vec{q} = \alpha_e(|\vec{u}|^2 - U_c^2)(|\vec{u}| - 0.7U_c)\left(\frac{\vec{u}}{|\vec{u}|} - \nabla h \cdot \mathbf{G}\right)\mathscr{H}(|\vec{u}| - U_c), \tag{2.14}$$

where

$$\alpha_e = \frac{30Q_C}{\mu_d \pi}\left(\frac{1}{(s-1)gdC'^2}\right)^{\frac{3}{2}}, \qquad U_c = [\theta_c\,(s-1)\,g\,d]^{\frac{1}{2}}C'. \tag{2.15}$$

If the critical velocity $U_c = 0$ and isotropic sand transport is considered, Eq. 2.14 reduces to the formulation as that in Hulscher et al. (1993):

$$\vec{q} = \alpha_e|\vec{u}|^3\left(\frac{\vec{u}}{|\vec{u}|} - \Lambda\nabla h\right). \tag{2.16}$$

2.2.3 *Linear stability analysis*

In this chapter, the initial formation of bedforms is investigated by applying the concepts of linear stability analysis. First, a basic state is defined, which is the spatially uniform tidal current $\vec{u}_0$ over a flat bottom. After that, small perturbations of the bottom h_0 are introduced, which are periodic in the domain with length and width L_x and L_y:

$$h_0 = h(x, y, 0) = Ae^{\mathrm{i}(k_x x + k_y y)} + c.c.. \tag{2.17}$$

In this expression, A is an amplitude that is much smaller than H, k_x and k_y are topographic wavenumbers in the x- and y-directions, and $c.c.$ denotes a complex conjugate (the same applies elsewhere). Each h_0 with a pair of (k_x, k_y) is called a bottom mode. There are two ways to specify the directions of the basic flow and the topographic wave vector of the perturbations. One is to fix the principal direction of the basic flow and vary k_x and k_y. The other is to give a basic flow with varying principal directions and fix the orientation of the crest lines, for instance, by setting the topographic wave vector as $(0, k_y)$ (the crests of the perturbation are along the x-axis). Next, the interaction between the flow and the bottom topography is investigated. According to linear stability theory, since A is small, the solution of the flow and the bed level is written as

$$(u, v, h) = (u_0, v_0, 0) + [(u_1, v_1, h_1)Ae^{\mathrm{i}(k_x x + k_y y)} + c.c.] + O(A^2). \tag{2.18}$$

Here, $(u_0, v_0, 0)$ is the basic state, and (u_1, v_1, h_1) is the solution at the first order of A. Higher order terms in the solution are neglected. By plugging the solution above in the original governing equations, the linearized equations for (u_1, v_1, h_1) are derived. For a given basic flow, it turns out that each bottom mode evolves as

$$h(x, y, t) = Ae^{\Gamma t} e^{\mathrm{i}(k_x x + k_y y)} + c.c., \tag{2.19}$$

with Γ the complex growth rate of the mode, which depends on the topographic wave vector. The real part of Γ is Γ_r, its reciprocal Γ_r^{-1} being the e-folding growth time τ_e of the amplitude of the mode. The mode with the largest Γ_r is called the "fastest growing mode" or the "preferred mode/bedform". The imaginary part Γ_i is the radian frequency of the mode, which is related to the migration speed $(-\Gamma_i/k_x, -\Gamma_i/k_y)$. As will be shown in Section 2.2.5, the bedforms considered in this chapter have no migration speed.

2.2.4 *Numerical implementation*

The system (Eqs. 2.4, 2.5 and 2.8), with specific formulations for bed shear stress and sand transport, is solved by using a finite-difference numerical scheme on a regular rectangular staggered grid (Caballeria et al., 2002; Garnier et al., 2006). A central second-order discretization is used in space, while an explicit fourth-order Runge-Kutta scheme is applied for time integration. The explicit scheme needs to satisfy the Courant-Friedrichs-Levy condition, i.e., $\Delta t \leq C \min\{\Delta x, \Delta y\}/\sqrt{gD_{max}}$, where Δt is the time step and $(\Delta x, \Delta y)$ the grid sizes, and D_{max} the maximum water depth. The constant C is determined empirically (generally $C \leq 1.0$). The way of coupling tidal current and sand transport is shown in Fig. 2.2.

The domain size (L_x, L_y) varies in the range of 1–36 km. Initially, bed perturbations as those in Eq. 2.17 with a small amplitude A (0.1% of the undisturbed water depth) are imposed on a flat bottom. Details of the basic state and domain size are given in Section 2.2.5 for different experiments.

Sand transport is calculated after the basic flow has been spun up to a dynamic equilibrium state (the relative tolerance of velocity magnitude at successive tidal cycles is within 0.001%). To calculate the growth rate, the root-mean-square height of the perturbation h_{rms} is computed at the beginning of each tidal cycle, which is defined as

$$h_{rms}(t) = \overline{(h(x, y, t)^2)}^{\frac{1}{2}}. \tag{2.20}$$

Here, the overbar denotes spatial averaging. From Eqs. 2.17 and 2.19, it follows that h_{rms} satisfies

$$h_{rms}(t) = h_{rms}(0)e^{\Gamma_r t}. \tag{2.21}$$

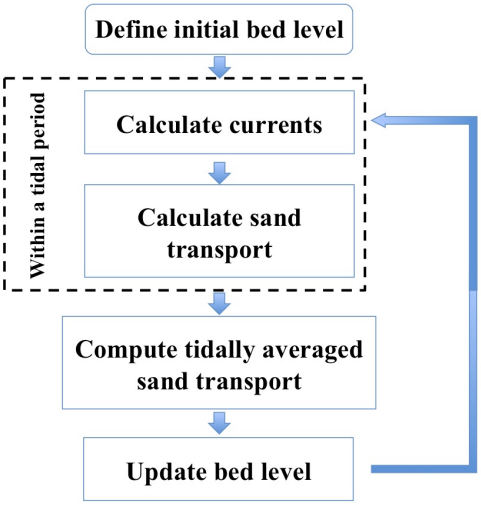

Figure 2.2: Flow chart of the numerical model.

Hence the real part of the growth rate is computed as

$$\Gamma_r = \frac{1}{NT} \ln\left(\frac{h_{rms}(NT)}{h_{rms}(0)}\right). \tag{2.22}$$

Here, N is an integer that is larger than the number of tidal periods needed for the spin up. At time NT, the term $\ln(h_{rms}(NT)/h_{rms}(0))$ is calculated, and finally the average of Γ_r over several N is taken. Eq. 2.22 is basically the same as the formulation for calculating Γ_r in Borsje et al. (2013).

2.2.5 *Design of the experiments*

Details about the design of the numerical experiments are given in Table 2.1. Values of the other parameters for the experiments are shown in Table 2.2. Note that the imposed tidal forcing only includes M_2, K_1, the joint action of $M_2 + K_1$ and $M_2 + S_2$. Migration of the bedforms occurs only if the tidal forcing consists of multiple constituents with angular frequencies that have an integer ratio, for instance, M_2+ residual, $M_2 + M_4$ (Roos et al., 2001; Walgreen et al., 2002). The tidal frequencies of the tidal constituents in this chapter have non-integer ratios. Hence the bedforms driven by these tidal constituents do not migrate, and the focus here is on the real part of the growth rate Γ_r.

Table 2.1: Overview of the set up of the experiments

Exp.	lin/nonlin	Sand transport		Tidal currents		
		U_c (m s^{-1})	iso/aniso	Constituents	U_{max} (m s^{-1})	ϵ
1	lin	0	iso	M_2	1.0	0
2	nonlin	0	iso	M_2	1.0	0
3	lin	0.18:0.2:0.98	iso	M_2	1.0	0
4	lin	0	aniso	M_2	1.0	0
5	lin	0	iso	M_2	1.0	-1:0.2:1
6	lin	0	iso	K_1'	1.0	0
7	lin	0	iso	$M_2'+K_1'$		0
8	lin	0	iso	$M_2'+S_2$		0
9	nonlin	0.58	aniso	M_2	0.6	0.4

In this table, 'lin/nonlin' means linear/nonlinear friction, 'iso/aniso' means isotropic/anisotropic slope-induced sand transport, U_{max} is the maximum velocity of the basic flow $\vec{u}_0$, and ϵ is the tidal ellipticity. The notations with ':' mean from the first number to the third number with an increment of the middle number. The periods for K_1' and M_2' are chosen as 24 hours and 12.5 hours, respectively.

Table 2.2: Default values of parameters used in the experiments

	Parameter	Value	Description
	Ω	7.292×10^{-5} rad s^{-1}	Angular frequency of the Earth
	Φ	52°N	Latitude
	ω_{M_2}	1.40×10^{-4} rad s^{-1}	Angular frequency of M_2 (M_2') tide
	ω_{S_2}	1.45×10^{-4} rad s^{-1}	Angular frequency of S_2 tide
	$\omega_{K_1'}$	7.27×10^{-5} rad s^{-1}	Angular frequency of K_1' tide
	g	9.81 m s^{-2}	Gravitational acceleration
	p	0.4	Bed porosity
	Λ	2.37	Bed slope coefficient
	μ_d	0.6	Dynamic friction coefficient
	k_G	0.55	Empirical coefficient for anisotropic sand transport
Exp. 1–8	H	30 m	Undisturbed water depth
	α_e	2.4×10^{-5} m^{-1} s^2	Coefficient for sand transport
	r	0.0025 m s^{-1}	Linear friction coefficient
Exp. 9	H	40 m	Undisturbed water depth
	d	0.4 mm	Grain size
	θ_c	0.051	Critical Shields parameter

In Exp. 2, the drag coefficient C_d (0.003) is calculated from $r = 8/(3\pi)C_d U_{max}$ using $U_{max} = 1$ m s^{-1}. In Exp. 9, C_d is calculated by $C_d = (2.5\ln(11\bar{D}/z_r))^{-2}$ as in Blondeaux et al. (2009), where z_r is the roughness of the seabed and a value of 2.5 cm is used.

First, to check if the model is capable of reproducing the initial formation of tidal sand ridges, the same parameter values and formulations for sand transport and bottom friction as those in Hulscher et al. (1993) (Exp.1) are used. Next, the effect of nonlinear bed shear stress on the characteristics (growth rate, wavelength and orientation) of the preferred bedforms during their initial formation is studied in Exp. 2. Furthermore, using Eq. 2.14, a critical depth-averaged velocity U_c for sand erosion and anisotropic slope-induced sand transport are considered in Exps. 3 and 4, respectively. Decreasing U_c means either decreasing grain size or assuming an increase in stirring of sand by waves. In this chapter, the latter interpretation applies since the grain size is assumed to be kept as a constant. In the experiments hereafter, tidal currents with different characteristics are considered: elliptical tidal currents in Exp. 5, the diurnal tide in Exp. 6, the mixed semidiurnal tide in Exp. 7, and the spring-neap tide in Exp. 8. To reduce the computation time, in Exp. 7 the periods of the M_2 tide and the K_1 tide are adjusted slightly (denoted by M_2' and K_1', respectively). The same applies to Exp. 8, in which the adjusted M_2' tide is used. In the cases of a mixed tide and a spring-neap tide, the tidal constituents are chosen to have the same phase and inclination. For the mixed tide, the velocity amplitude of the M_2' tide $U_{M_2'} = 1$ m s^{-1}, while the velocity amplitude of the K_1' tide $U_{K_1'}$ increases from 0.1 m s^{-1} to 0.5 m s^{-1}. For the spring-neap tide, the velocity amplitudes of the tidal constituents are chosen such that the representative amplitude $U_r = ({U_{M_2'}}^2 + {U_{S_2}}^2)^{1/2}$ is kept at 1 m s^{-1}. Furthermore, in Exp. 9, both the critical depth-averaged velocity U_c for sand erosion and elliptical tidal currents are considered. The same parameter values (Tables 2.1 and 2.2) and formulations as in Blondeaux et al. (2009) are used. In that study, they found that another type of large-scale bedforms, long bed waves, form if the amplitude of the tidal current is slightly above the critical velocity for sand erosion and the current is elliptical.

In Exp. 1, two ways of specifying the directions of the basic flow and bottom perturbations are used. In the first configuration, the principal direction of the basic tidal current is parallel to the x-direction, and the wavenumbers of the perturbation are chosen as $k_x = 2\pi/L_x$ and $k_y = 2\pi/L_y$, where L_x and L_y are the length of the domain in the x- and y-directions, respectively. The sampled wavenumbers are shown in Fig. 2.3a. This is done in order to allow for straightforward comparison of model results with those of Hulscher et al. (1993). In the second one, it is configured such that the wavelength and orientation of the fastest growing mode can be accurately identified: the direction of the basic flow φ is varied between $-90°$ and $90°$, and the bottom modes have wavenumbers $(0, k_y)$ ($k_y = k = 2\pi/L_y$). This means that the crests of the bottom modes are parallel to the x-axis, and the angle ϑ between the principal current direction and the crests equals to φ. Positive/negative ϑ means that the crests are rotated anticyclonically/cyclonically with respect to the principal current direction in the Northern Hemisphere. Hereafter, whenever the orientation

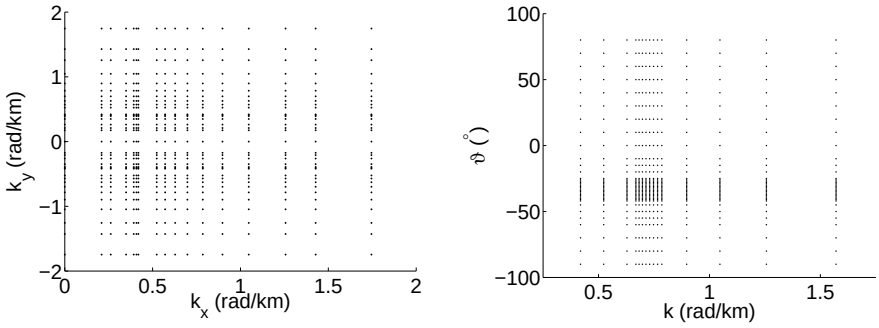

(a) (b)

Figure 2.3: Sampled parameter space (wavenumbers k_x, k_y of the bottom perturbation and angle ϑ between the principal current direction and the crests): the first configuration (a) and the second one (b). Each dot corresponds to a sampled mode.

of the mode/crests is mentioned, it is always with respect to the principal current direction. First a relatively low resolution in the (ϑ, k) space is used, possible later refinement is done after analysis of these results. The second configuration is used in all other experiments. The sampled parameter space of Exp. 1 using the second configuration is shown in Fig. 2.3b. Generally, near the fastest growing mode, the resolution in ϑ is within 1° (up to 0.2°), and in the wavelength it is around 200 m for Exp. 1-8 (the grid sizes are $\Delta x = \Delta y = 200$ m, with a time step $\Delta t = 10$ s) and 100 m for the Exp. 9 (the grid sizes are $\Delta x = \Delta y = 100$ m, with a time step $\Delta t = 5$ s). Tests have shown that if the bottom modes have wavenumbers $(0, k_y)$, the domain length in the x-direction L_x does not affect the growth rate of the modes. Hence L_x is chosen equal to $3\Delta x$, which is the minimum possible value.

2.3 RESULTS

2.3.1 *Verification with Hulscher et al. (1993)*

First the present model is run using the same configuration and parameter values as those used in Hulscher et al. (1993) (Exp. 1 in Table 2.1). Fig. 2.4a shows a contour plot of the dimensionless growth rate $\hat{\Gamma_r}$ of the bed perturbations versus dimensionless wavenumbers $\hat{k_x}$ ($\hat{k_x} = k_x U_{max}/\omega$) and $\hat{k_y}$ ($\hat{k_y} = k_y U_{max}/\omega$) . In this configuration, the principal direction of the basic flow is along the x-axis, as in Hulscher et al. (1993). Here, $\hat{\Gamma_r} = T_m \Gamma_r$, where $T_m = (1-p)H/(\alpha_e U_{max}^2 \omega)$ is the morphological time scale. For $H = 30$ m, $U_{max} = 1$ m s^{-1}, $\omega = 1.4 \times 10^{-4}$ rad s^{-1}, $p = 0.4$ and $\alpha_e = 2.4 \times 10^{-5}$ m^{-1} s^2, $T_m \approx 170$ yr. In Fig. 2.4b, the results are shown in a diffe-

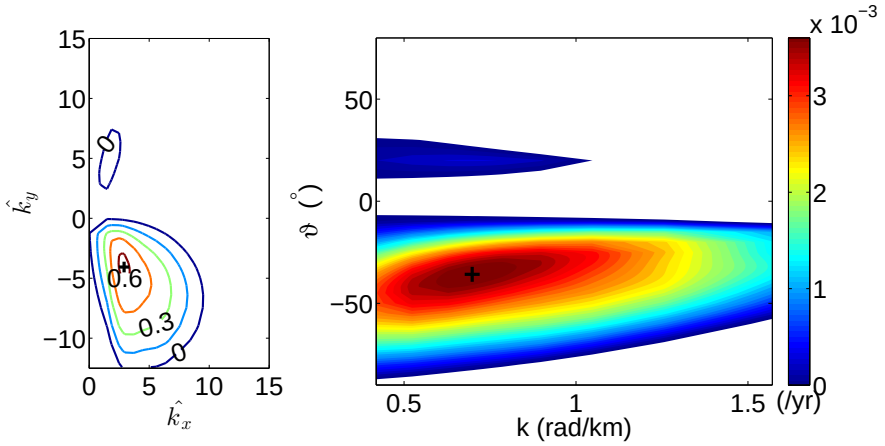

(a) (b)

Figure 2.4: Exp. 1: (a) Dimensionless growth rate of the bed perturbations as a function of the dimensionless wavenumbers; (b) dimensional growth rate Γ_r as a function of dimensional wavenumber k and angle ϑ between the principal current direction and the crests of the bed perturbations. The plus corresponds to the fastest growing mode.

rent way, i.e., dimensional growth rate Γ_r as a function of dimensional wavenumber k and angle ϑ between the principal current direction and the crests (parallel to the x-direction) of the bed perturbation. Growing modes (modes with positive growth rate Γ_r) with different orientations are observed, i.e., their crests are either cyclonically or anticyclonically rotated with respect to the principal direction of the tidal current. From Fig. 2.4, it is seen that the fastest growing mode has a dimensionless wavenumber of 5.0 and a dimensional wavenumber of ~ 0.7 rad km^{-1}, which is equivalent to a dimensional wavelength of 9.0 km. Furthermore, the direction of the crests is approximately 35.8° cyclonically oriented with respect to the principal current direction. The obtained wavelength and the angle between the principal current direction and the crests of the fastest growing mode are larger than those in Hulscher et al. (1993) (wavelength approximately 8 km and $|\vartheta|$ approximately 30°). The e-folding time scale τ_e ($\tau_e = \Gamma_r^{-1}$) is 270 yr, while it is around 400 yr in Hulscher et al. (1993). Possible reasons for these differences will be discussed in Section 2.4.

2.3.2 *Nonlinear bed shear stress*

For the case using a nonlinear bed shear stress (Exp. 2), the growth rate of the bed perturbations as a function of dimensional wavenumber k and angle ϑ between the principal current direction and the crests of the bed perturbation is shown in Fig. 2.5.

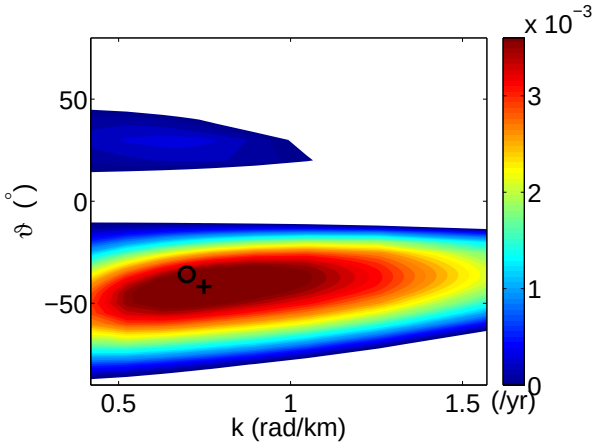

Figure 2.5: Growth rate Γ_r of the bed perturbations as a function of wavenumber k and angle ϑ between the principal current direction and the crests of the bed perturbations, using nonlinear bed shear stress (Exp. 2). The plus and circle correspond to the fastest growing modes using nonlinear shear stress (Exp. 2) and linearized stress (Exp. 1), respectively.

The fastest growing mode has a smaller e-folding time ($\tau_e \approx 250$ yr) and a slightly smaller wavelength (~ 8.4 km) than that obtained if a linearized bed shear stress is used, while the angle ($\sim 41.8°$) between the principal current direction and the crests becomes larger.

2.3.3 *Critical bed shear stress for sand erosion*

Fig. 2.6 shows the e-folding time, wavelength and orientation of the fastest growing mode versus the critical averaged velocity for sand erosion U_c (Exp. 3). In general, the e-folding time of the fastest growing mode increases as the critical velocity increases. Moreover, the wavelength and the angle between the principal current direction and the crests decrease with increasing U_c. For $U_c = 0.58$ m s^{-1}, the e-folding time of the fastest growing mode ($\tau_e \approx 390$ yr) increases more than 31% of that if the threshold is not considered (Fig. 2.6a), and the wavelength decreases by around 1.4 km (Fig. 2.6b). The change in the orientation angle is less significant until U_c reaches 0.78 m s^{-1} (Fig. 2.6c).

Note that once the critical velocity is close to the maximum current velocity, it is seen from the growth rate Γ_r of the bed perturbations shown in Fig. 2.7 that, Γ_r decreases significantly and the maxima are found not only near the wavelength of 5.4 km with $\vartheta \sim -28°$, but also around 2.4 km with $\vartheta \sim -34°$. The latter parameters are representative for long bed waves, since the wavelength is between those of sand

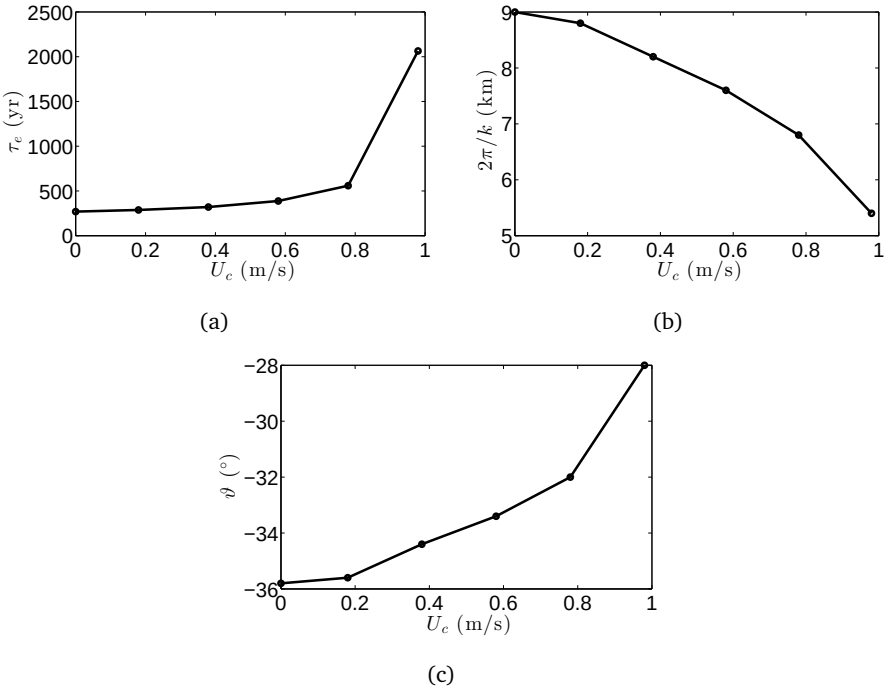

Figure 2.6: (a) The e-folding time τ_e , (b) wavelength $2\pi/k$ and (c) orientation angle ϑ of the fastest growing mode as a function of the critical depth-averaged velocity U_c for sand erosion (Exp. 3).

waves and tidal sand ridges, albeit that the orientation angle found here differs from the observations (approximately −60° or 30°).

2.3.4 *Anisotropic slope-induced sand transport*

The growth rate of the bed perturbations in Exp. 4 using anisotropic slope-induced sand transport is shown in Fig. 2.8. Compared to the case using isotropic slope-induced sand transport (Exp. 1), the fastest growing mode has a slightly smaller e-folding time ($\tau_e \approx 250$ yr) and a smaller wavelength (~ 8.2 km). The orientation of the fastest growing mode hardly changes.

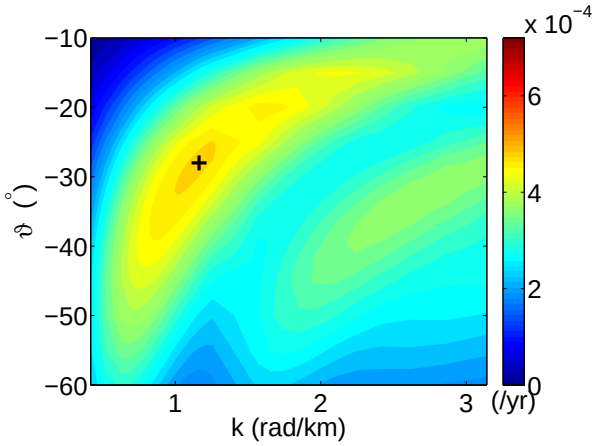

Figure 2.7: Growth rate Γ_r of the bed perturbations as a function of wavenumber k and angle ϑ between the principal current direction and the crests of the bed perturbations, with the critical depth-averaged velocity U_c for sand erosion equal to 0.98 m s^{-1} (Exp. 3). The plus corresponds to the fastest growing mode.

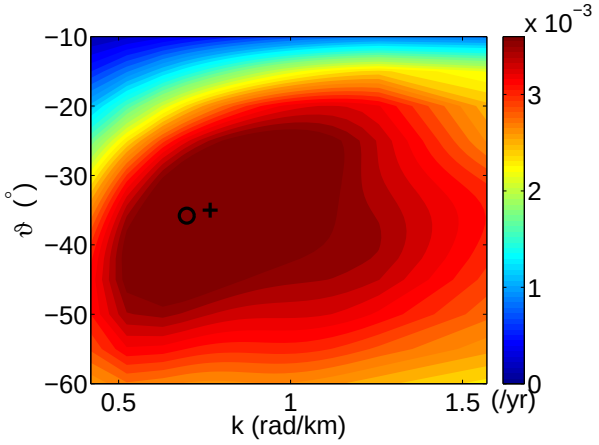

Figure 2.8: Growth rate Γ_r of the bed perturbations as a function of wavenumber k and angle ϑ between the principal current direction and the crests of the bed perturbations, using anisotropic slope-induced sand transport (Exp. 4). The plus and circle correspond to the fastest growing modes using anisotropic (Exp. 4) and isotropic sand transport (Exp. 1), respectively.

2.3.5 *Tidal ellipticity*

The e-folding time, wavelength and orientation of the fastest growing mode against tidal ellipticity ϵ (Exp. 5) are shown in Fig. 2.9. The e-folding time of the fastest gro-

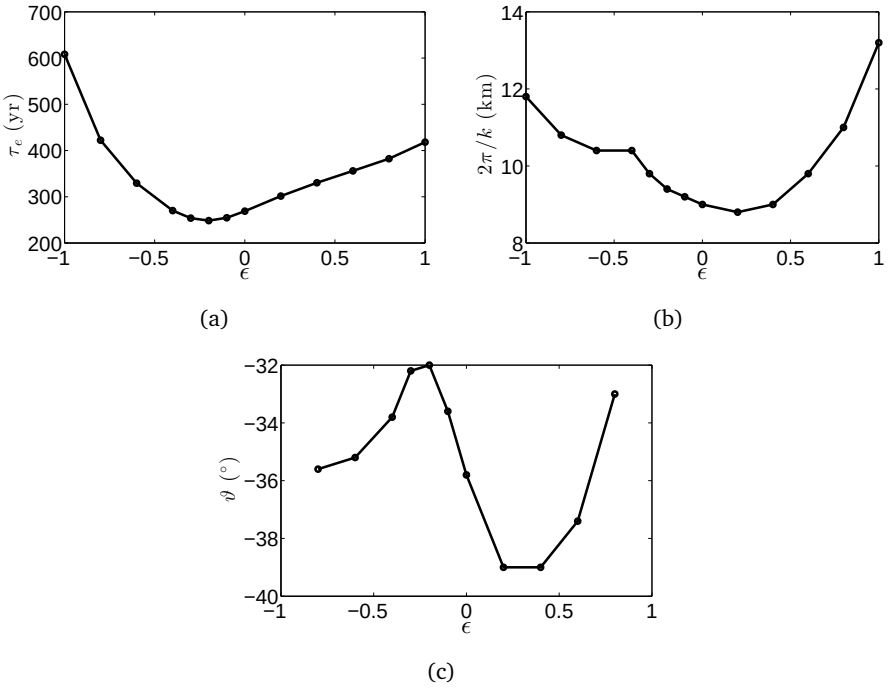

Figure 2.9: (a) The e-folding time τ_e , (b) wavelength $2\pi/k$ and (c) orientation angle ϑ of the fastest growing mode as a function of tidal ellipticity ϵ (Exp. 5).

wing mode using circular tides is approximately 1.3 ($\epsilon = 1$) and 2 ($\epsilon = -1$) times of that using a rectilinear tidal current. Note that the smallest e-folding time of the fastest growing modes along ϵ is not found at $\epsilon = 0$, but rather near $\epsilon = -0.2$. The wavelength of the fastest growing mode does not change much for $-0.3 \leq \epsilon \leq 0.4$, and the smallest wavelength is observed near $\epsilon = 0.2$. It increases as the absolute value of ϵ increases for $|\epsilon| > 0.4$. The orientation angle of the fastest growing mode also depends non-monotonically on the tidal ellipticity. The absolute value of ϑ decreases from $\epsilon = -0.8$ to $\epsilon = -0.2$, next increases rapidly until $\epsilon = 0.2$ and decreases again towards $\epsilon = 0.8$. Note that for $\epsilon = \pm 1$, the growth rates of the perturbation are independent of the angle ϑ, thus in Fig. 2.9c no data are shown for $\epsilon = \pm 1$.

2.3.6 *Diurnal tide*

Fig. 2.10 shows a contour plot of the growth rate of the bed perturbations using a diurnal tide K_1' (Exp. 6). Compared to the result in Exp. 1, it is found that the e-folding

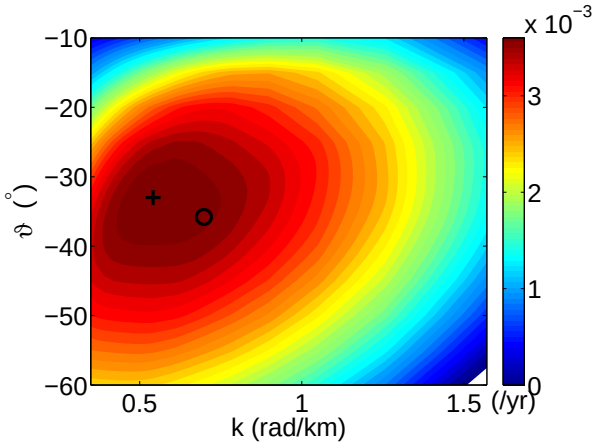

Figure 2.10: Growth rate Γ_r of the bed perturbations as a function of wavenumber k and angle ϑ between the principal current direction and the crests of the bed perturbations, using the K_1' tide (Exp. 6). The plus and circle correspond to the fastest growing modes using K_1' (Exp. 6) and M_2 (Exp. 1), respectively.

time of the fastest growing mode using a diurnal tide hardly changes. Furthermore, it is seen that the fastest growing mode using the K_1' tide has a smaller wavenumber (equivalently the wavelength increases by around 3 km) and a smaller orientation angle (around 3° smaller) than that using the M_2 tide.

2.3.7 *Mixed tide and spring-neap tide*

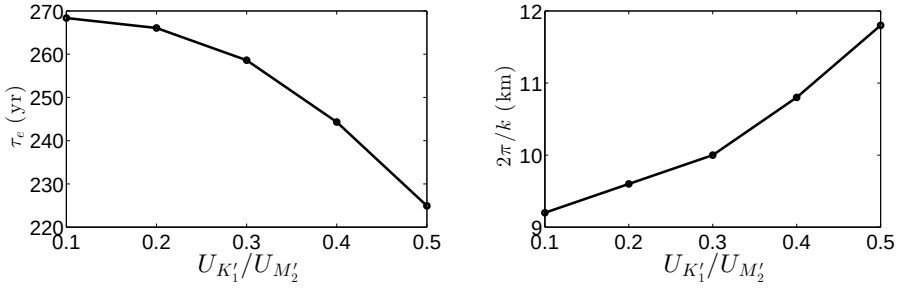

(a) (b)

Figure 2.11: (a) The e-folding time τ_e and (b) wavelength $2\pi/k$ of the fastest growing mode as a function of $U_{K_1'}/U_{M_2'}$ (Exp. 7).

Fig. 2.11 shows the e-folding time and wavelength of the fastest growing modes against the ratio of the velocity amplitude of the K_1' tide and the M_2' tide (Exp. 7). If $U_{M_2'}$ is fixed, it is found that as the ratio $U_{K_1'}/U_{M_2'}$ increases from 0.1 to 0.5, the e-folding time of the fastest growing modes decreases (Fig. 2.11a) by approximately 40 yr, while the wavelength of the fastest growing modes increases (Fig. 2.11b) by 2.6 km. The orientation angles of the fastest growing modes are between −36° and −35° (not shown). The results of additional experiments show that phase difference between tide K_1' and tide M_2' has no effect on the growth rate, wavelength and orientation of the fastest growing modes.

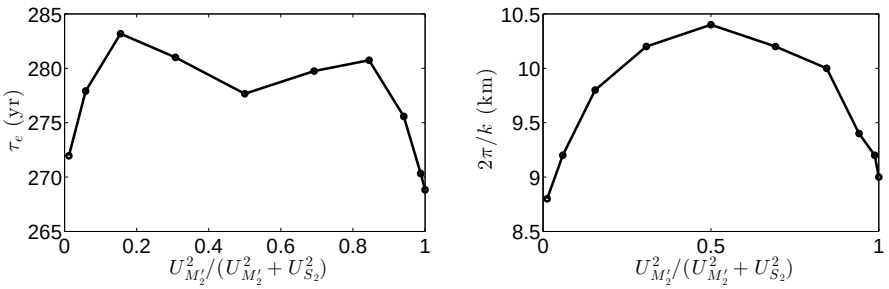

(a) (b)

Figure 2.12: (a) The e-folding time τ_e and (b) wavelength $2\pi/k$ of the fastest growing mode as a function of $U^2_{M_2'}/(U^2_{M_2'}+U^2_{S_2})$ (Exp. 8).

In Fig. 2.12, the e-folding time and wavelength of the fastest growing modes are plotted against the ratio between the squared velocity amplitude of the M_2' tide and the squared representative velocity (Exp. 8). It appears that the dependency of the e-folding time of the fastest growing modes (Fig. 2.12a) on this parameter is rather weak (changes are less than 15 yr). In contrast, the wavelength of the fastest growing modes (Fig. 2.12b) increases by around 1.4 km when the ratio $U^2_{M_2'}/(U^2_{M_2'}+U^2_{S_2})$ increases from 0 to 0.5, i.e., from the S_2 tide dominant to $U_{M_2'}=U_{S_2}$. The change of the orientation angles is within 1° (not shown). Like in the case of the mixed tides, the phase difference between the M_2' tide and the S_2 tide does not affect the characteristics of the fastest growing modes. The variations in the growth rate and the wavelength of the preferred bedforms for the mixed tides and spring-neap tides reveal that the characteristics of these bedforms are determined by the dominant tidal constituent.

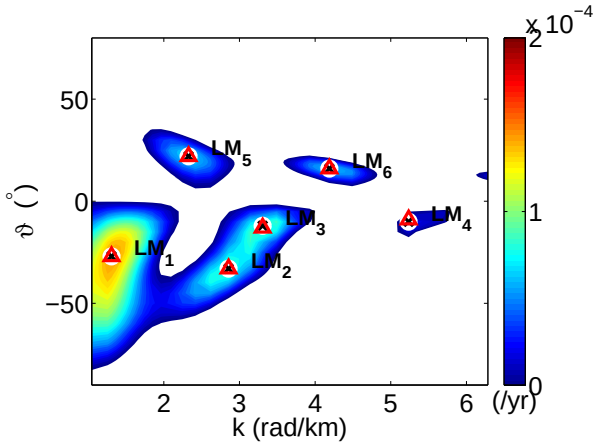

Figure 2.13: Growth rate Γ_r of the bed perturbations as a function of wavenumber k and angle ϑ between the principal current direction and the crests of the bed perturbations, with both critical bed shear stress and elliptical tides (Exp. 9). Local maxima are marked by the crosses in the white circles, and are named as LM_1 to LM_6. The triangles indicate the local maxima found by Blondeaux et al. (2009).

2.3.8 *Combined tidal ellipticity and critical velocity for sand erosion*

The combination of tidal ellipticity and critical shear stress is considered in Exp. 9. The drag coefficient was calculated using the same formulation as that of Blondeaux et al. (2009), i.e., $C_d = (2.5 \ln(11\tilde{D}/z_r))^{-2}$, where $z_r = 2.5$ cm is the roughness of the sea bottom. In that case, the morphological time scale, for the given sand transport formulation and parameters, is $T_m \sim 500$ years. The result is shown in Fig. 2.13, in which several local maxima in the growth rate Γ_r (LM_1 to LM_6) with both positive and negative orientation angles are observed. The maximum in Γ_r with the smallest wavenumber LM_1 is identified at $k \sim 1.30$ rad/km and $\vartheta \sim -27°$, the corresponding e-folding time is around 13 times of the morphological time T_m. This is related to the tidal sand ridge mode that has a wavelength of around 4.8 km and crests that are $\sim 27°$ cyclonically oriented with respect to the principal current direction. The other local maxima in Γ_r occur for wavenumbers that correspond to those of long bed waves modes (wavelengths are in the range of 1–3 km). Two local maxima in Γ_r with negative ϑ, LM_2 and LM_3, are observed at a wavelength of around 2 km. One is found at $k \sim 2.9$ rad/km (wavelength around 2.2 km) and $\vartheta \sim -33°$, and the other at $k \sim 3.3$ rad/km (wavelength around 1.9 km) and $\vartheta \sim -13°$. Another long bed wave mode with negative ϑ, LM_4, is found at $k \sim 5.2$ rad/km (wavelength around 1.2 km) and $\vartheta \sim -11°$. For $\vartheta > 0°$, LM_5 occurs at $k \sim 2.4$ rad/km (wavelength around 2.7 km) and $\vartheta \sim 22°$, and LM_6 is found at $k \sim 4.2$ rad/km (wavelength

around 1.5 km) with $\vartheta \sim 16^\circ$. The e-folding times of the long bed wave modes from LM_2 to LM_6 are approximately 23, 22, 70, 30 and 29 times of the morphological time T_m, respectively. The wavelength and orientation of the local maxima agree quite well with those in Blondeaux et al. (2009). Generally, the differences in the e-folding times between the present results and those of Blondeaux et al. (2009) are within 15%. The reason for the differences is given in Section 2.4.

2.4 DISCUSSION

2.4.1 *Mechanism of the formation of large-scale bedforms*

The physical mechanisms causing the initial formation of tidal sand ridges and long bed waves have been discussed in several studies. Among many of the hypotheses, linear stability theory has been proven to be successful in explaining the characteristics of observed bedforms, which is also supported by the results in this chapter. The crucial aspect for both types of bedforms is the joint action of the background tidal current and the residual current that is generated by tide-topography interaction.

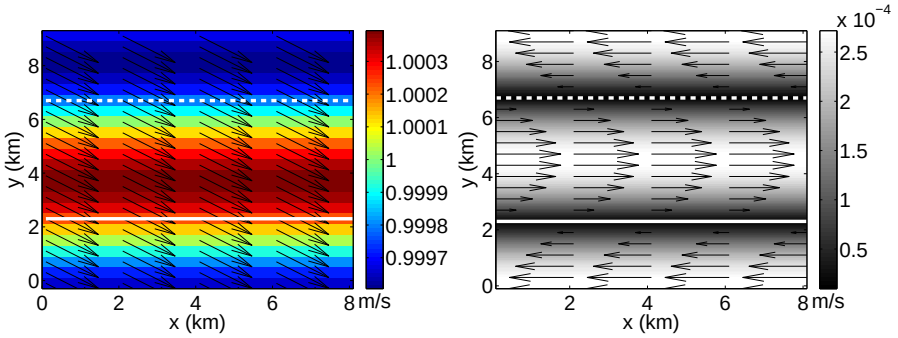

Figure 2.14: Tidal current patterns for the preferred bedform in Exp. 1. The solid/dashed line stands for the crest/trough of the bed perturbation. The principal direction of the basic flow is 35.8° clockwise rotated with respect to the x-axis. (a) Total tidal current during flood. The colormap/arrow indicates the magnitude/vector of the tidal current. Note that the current velocity is larger upstream of the crest and smaller downstream of the crest, which also occurs during ebb. (b) The residual current, with the colormap/arrow indicating its magnitude/vector. Note that the residual current is anticyclonic around the crest, and its magnitude is small because the amplitude of the bedform is small.

Regarding tidal sand ridges, Zimmerman (1981) used vorticity concepts to show that for a ridge that is obliquely oriented with respected to the tidal current, the frictional torque generates a residual current that acts with the tidal current on the upstream side of the ridges, whilst it acts against the tidal current on the downstream side (Fig. 2.14). The intensity of this residual current is maximum if the distance between successive ridges is of the order of the tidal excursion length U/ω (the distance travelled by particles in one tidal period). Here, U and ω are the characteristic current velocity amplitude and radian tidal frequency, respectively. As explained by Huthnance (1982a), since advective sand transport induced by the flow increases faster than linearly with the instantaneous current, sand transport on the upstream side is larger than that on the downstream side. In the case of a symmetric tidal current, this results in net accumulation of sand at the crest. On the other hand, the sand transport due to local bed slopes is directed downslope, thus this transport is divergent at the crests, which increases if ridges are spaced closer together (larger wavenumber k). The competition between advective and slope-induced sand transport gives rise to a fastest growing mode with a certain wavelength and orientation. In addition, if Coriolis torque is considered, it generates a residual flow in the same direction as that due to the frictional torque if the ridge is oriented cyclonically with respect to the tidal current. The opposite occurs if the ridge has an anticyclonic orientation with respect to the tidal current. Thus, convergence of advective sand transport at the crest is larger than that in the former case. This explains the preferred cyclonic orientation of tidal sand ridges. In the case of an asymmetric tidal current, Roos et al. (2001) and Walgreen et al. (2002) have shown that a flood-dominant current (the maximum flood current is larger than the maximum ebb current) causes convergence of advective sand transport to occur downstream of the crests, thereby affecting the growth of the ridges and causing the ridges to move downstream. If the current is ebb-dominant, i.e., the maximum ebb current is larger than the maximum flood current, the ridges migrate upstream.

Concerning long bed waves, it was demonstrated by Blondeaux et al. (2009) that they form if sand transport takes place during only part of the tidal cycle (tidal current amplitude slightly above the critical velocity for sand erosion) and the tidal current is elliptical. In those cases, the growth or decay of bedforms is determined by the joint action of the tidal current and the residual current that is calculated over the interval that the bed is active. For cyclonically oriented bedforms, the residual current is anticyclonic due to the combined effect of frictional torque and Coriolis torque. The residual current around anticyclonically oriented bedforms is generally weaker than that around cyclonically oriented bedforms. However, the residual current computed over the interval that the bed is active can be in the same order as that for cyclonically oriented bedforms and be cyclonic. As a result, bedforms with either cyclonic or anticyclonic orientation with respect to the tidal current occur.

2.4.2 *Differences between present results and those in previous studies*

Comparing the results of Exp. 1 (Fig. 2.4) with those in Hulscher et al. (1993), it turns out that the growth rate, wavelength and angle between the principal current direction and the crests of the fastest growing mode from the present model are slightly larger. The differences are caused by two reasons. First, Hulscher et al. (1993) used a harmonic truncation of the perturbed flow, in which the cut off took place after the second overtide of the principal M_2 constituent. In contrast, since the upper limit frequency of the harmonic components is determined by the time step in a numerical model, many more harmonic components generated by the basic current are included automatically in the present model. Second, Hulscher et al. (1993) neglected the $\partial\zeta/\partial t$ term in the continuity equation (rigid-lid approximation).

Comparison between the results in Exp. 9 (Fig. 2.13) and those in Blondeaux et al. (2009) shows marginal differences in the wavelength and orientation of the preferred bedforms, though slight differences in the growth rate are observed. The differences are attributed to the fact that the rigid lid approximation was used in their study, whereas the surface elevation $\tilde{\zeta}$ varies in time and space in the present model.

2.4.3 *Key parameters for the initial formation of tidal sand ridges*

Several parameters have been varied in this chapter to investigate whether they are essential for the initial formation of tidal sand ridges, i.e., linear versus nonlinear bottom friction, critical velocity for sand erosion, isotropic versus anisotropic slope-induced sand transport, tidal ellipticity and different tidal constituents.

Nonlinear bed shear stress is not crucial for the generation of tidal sand ridges (Fig. 2.5 in Exp. 2) Likewise, the anisotropic slope-induced sand transport is not crucial for the formation of the bedforms, albeit that the growth rate of the preferred bedforms is sensitive to the formulations of the slope-induced sand transport (Fig. 2.8 in Exp. 4). Compared to the case using linear bed shear stress, using nonlinear bed shear stress generates frictional torques with slightly different values, thereby giving rise to a different residual current, and further different advective sand transport. If anisotropic slope-induced sand transport is used, the coefficients for the slope-induced sand transport change, hence different divergent sand transport is obtained compared to the case in which isotropic slope-induced sand transport is used.

If the critical velocity is considered, the tidal current and the residual current in a tidal period are the same as that in the case in which the critical velocity is absent ($U_c = 0$). However, the net sand transport occurs only during the time that the bed is active. Hence both the advective and slope-induced sand transport differ from that in the case $U_c = 0$. If an elliptical tide instead of a rectilinear tide is considered (Fig. 2.9

in Exp. 5), both the advective and slope-induced sand transport change, which is due to the change in the tidal current and the residual current.

Different tidal constituents are not essential for the generation of the offshore tidal sand ridges. Nevertheless, compared to the case using only the principal semidiurnal tide, due to the change of the tidal current and the residual current, the advective and slope-induced sand transport alter accordingly. Hence bedforms with different characteristics appear, as has appeared from the results of the experiments with the diurnal tide (Fig. 2.10 in Exp. 6), the mixed tide (Fig. 2.11 in Exp. 7) and the spring-neap tide (Fig. 2.12 in Exp. 8).

2.4.4 *Comparison with field data*

In the southern North Sea, tidal sand ridges with different characteristics are observed (Fig. 1.2). The focus here is on the Dutch Banks and the Flemish Banks. The Norfolk Banks will be considered in further research.

Although the areas of the Dutch Banks and the Flemish Banks are characterized by the same mean water depth, compared to the Flemish Banks, the Dutch Banks have a larger wavelength. From Roos et al. (2004), the wavelength of the Dutch Banks is in the range of 5.7–9.8 km, and the orientation angle is $-25°$; near the Flemish Banks, the wavelength of the ridges is around 4.5 km, and the orientation angle is $-6°$. To explain the different appearance of the ridges mentioned above, several experiments were conducted, i.e., with/without elliptical tide and with/without critical velocity for sand erosion.

Topography, tidal conditions and the grain size information are based on those from Roos et al. (2004) and van Santen et al. (2011). In the model, a mean water depth of 29 m is used. At the Dutch Banks, the maximum velocity of the M_2 tide is chosen as 0.75 m s^{-1} with an ellipticity of -0.2, and the grain size is 0.25 mm. At the Flemish Banks, a stronger current with a velocity amplitude of 0.8 m s^{-1} and an ellipticity of 0.1 is employed, and the sand is coarser (0.45 mm). Using $\theta_c = 0.05$ yields values of the critical velocity for sand erosion U_c of 0.46 m s^{-1} and 0.59 m s^{-1} in the areas of the Dutch Banks and the Flemish Banks, respectively. A nonlinear bed shear stress with a constant drag coefficient C_d of 0.003 is used. The sand transport is calculated from Eq. 2.14, in which the parameters μ_d, K_G and s have the same values as those in Exp. 9. The modeled preferred bedforms in the areas of the Dutch Banks and the Flemish Banks have a wavelength of around 6.0 km and 5.2 km, respectively, which qualitatively agree with the observations. The e-folding times of the preferred bedforms are around 600 yr at both locations. If the critical velocity $U_c = 0$ and the ellipticity is kept the same as above, the wavelength of the preferred bedforms changes to 7.0 km for the Dutch Banks and 6.4 km for the Flemish Banks, and the e-folding time decreases to 360 yr and 280 yr, respectively. Furthermore, if the critical

velocity is included and rectilinear tides are used, the wavelengths of the preferred bedforms at both locations become 5.4 km, and the change in the e-folding time is within 50 yr compared to the experiment using both elliptical tides and the critical velocity. Hence the differences in the critical velocity for sand erosion (related to the grain size) and the tidal ellipticity might explain the different wavelengths of the ridges at those locations. The modeled orientation angles are around $-40°$ for all the experiments above, whilst the observed orientations are $-25°$ and $-6°$ for the Dutch Banks and the Flemish Banks, respectively.

It should be noted that the observed ridges have finite height. Nonlinear processes are likely to affect the wavelength of the bedforms during their long-term evolution. This behavior has been found in the case of other coastal bedforms, such as sand bars in the near shore zone (Garnier et al., 2006) and shoreface-connected sand ridges on the inner shelf (Nnafie et al., 2014b).

2.4.5 *Limitations*

The present model is idealized in the sense that several assumptions have been made. First, the depth-averaged shallow water equations are used, which means that the vertical flow structure is not considered. Hence the model is not able to simulate sand waves (Hulscher, 1996; Besio et al., 2006; Borsje et al., 2013). The differences between modeled and observed orientation of tidal sand ridges could also be attributed to that assumption, since the direction of the currents near the bottom may differ from that of depth averaged currents. Second, the domain size is assumed to be much smaller than the wavelength of tidal waves, so no phase differences of the background tidal waves are accounted for. Third, the model assumes a constant mean depth and periodic boundary conditions in all horizontal directions, thereby mimicking the situation on an open shelf, without considering the proximity of coasts. Fourth, the sand is uniform, so sorting processes (Walgreen et al., 2004; Roos et al., 2007) resulting in variation of mean grain size over the ridges are not accounted in the present model. Also note that although multiple tidal constituents in the forcing are considered, the residual flow and the nonlinear overtides of the principal tidal constituents are not included in this chapter. Finally, for simplicity, the orientations of tidal ellipses are chosen to be the same in the cases in which multiple tidal constituents are used.

2.4.6 *Choice of numerical aspects*

Regarding the choice of the bottom modes, the domain size (L_x, L_y) was chosen in the range of 1–36 km, and (k_x, k_y) were calculated from (L_x, L_y). In Exp. 1, 17×35 pairs of (k_x, k_y) were used. In the part of the $\vartheta - k$ parameter space where tidal sand

ridges were expected ($-60^\circ \leq \vartheta \leq -10^\circ$ and $0 \leq k \leq 1.5$ rad/km), a minimum of 25×20 pairs of (ϑ, k) were used. For Exp. 9, 57×25 pairs of (ϑ, k) were used.

Regarding the numerical settings, it has been demonstrated that using the grid size and time step mentioned in Section 2.2.5, the model results agree well with those of the previous studies. By using a smaller grid size $\Delta y = 100$ m and a time step $\Delta t = 5$ s instead of $\Delta y = 200$ m and $\Delta t = 10$ s for Exp. 1, it turned out that the relative change in the e-folding time of the fastest growing mode is 0.4%. Hence, the effect of the numerical discretization on the final results is very small. The initial amplitude of the bottom perturbation used in this chapter, i.e., $0.001H$, is adequate. Further experiments using amplitudes of $0.0001H$ and $0.01H$ of the bed perturbation for Exp. 1 revealed that the fastest growing mode has the same characteristics as that using $0.001H$.

2.5 CONCLUSIONS

Previous work has explained the mechanism of the generation of tidal sand ridges in coastal seas by free instability of the sandy bed subject to tidal currents. However, little attention has been paid to the effect of bed shear stress formulations (linear versus nonlinear), tidal characteristics (tidal ellipticity, different tidal constituents) and sand transport formulations on the characteristics (growth rate, wavelength, and orientation) of these large-scale bedforms during their initial formation. To this end, an idealized nonlinear numerical model was developed, which describes the interaction between depth-averaged tidal currents and the sandy bed. The results demonstrate that the present model is able to reproduce the initial formation of tidal sand ridges and long bed waves as were found in earlier studies that employed linear stability analysis (Hulscher et al., 1993; Blondeaux et al., 2009). The advantage of the present approach is that it offers a framework to study the long-term nonlinear evolution of these bedforms, which will be done in the following chapters.

For tidal sand ridges, using nonlinear bed shear stress and anisotropic slope-induced sand transport causes a slight increase of the growth rate and a decrease of the wavelength of the preferred bedforms. Furthermore, if the critical depth-averaged velocity for sand erosion is increased, the growth rate of the preferred bedforms becomes smaller, as well as the wavelength and the angle between the principal current direction and the crests. Note that besides tidal sand ridges, long bed waves could also emerge if the critical velocity is close to the maximum current velocity. The changes of the growth rate, wavelength and orientation angle of the preferred bedforms due to changing tidal ellipticity are non-monotonic: the largest growth rate and the smallest orientation angle are found around $\epsilon = -0.2$, and the smallest wavelength is found around $\epsilon = 0.2$. The combined effect of the critical velocity for sand erosion and elliptical tides might explain the difference in the wavelength at the Dutch Banks and the Flemish Banks in the North Sea. Using a diurnal tide increases the wa-

velength of the preferred bedforms significantly, while the orientation angle slightly decreases and the growth rate barely varies. The characteristics of the preferred bedforms are determined by the dominant tidal constituent if tidal currents with more than one constituents are considered. At locations dominant by the mixed tides, if the semidiurnal tide is known, as the amplitude of the diurnal tide increases, both the growth rate and the wavelength of the preferred bedforms increase. In the case of spring-neap tide dominant areas, if the representative current velocity is fixed, the growth rate hardly changes, while the bedforms with longer wavelength are found if the amplitudes of the two semidiurnal tides are close to each other. The change in the orientation of the preferred bedforms is insignificant for mixed tides and spring-neap tides. Furthermore, it is confirmed that long bed waves appear if the critical velocity for sand erosion is slightly smaller than the maximum current velocity.

2.A DERIVATION OF GOVERNING EQUATIONS FOR TIDAL CURRENTS

To derive the governing equations for the currents (Eqs. 2.4 and 2.5), plugging $\zeta = \zeta_0 + \tilde{\zeta}$ and $D = \tilde{D} + \zeta_0$ into Eqs. 2.1 and 2.2 gives

$$\frac{\partial(\tilde{\zeta}+\zeta_0)}{\partial t} + \nabla\cdot((\tilde{D}+\zeta_0)\vec{u}) = 0, \tag{2.A1}$$

$$\frac{\partial \vec{u}}{\partial t} + (\vec{u}\cdot\nabla)\vec{u} + f\vec{e}_z\times\vec{u} = -g\nabla(\tilde{\zeta}+\zeta_0) - \frac{\vec{\tau}_b}{\rho(\tilde{D}+\zeta_0)}. \tag{2.A2}$$

The equations above are rearranged as

$$\frac{\partial \tilde{\zeta}}{\partial t} + \nabla\cdot(\tilde{D}\vec{u}) + \frac{\partial \zeta_0}{\partial t} + \nabla\cdot(\zeta_0\vec{u}) = 0, \tag{2.A3}$$

$$\frac{\partial \vec{u}}{\partial t} + (\vec{u}\cdot\nabla)\vec{u} + f\vec{e}_z\times\vec{u} = -g\nabla\tilde{\zeta} - g\nabla\zeta_0 - \frac{\vec{\tau}_b}{\rho(\tilde{D}+\zeta_0)}. \tag{2.A4}$$

Writing $\zeta_0 = D_0 - H$, and $\vec{u} = \vec{u}_0 + \vec{\tilde{u}}$, with $\vec{\tilde{u}}$ representing the velocity due to bottom perturbations, the sum of the last two terms on the left hand side of Eq. 2.A3 is shown to be approximately 0 as follows,

$$\frac{\partial \zeta_0}{\partial t} + \nabla\cdot(\zeta_0\vec{u}) = \frac{\partial \zeta_0}{\partial t} + \nabla\cdot\big((D_0-H)(\vec{u}_0+\vec{\tilde{u}})\big) = \nabla\cdot\big((D_0-H)\vec{\tilde{u}}\big). \tag{2.A5}$$

Here, the continuity equation $\partial\zeta_0/\partial t + \nabla\cdot(D_0\vec{u}_0) = 0$ and $\nabla\cdot(H\vec{u}_0) = 0$ are used. From $|\zeta_0| \ll H$, $D_0 - H \approx 0$, also $|\vec{\tilde{u}}|$ is small. Therefore, the new continuity equation Eq. 2.4 is obtained. The depth $\tilde{D}$ is in the same order of the mean water depth H, thus $|\zeta_0| \ll \tilde{D}$, and $1/(\tilde{D}+\zeta_0) \approx 1/\tilde{D}$. Furthermore, using $\vec{F}_p = -g\nabla\zeta_0$, the new momentum equation Eq. 2.5 is derived.

3

MODELING THE FINITE-HEIGHT BEHAVIOR OF OFFSHORE TIDAL SAND RIDGES

3.1 INTRODUCTION

As was described in Chapter 1, several simplifications were used in the previous studies on the finite-height behavior of tidal sand ridges. Either limited sand availability was assumed (Huthnance, 1982b), or a 1D configuration (the topography varies only in one horizontal dimension) was applied (Huthnance, 1982a; Roos et al., 2004), or the background tidal current was almost circular, i.e., its ellipticity is close to 1 (Tambroni and Blondeaux, 2008). Besides, only in Tambroni and Blondeaux (2008) the critical bed shear stress for sand erosion was considered. Other studies either neglected the nonlinear interaction of bottom modes with different wavelengths (Idier and Astruc, 2003) or gave characteristics of modeled ridges that did not agree with those of the observed ridges (Komarova and Newell, 2000).

The research in this chapter has two objectives. The first is to quantify the differences in the characteristics of finite-height tidal sand ridges, i.e., their shape and growth time, between cases in which either a 1D or a 2D configuration is assumed with unlimited sand, rectilinear tides and no critical bed shear stress for sand erosion. The second is to study the sensitivity of the characteristics of the finite-height ridges to elliptical tides and the critical bed shear stress for sand erosion. In addition, qualitative comparison between modeled and observed ridges in the southern North Sea will be done. To achieve these objectives, an extended version of the morphodynamic model in Chapter 2 will be considered. The extension concerns the consideration of

This chapter is based on:
Yuan, B., de Swart, H. E., Panadès, C., 2017. Modeling the finite-height behavior of offshore tidal sand ridges, a sensitivity study. *Continental Shelf Research* 137, 72–83.

the stirring of sand by wind waves in the formulation for sand transport (Huthnance, 1982a,b; Roos et al., 2004) .

In Section 3.2, first the extended morphodynamic model is introduced, followed by a description of numerical implementation, quantities for the characteristics of finite-height bedforms and the design of the experiments. Section 3.3 and Section 3.4 contain results and discussion, respectively. Last, Section 3.5 presents conclusions.

3.2 MATERIAL AND METHODS

Compared to the model shown in Section 2.2.1, the model in this chapter takes into account the stirring of sand by wind waves in the formulation of sand transport as in Roos et al. (2004).

3.2.1 *Formulations of bed shear stress and sand transport*

The bed shear stress $\vec{\tau}_b$ is related to the depth-averaged current velocity through the drag coefficient C_d by the quadratic friction law

$$\vec{\tau}_b = \rho C_d |\vec{u}| \vec{u}, \qquad C_d = [2.5 \ln(11\tilde{D}/k_s)]^{-2}, \tag{3.1}$$

where k_s is the Nikuradse roughness that measures the roughness of the sea bed. In the presence of ripples, k_s is related to the dimensionless grain size D_* (Soulsby and Whitehouse, 2005) by

$$k_s = 202\, d\, D_*^{-0.554}, \qquad D_* = \left[\frac{g(s-1)}{\nu^2}\right]^{1/3} d. \tag{3.2}$$

Here, s is the ratio of densities of non-cohesive sand and water, d is the median grain diameter, and ν is the kinematic viscosity of water.

For sand transport, a bed load formulation is used. The formulation for sand transport is a modified version of that of Fredsøe and Deigaard (1992):

$$\vec{q} = \alpha_e (u_e^2 - U_c^2)(1 - 0.7 U_c/u_e)\,(\vec{u} - \Lambda u_e \nabla h)\,\mathscr{H}(u_e - U_c). \tag{3.3}$$

In this expression, α_e is the sand transport coefficient given by

$$\alpha_e = \frac{30}{\mu_d \pi C'^3} \frac{1}{(s-1)g}, \tag{3.4}$$

where μ_d is the dynamic friction coefficient and $C' = 2.5 \ln(11\tilde{D}/2.5d)$ is the grain-related conductance coefficient. The critical depth-averaged velocity for sand erosion U_c is obtained from

$$U_c = C'[(s-1)\, g\, d\, \theta_c]^{1/2}, \tag{3.5}$$

with θ_c being the critical Shields parameter. To calculate θ_c, an empirical relation through the dimensionless grain size D_* is used (Soulsby and Whitehouse, 1997):

$$\theta_c = \frac{0.3}{1+1.2D_*} + 0.055\left[1-e^{-0.02D_*}\right]. \tag{3.6}$$

The modification concerns the wave stirring effect on sand transport and the slope-induced transport. The wave stirring effect on sand transport is included by using an effective velocity u_e in the sense of stirring sand, given by $u_e^2 = |\vec{u}|^2 + 0.5u_w^2$, where u_w is the amplitude of the depth-dependent wave-induced near-bed orbital velocity. Following Roos et al. (2004), the velocity u_w is parameterized as

$$u_w = U_w\left(\frac{H}{\widetilde{D}}\right), \tag{3.7}$$

in which U_w represents the near-bed orbital velocity amplitude in the absence of bottom undulations. Hereafter U_w is called wave stirring coefficient as in Roos et al. (2004). Furthermore, isotropic instead of anisotropic slope-induced sand transport is employed with a bed slope coefficient Λ, which is often used for bed load transport (e.g. Bailard and Inman, 1981). Finally, the Heaviside function $\mathscr{H}$ is used to guarantee that sand transport only occurs if $u_e > U_c$.

3.2.2 *Numerical implementation*

Since the morphological time scale of offshore large-scale bedforms is much larger than the time scale of tides, a morphological acceleration factor β (Roelvink, 2006) is introduced into Eq. 2.8 (replace $\partial h/\partial t$ by $\partial h/\partial(\beta t)$) to accelerate the morphodynamic processes.

The finite-height behavior of sand ridges is investigated by simulating the long-term evolution of bed perturbations that initially have a small amplitude in a finite domain subject to tidal forcing. Here, background tidal currents are characterized by a single angle φ between the major axes of the ellipses of the tidal constituents and the x-axis. Angle φ and domain length L_y are linked to the orientation ϑ_p of the crests with respect to the principal current direction and the wavelength λ_p of the initially fastest growing bottom mode (or the initially preferred bedform/mode). Values of ϑ_p and λ_p (or wavenumber $k_p = 2\pi/\lambda_p$) are computed a priori by applying linear stability analysis (Huthnance, 1982a) and are thus known. Negative ϑ_p means that the crests of the bedforms are rotated cyclonically with respect to the principal current direction. The chosen set-up is that $\varphi = \vartheta_p$ and $L_y = N\lambda_p$ with N an integer. This implies that the domain is chosen such that the initially preferred bedform has its crests parallel to the x-axis and it fits into the domain. Regarding the domain length in the x-direction L_x, three grid points (two are boundary points) are used in the case of a 1D configuration, i.e., $L_x = 3\Delta x$, with Δx being the grid size in the x-direction.

Regarding a 2D configuration, L_x is chosen based on a bottom mode with a wave vector $(k_{x0}, 0)$, i.e., $L_x = 2\pi/k_{x0}$, such that $k_{x0} \simeq k_p$. As default, initially random bed perturbations are imposed with a small amplitude (approximately $0.001H$).

3.2.3 *Quantities to describe characteristics of finite-height bedforms*

The root mean square height of the bedforms $h_{rms} = (\overline{h^2})^{\frac{1}{2}}$ represents the variance the bedforms, where the overbar denotes spatial averaging, $(L_x L_y)^{-1} \int_0^{L_x} \int_0^{L_y} \cdot\, dx\, dy$. The potential energy of the bedforms is thus measured by $h_{rms}^2/2$. The bedforms at any time contain Fourier components with wave vectors $(k_x, k_y) = \left(\frac{2m\pi}{L_x}, \frac{2n\pi}{L_y}\right)$, i.e.,

$$h = \sum_m \sum_n a_{mn} e^{2\pi \mathrm{i}(mx/L_x + ny/L_y)}. \tag{3.8}$$

Here, m and n are integers, $-\frac{L_x}{2\Delta x} \le m \le \frac{L_x}{2\Delta x}$, $-\frac{L_y}{2\Delta y} \le n \le \frac{L_y}{2\Delta y}$, with Δy being the grid size in the y-direction, and a_{mn} represents the complex amplitude of the corresponding component, which is obtained from inverse Fourier transform. A bottom mode consists of components with wave vectors $\pm(k_x, k_y)$. The potential energy of the bedforms is computed as $\sum_m \sum_n |a_{mn}|^2/2$.

To describe the growth or decay of the amplitude of the bedforms, a global growth rate Γ of the bedforms is computed (Garnier et al., 2006), which reads

$$\Gamma = \frac{1}{(h_{rms}^2)} \frac{\partial}{\partial t} \left(\frac{1}{2} h_{rms}^2 \right). \tag{3.9}$$

A static equilibrium state of the growth of finite-height bedforms is reached if Γ remains 0, while a dynamic equilibrium state of the growth of finite-height bedforms is obtained if Γ oscillates around 0 in time. Typically, in the case of an initially random bed perturbation, Γ changes its sign after a period during which the amplitudes of the bottom modes grow exponentially. In this chapter, a global growth time τ_g is defined as the time when Γ turns negative after the exponential growth of the bottom modes.

In the presence of asymmetric tidal current (unequal strength of flood and ebb), the bedforms migrate and show asymmetrical profiles (Huthnance, 1982a). To describe the cross-sectional (normal to crests) profiles of the bedforms, the relative height h_{rel} and asymmetry A defined in Roos et al. (2004) are used:

$$h_{rel} = \frac{|z_{tr}| - |z_{cr}|}{|z_{tr}|}, \qquad A = \ln\left(\frac{l_1}{l_2}\right). \tag{3.10}$$

In these expressions, $|z_{tr}|$ and $|z_{cr}|$ are the distances between the reference sea level and the trough/crest level, and l_1 and l_2 are the horizontal distances from the crest

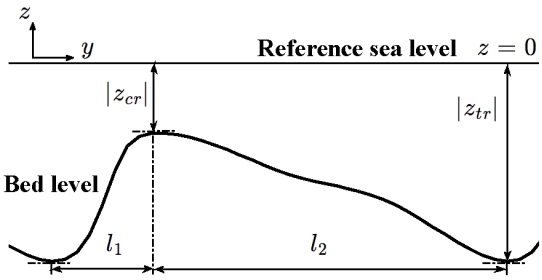

Figure 3.1: Sketch showing how quantities z_{cr} and z_{tr} (crest and trough levels), and length scales l_1, l_2 are obtained from model output. From these quantities, the relative height h_{rel} and asymmetry A of the bedforms are calculated from Eq. 3.10. Here $A < 0$.

to the neighboring troughs (Fig. 3.1). Recall that the crests of the initially preferred bedform are parallel to the x-axis. As most spatial variation of the bedforms is expected in the y-direction, only l_1 and l_2 along the y-axis are presented. The distances l_1 and l_2 are measured in the positive y-direction, such that $A > 0$ indicates that the steeper side with respect to the crest is in the positive y-direction when measured from the crest.

3.2.4 *Design of experiments*

To fulfill the two main aims of this chapter, two groups of experiments are designed. Default parameter values for hydrodynamics, sand transport and numerics are listed in Table 3.1. The chosen physical parameter values represent typical conditions at the outer shelf of the southern North Sea. Experiments of the first group are carried out to quantify the differences in the characteristics of finite-height tidal sand ridges, i.e., their shape and growth time, using 1D and 2D configurations under a rectilinear ($\epsilon = 0$) semidiurnal tide M_2 with no critical bed shear stress for sand erosion ($U_c = 0$).

In the second group of experiments, the focus is on exploring separately the effect of the tidal ellipticity ϵ and the critical bed shear stress, or equivalently the critical velocity U_c for sand erosion, on the characteristics of finite-height ridges. If an elliptical tidal current ($\epsilon = -0.4, -0.2, 0.2, 0.4$) is used, $U_c = 0$, while if the critical shear stress is included, $\epsilon = 0$. The values of the tidal ellipticity and the grain size in this chapter are based on the reconstructed tidal currents from the results of a numerical model and field data that are both presented in van Santen et al. (2011).

Accounting for the subharmonics of the initially preferred bedform, i.e., modes with wavenumbers $(0, k_p/I)$ (I is an integer larger than 1), increases the complexity

Table 3.1: Default parameter values for hydrodynamics, sand transport and numerics in the experiments. An M_2 background tidal current is considered, unless otherwise specified.

	Parameter	Value	Description
Hydrodynamics	H	30 m	Undisturbed water depth
	U_{max}	1 m s^{-1}	Maximum velocity of background tidal current
	Φ	52° N	Latitude
	Ω	7.292×10^{-5} rad s^{-1}	Angular frequency of the Earth
	g	9.81 m s^{-2}	Gravitational acceleration
	U_w	0.25 m s^{-1}	Near-bed wave stirring coefficient
	ν	1.4×10^{-6} m^2 s^{-1}	Kinematic viscosity of water
	ω_{M_2}	1.4×10^{-4} rad s^{-1}	Angular frequency of M_2 tide
Sand transport	s	2.6	Density ratio between sand and water
	p	0.4	Bed porosity
	Λ	2.0	Bed slope coefficient
	μ_d	0.6	Dynamic friction coefficient
	d	0.4 mm	Median grain size
Numerics	Δx	400 m	Grid size in the x-direction
	Δy	200 m	Grid size in the y-direction
	Δt	8 s	Time step
	β	25–450	Morphological acceleration factor

of the system. Therefore, in Section 3.3 the domain length L_y is chosen as the wavelength of the initially preferred bedform. Consequently, the modes with $k_x = 0$ only include the initially preferred bedform and its superharmonics ($k = Ik_p$), as made visible as squares in Fig. 3.2, which is a contour plot of the initial growth rate of bottom modes in the topographic wavenumber space. Additionally, the circles in Fig. 3.2 denote several bottom modes with wave vectors normal/oblique to that of the preferred bedform in a 2D configuration. Simulations that include subharmonics of the preferred bedform will be discussed in Section 3.4.

Note that in the main part background tidal currents with multiple constituents, e.g. M_0, M_2 and its first overtide M_4 (with angular frequency $\omega_{M_4} = 2\omega_{M_2}$), are only considered when situations at specific field sites are mimicked (in Section 3.4). Further information of the effect of considering more than one tidal constituent on the characteristics of finite-height ridges is given in the appendices.

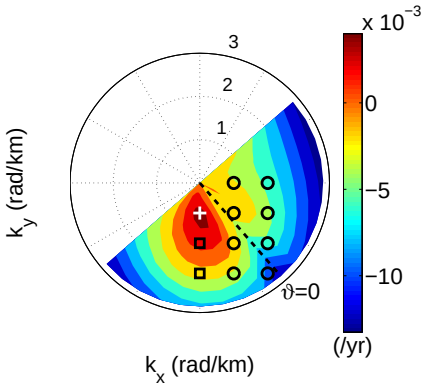

Figure 3.2: An example of the initial growth rate of bottom modes as a function of the topographic wavenumbers k_x and k_y of the modes, obtained from linear stability analysis. The x- and y-axes are chosen such that the preferred bedform has a wave vector $(0, k_p)$. The black dashed line $\vartheta = 0$ indicates that the crests of the modes align with the principal current direction. The plus and squares correspond to the preferred bedform and two of its superharmonics, respectively. The circles denote several additional modes with crests normal/oblique to those of the preferred bedform in a 2D configuration.

3.3 RESULTS

3.3.1 *Rectilinear tides and no critical bed shear stress for sand erosion: 1D versus 2D configuration*

Fig. 3.3 shows snapshots of the bed level h at several times in the experiments using a rectilinear M_2 background tidal current and no critical bed shear stress for sand erosion ($U_c = 0$) for both 1D and 2D configurations. Based on the wavelength and orientation of the preferred bedform, the domain length $L_y = 9$ km, and the principal current direction is 41° clockwise rotated with respect to the x-axis. In a 2D configuration, the domain length $L_x = 8$ km. Due to the selection of the bottom modes, rhythmic bottom patterns appear in both 1D and 2D cases (Figs. 3.3a-b). Subsequently, the crests of the bedforms reach a high level, and in the 2D case they become parallel to the x-axis (Fig. 3.3c). Afterwards, the change in the bed level is minor in the 1D case, while in the 2D case meandering crests appear in space (Fig. 3.3d). In Fig. 3.4 the time evolution of the bed level h of a slice along the y-direction is shown for both 1D and 2D configurations. During the first 2000 yr, the bed level evolves similarly in the two cases, while afterward it behaves quite differently. In the 1D case, after a certain time the bed level does no longer change, a result that was also found

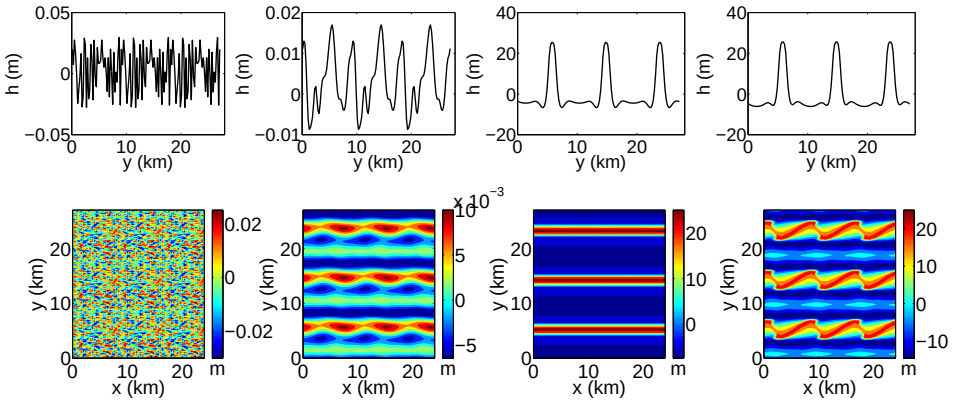

(a) $t = 0$ (b) $t = 500$ yr (c) $t = 2600$ yr (d) $t = 3600$ yr

Figure 3.3: Snapshots of the bed level h for both 1D (top) and 2D (bottom) configurations at times: (a) $t = 0$, (b) $t = 500$ yr, (c) $t = 2600$ yr, (d) $t = 3600$ yr, using a rectilinear M_2 background tidal current and $U_c = 0$. In the 2D case, the bed level obtained in the domain of 8 km×9 km is used to cover a domain with a size 3×3 times larger. Similar extension in the y-direction is done for the 1D case.

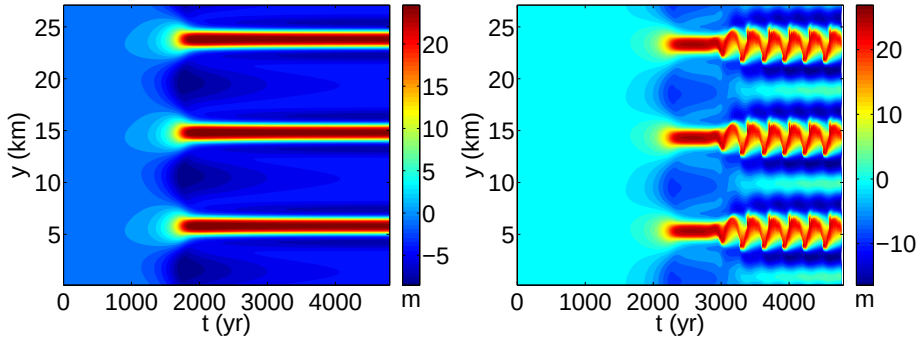

(a) 1D (b) 2D

Figure 3.4: Time evolution of the bed level of a slice along the y-direction in the cases using a rectilinear M_2 background tidal current and $U_c = 0$, for (a) a 1D configuration and (b) a 2D configuration. The bed level obtained in a domain with $L_y = 9$ km is used to cover a domain with L_y that is 3 times larger. In (b), $L_x = 8$ km, and the slice was taken at $x = 3.2$ km.

by Roos et al. (2004) (for a detailed comparison see Appendix 3.A). In contrast, if a 2D configuration is used, after about 3000 yr the crests of the bedforms begin to oscillate in time. The oscillation of the crests has a period of roughly 300 yr, and the distance that the crests shift in the y-direction is approximately 2.4 km.

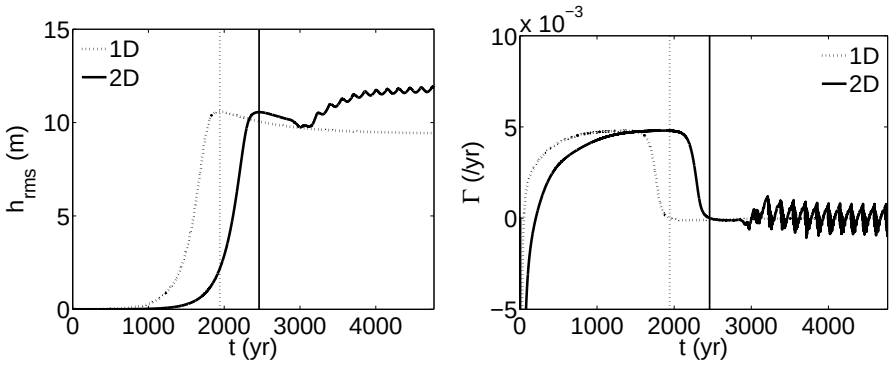

(a) h_{rms} (b) Γ

Figure 3.5: Time evolution of (a) root mean square height h_{rms} and (b) global growth rate Γ of the bedforms in the cases using a rectilinear M_2 background tidal current and $U_c = 0$, for both 1D (dotted line) and 2D (solid line) configurations. The vertical lines mark the global growth time τ_g of the bedforms.

In Fig. 3.5, the time evolution of the root mean square height h_{rms} and the global growth rate Γ of the bedforms are shown for both 1D and 2D configurations. It is seen that for a 2D configuration, the global growth time τ_g (2500 yr) of the bedforms is larger than that in the case of a 1D configuration (1900 yr). For time $t < \tau_g$, the time evolution of h_{rms} and Γ of the bedforms is similar for the 1D and 2D configurations, although a time difference of 600 yr is observed. For t slightly larger than τ_g, the global growth rate in the 2D case starts to oscillate around 0 (dynamic equilibrium) instead of infinitely approaching 0 (static equilibrium) as in the 1D case. In the end, in the 1D case h_{rms} and the relative ridge height h_{rel} (not shown) become almost constant, whereas in the 2D case these quantities oscillate in time. The relative height of the ridges in the transect at $x = 3.2$ km in the 2D case is 87±10% for time $t > \tau_g$, the mean value of which is close to that in the 1D case. As meanders could appear in the 2D case, hereafter, the results using a 2D configuration are presented, unless otherwise specified.

3.3.2 *Elliptical tides and critical bed shear stress for sand erosion*

In Fig. 3.6, the time series of the characteristics of the bedforms (h_{rms} and Γ) are shown for the experiments that consider M_2 background tidal currents with different values of tidal ellipticity ϵ and no critical bed shear stress for sand erosion. Results of the experiments using a 1D configuration are presented in Appendix 3.B. The wavelength of the initially preferred bedform is largest (11.2 km) for $\epsilon = -0.4$ and

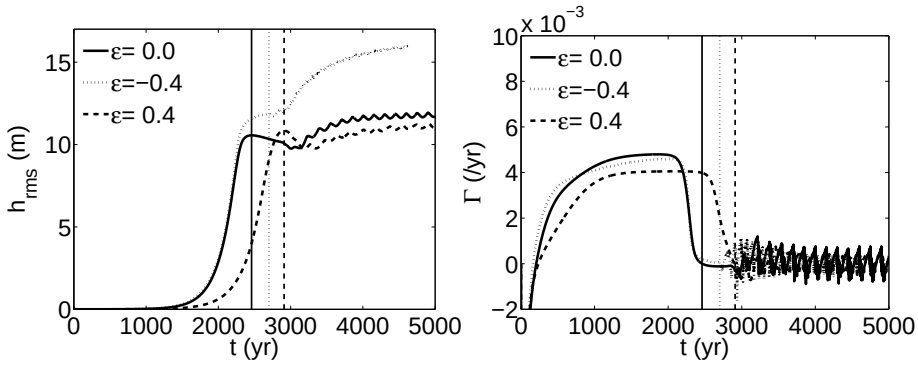

(a) h_{rms} (b) Γ

Figure 3.6: As Fig. 3.5 but for different values of ellipticity ϵ and $U_c = 0$. The case $\epsilon = 0$ is identical to the 2D case in Fig. 3.5.

smallest (8.6 km) for $\epsilon = 0.2$. The temporal behavior of Γ reveals that for all values of ϵ ($\epsilon = \pm 0.2$ not shown), similar to the case of a rectilinear tide, a dynamic equilibrium state is reached. In the case of cyclonic tidal currents ($\epsilon > 0$), for time $t > \tau_g$ the time-averaged value of h_{rms} decreases as the value of ϵ increases. In contrast, for anti-cyclonic tidal currents ($\epsilon < 0$), for time $t > \tau_g$ the time-averaged value of h_{rms} increases as the value of $|\epsilon|$ increases. Fig. 3.7a shows the dependence of the global growth time τ_g on the tidal ellipticity ϵ. Clearly, this dependence is non-monotonic, i.e, τ_g reaches a minimum at $\epsilon = -0.2$ and a maximum at $\epsilon = 0.4$. Besides, noticeable differences in the crest and trough levels for different values of ϵ are observed, which for each ϵ gives a large variation in the values of h_{rel}. Fig. 3.7b shows the range of relative ridge height h_{rel} for time $t > \tau_g$ against ϵ. For $t > \tau_g$, the maximum of h_{rel} for each ϵ is around 93%, while the minimum of h_{rel} changes from 85% at $\epsilon = -0.2$ to 48% at $\epsilon = 0.4$. Furthermore, Fig. 3.7c shows the period of the oscillation of the crests T_c and the distance l_c that the crests shift in the y-direction versus ϵ. It is seen that T_c increases as ϵ increases, and l_c varies between 2 km and 3.5 km. Note that l_c is larger for negative ϵ than for positive ϵ.

Next, the sensitivity of the characteristics of the bedforms to the critical velocity U_c for sand erosion is examined. In the case that $U_c > 0$, for the default value of the undisturbed water depth ($H = 30$ m, see Table 3.1), initially $U_c = 0.48$ m s^{-1}, and the initially preferred bedform has a smaller wavelength (8 km) than that (9 km) in the case that $U_c = 0$. Meandering crests that oscillate in time are also observed when $U_c > 0$ (not shown). The period of the oscillation of the crests is around 400 yr, and the distance that the crests shift in the y-direction is approximately 2.4 km. Another essential difference of the characteristics of the bedforms between the cases that $U_c = 0$ and $U_c > 0$ concerns the global growth time τ_g. In the latter case, τ_g is 500 yr larger. The other quantities (h_{rms} and h_{rel}) of the bedforms are only slightly

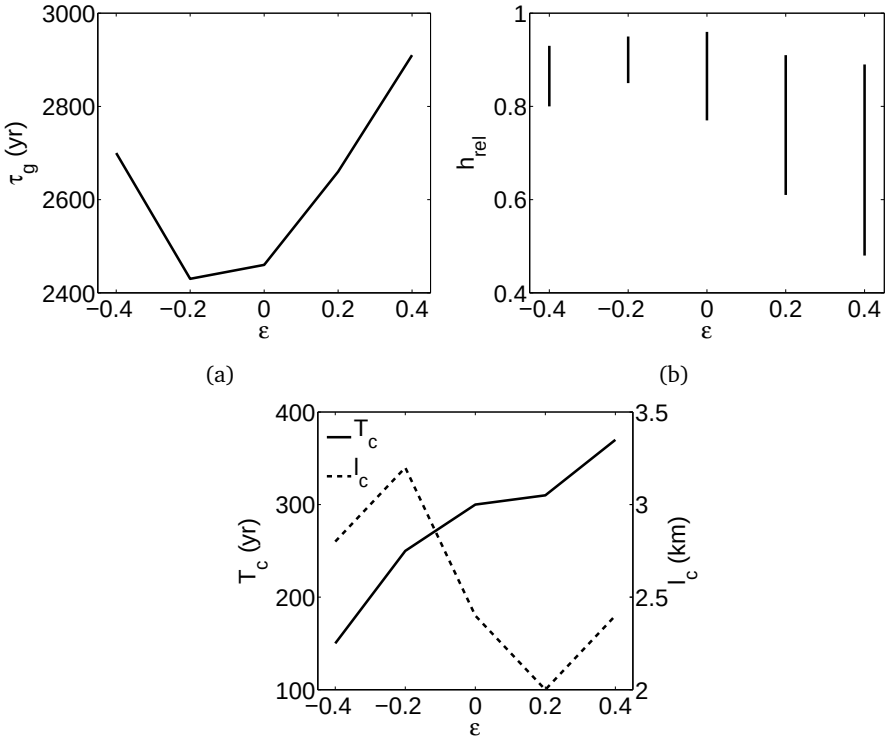

Figure 3.7: (a) Global growth time τ_g versus tidal ellipticity ϵ. (b) As (a), but for relative ridge height h_{rel} in the dynamic equilibrium state ($t > \tau_g$). (c) As (b), but for the period T_c (solid line) of the oscillation of the crests and the distance l_c that the crests shift in the y-direction (dashed line).

affected if $U_c > 0$ is considered. In particular, at time $t = \tau_g$, the relative differences in h_{rms} and h_{rel} between the cases that $U_c > 0$ and $U_c = 0$ are approximately 0.3% and 0.8%, respectively.

3.4 DISCUSSION

3.4.1 *Tendency of tidal sand ridges towards static equilibrium*

In the experiments using a 1D configuration, finite-height tidal sand ridges in static equilibrium are obtained with the present model, i.e., the global growth rate Γ of the bedforms in the end state remains zero. In contrast, in the experiments using a

2D configuration in Section 3.3, ridges in dynamic equilibrium are observed, i.e., Γ oscillates in time. To further understand why tidal sand ridges in static equilibrium occur, the potential energy of the bedforms (measured by $h_{rms}^2/2$) is analyzed. From the equation of bed level evolution (Eq. 2.8), the equation for the evolution of the potential energy is derived, which reads

$$\frac{\partial}{\partial t}\left(\frac{1}{2}h_{hrms}^2\right) = \frac{\overline{-h\nabla\cdot\langle\vec{q}_a\rangle}}{1-p} + \frac{\overline{-h\nabla\cdot\langle\vec{q}_s\rangle}}{1-p}. \tag{3.11}$$

Here, $\vec{q}_a$ and $\vec{q}_s$ are the advective and slope-induced sand transport, respectively,

$$\begin{aligned}\vec{q}_a &= \alpha_e(u_e^2-U_c^2)(1-0.7U_c/u_e)\,\vec{u}\,\mathscr{H}(u_e-U_c),\\ \vec{q}_s &= \alpha_e(u_e^2-U_c^2)(1-0.7U_c/u_e)\,(-\Lambda u_e\nabla h)\,\mathscr{H}(u_e-U_c).\end{aligned} \tag{3.12}$$

By applying the Green's theorem and periodic boundary conditions, the first and second terms on the right hand side of Eq. 3.11 are written as

$$\begin{aligned}P &= \frac{\overline{\left\langle\alpha_e(u_e^2-U_c^2)(1-0.7U_c/u_e)(\nabla h\cdot\vec{u})\mathscr{H}(u_e-U_c)\right\rangle}}{1-p},\\ \Delta &= -\frac{\overline{\left\langle\alpha_e(u_e^2-U_c^2)(1-0.7U_c/u_e)\,\Lambda u_e\,\mathscr{H}(u_e-U_c)\right\rangle(\nabla h\cdot\nabla h)}}{1-p}.\end{aligned} \tag{3.13}$$

Here, P describes the production of the potential energy due to advective sand transport $\vec{q}_a$, and Δ describes the damping of the potential energy due to slope-induced sand transport $\vec{q}_s$. Note that Δ is proportional to $-\overline{\nabla h\cdot\nabla h}$, and thus its value is negative.

Fig. 3.8a shows the time evolution of the production and damping terms P and Δ of the potential energy and their sum in the experiment using a rectilinear M_2 background tide, critical velocity $U_c = 0$ and a 1D configuration in Section 3.3.1. It is seen that the balance of the production term P and the damping term Δ in the end gives rise to a state in which the potential energy of the bedforms remains constant. Initially (for time $t \lesssim 1600$ yr) the magnitudes of both P and Δ increase. At this stage, since the bed slope $|\nabla h|$ is small, the magnitude of Δ is smaller than that of P. As the potential energy increases, the bed slopes become larger, giving rise to a fast increase in Δ. The final balance between the production term P and the damping term Δ results from a more vigorous increase in Δ caused by the increasing bottom slopes, rather than by the vanishing of P. The fact that P remains positive, even for a large value of h_{rms} (see Fig. 3.5a), indicates that the mechanism that causes initial growth of tidal sand ridges (see Huthnance, 1982a) also persists when sand ridges have finite heights. If wind waves are present, as the near-bed wave orbital velocity amplitude is inversely proportional to the water depth, bottom erosion due

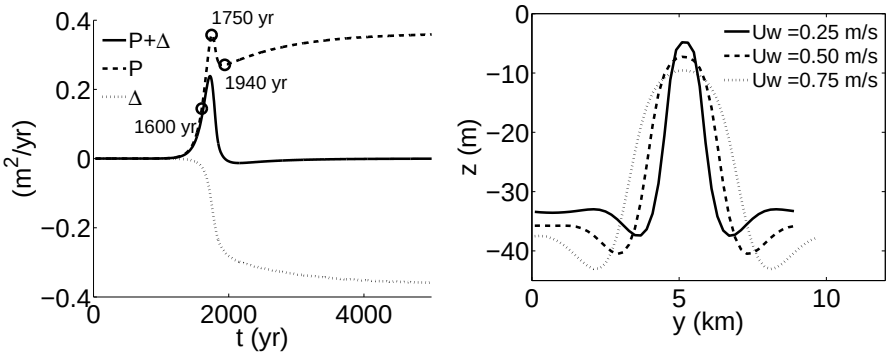

(a) (b)

Figure 3.8: (a) The production and damping terms P (dashed line) and Δ (dotted line) of the potential energy and their sum (solid line) versus time, from the experiment using a rectilinear M_2 background tidal current, $U_c = 0$ and a 1D configuration in Section 3.3.1. Several times are also indicated by circles. (b) Ridge profiles in equilibrium for different values of near-bed wave stirring coefficient U_w, using the same experiment setup as that for (a) except the value of U_w.

to wave stirring will prevent the crest level from growing too close to the surface level. Fig. 3.8b shows the ridge profiles (1D configuration) in equilibrium using different values of the near-bed wave stirring coefficient U_w. It is seen that as U_w increases, the depth above the crests increases and the crests become flatter.

3.4.2 *Presence of tidal sand ridges with meandering crests*

In Section 3.3.1, in the case of a 2D configuration, ridges appear with meandering crests that oscillate in time. The spatial characteristics of the ridges indicate the existence of bottom modes with wave vectors in different directions. To investigate this in more depth, the amplitude $|a_{mn}|$ of different bottom modes are analyzed. Fig. 3.9 shows the amplitude of the bottom modes at several times. It turns out that several bottom modes with crests that are oblique to those of the preferred bedform are excited at 3600 yr, which induces the meandering feature in space. Meanwhile, the temporal variations in the potential energy (measured by $|a_{mn}|^2$ for a single bottom mode) of those excited modes, the preferred bedform and its first few superharmonics cause the oscillation of the crests in time. The phenomenon that meandering crests of sand ridges evolve from straight crests is qualitatively similar to that of finite-amplitude plane waves of large steepness developing into three-dimensional (3D) crescent water waves due to nonlinear instability (Dias and Kharif, 1999, and references therein).

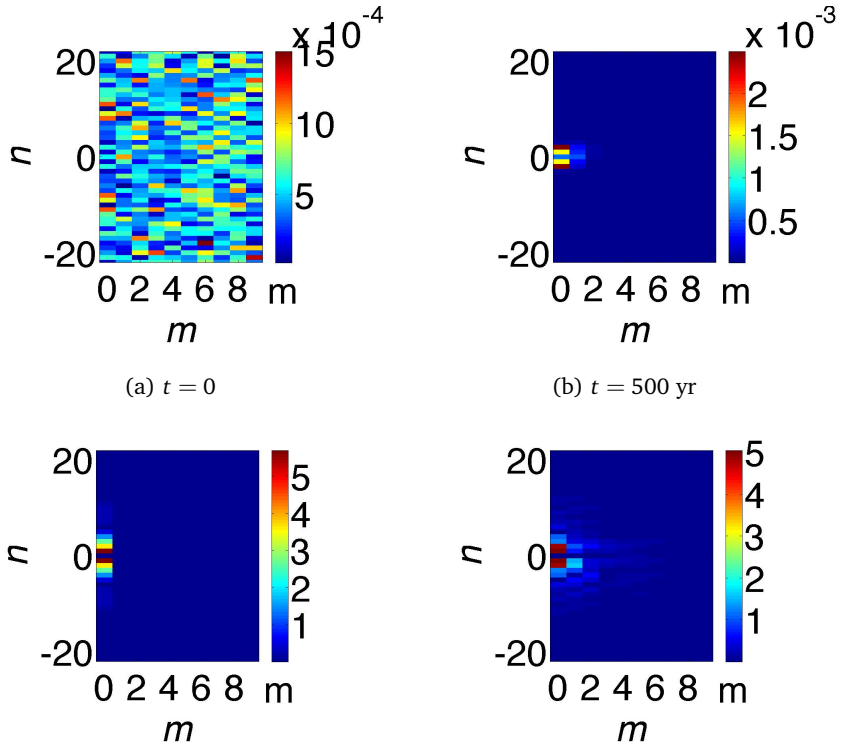

(a) $t = 0$ (b) $t = 500$ yr

(c) $t = 2600$ yr (d) $t = 3600$ yr

Figure 3.9: Amplitude $|a_{mn}|$ of bottom modes with index (m, n) (Eq. 3.8) at times: (a) $t = 0$, (b) $t = 500$ yr, (c) $t = 2600$ yr, (d) $t = 3600$ yr, corresponding to Fig. 3.3 (bottom). The image of $|a_{mn}|$ in the whole (m, n) space is symmetric with respect to $(0, 0)$, thus for better visualization only the part with positive m is shown. The index of the initially preferred bedform is $(0, 1)$.

One mechanism that causes the evolution of water waves from a 2D to a 3D pattern is related to the growth in amplitudes of waves that have wave vectors oblique to that of the original plane wave (Toffoli et al., 2013). Similarly, the development from straight crests to meandering crests for tidal sand ridges is the result of the presence of bottom modes with crests that are oblique to those of the preferred bedform. Based on the behavior of water waves, it is hypothesized that the occurrence of meandering ridges is linked to two variables. The first is the ratio of the wavenumber of the initially preferred bedform and the minimum wavenumber of bottom modes with crests normal to those of the preferred bedform, i.e., k_p / k_{x0}. The other is the relative ridge height h_{rel}, which is strongly coupled to the near-bed wave stirring coefficient U_w. In Fig. 3.10a, h_{rel} at time $t = \tau_g$ is plotted against the ratio between U_w and the velocity amplitude U_{M_2} of the M_2 tide for the cases of a rectilinear M_2

background tide, $U_c = 0$ and a 2D configuration. It is seen that the larger the value of U_w/U_{M_2}, the smaller the value of h_{rel}.

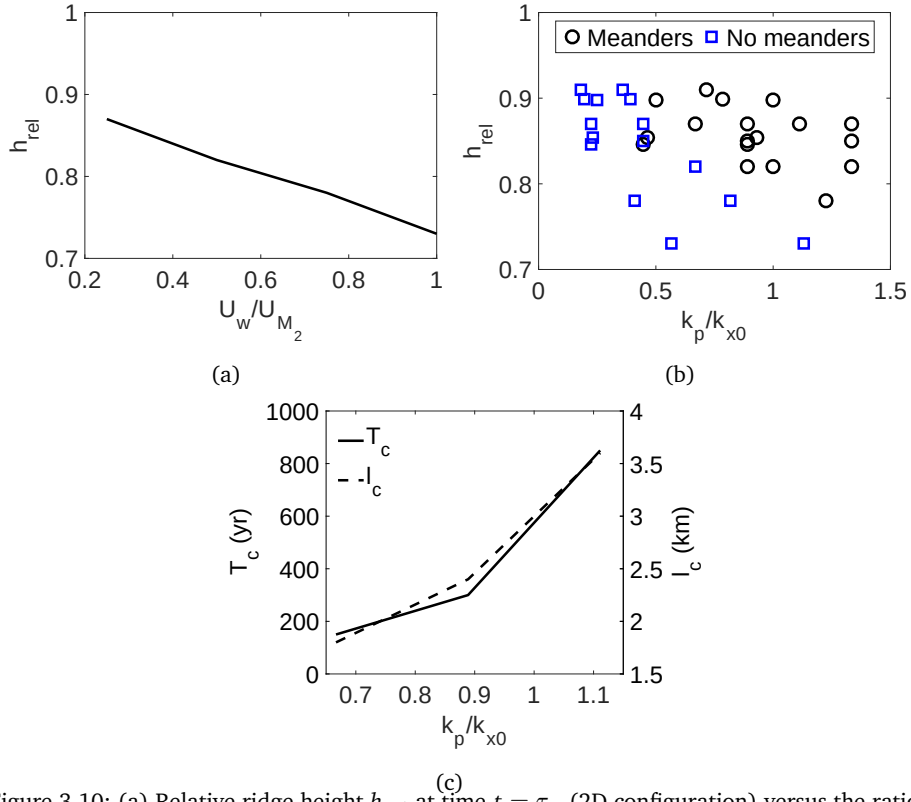

Figure 3.10: (a) Relative ridge height h_{rel} at time $t = \tau_g$ (2D configuration) versus the ratio between the near-bed wave stirring coefficient U_w and the velocity amplitude of the M_2 tide U_{M_2}. (b) Presence of meandering tidal sand ridges for different values of the wavenumber ratio k_p/k_{x0} and h_{rel} at time $t = \tau_g$, here $k_{x0} = 2\pi/L_x$ is the minimum wavenumber of the bottom modes with crests normal to those of the initially preferred bedform. (c) The period T_c (solid line) of the oscillation of the crests and the distance l_c that the crests shift in the y-direction (dashed line) versus k_p/k_{x0}. In (a) and (c), rectilinear M_2 background tidal currents were used and $U_c = 0$. For other parameters see Table 3.1.

Additional experiments were performed with different domain lengths L_x (recall that $k_{x0} = 2\pi/L_x$) and different values of U_w based on the experiments in Section 3.3. Fig. 3.10b shows the presence of meandering features for different values of the wavenumber ratio k_p/k_{x0} and h_{rel} at time $t = \tau_g$. In general, meanders appear if $h_{rel} \gtrsim 80\%$ and $k_p/k_{x0} \gtrsim 1$. In addition, Fig. 3.10c shows the period T_c of the oscillation of the crests and the distance l_c that the crests shift in the y-direction

versus the wavenumber ratio k_p/k_{x0} for the cases (with different L_x) of a rectilinear M_2 tidal current and $U_c = 0$. The values of T_c and l_c increase as k_p/k_{x0} increases.

Tidal sand ridges with meandering crests are indeed observed in the field, such as the Leman Bank and the Ower Bank of the Norfolk Banks area in the southern North Sea (Caston, 1972) and the Noordhinder Bank on the Belgian Continental Shelf (Smith, 1988). In particular, Caston (1972) suggested that, possibly due to an unequal sand transport rate along the originally straight crests of the ridges, a meandering ridge grows and breaks into three ridges. Smith (1988) on the other hand examined the stability of a kink in the Noordhinder Bank over a 135 yr period and did not find support for Caston's model. Instead, Smith (1988) proposed that it is more likely that eventually the kink would break, resulting in two ridges. In the present model, breaking of a ridge into two parts indeed happens, as shown in Figs. 3.3c-d. Additionally, merging of two ridges (not shown) with crests almost in the same direction occurs. Thus, alternate breaking and merging of ridges in the course of time takes place.

3.4.3 *Sensitivity of the results to numerical parameters*

The sensitivity of the results to numerical settings, i.e, the morphological acceleration factor β, the time step Δt, and the grid size Δx and Δy was examined. To this end, different values of numerics were used in the experiment with a rectilinear M_2 background tidal current, $U_c = 0$ and a 2D configuration, as considered in Section 3.3.1. In the reference case, $\Delta x = 400$ m, $\Delta y = 300$ m, $\Delta t = 8$ s and $\beta = 200$. For a smaller value of β, i.e., $\beta = 100$, the relative changes in the global growth time τ_g and h_{rms} at time $t = \tau_g$ of the bedforms are 0.1% and 0.02%, respectively. For a smaller time step, $\Delta t = 6$ s, the relative changes in τ_g and h_{rms} at time $t = \tau_g$ are 0.1% and 0.04%, respectively. Using a smaller grid size, $\Delta x = 200$ m and $\Delta y = 150$ m, comparing with the results in the reference case, τ_g is 0.2% larger, while h_{rms} at time $t = \tau_g$ is 2% smaller.

3.4.4 *Role of subharmonics of the preferred bedform in the dynamics of ridges*

So far, results have been presented for a domain length $L_y = \lambda_p$, such that in the direction normal to the crests of the initially preferred bedform, only the initially preferred bedform with a wavelength of λ_p and its superharmonics were included. Roos and Hulscher (2006) studied the effect of subharmonics on the finite-height sand ridges using a 1D configuration. They observed that in the presence of subharmonics of the initially preferred bedform, the average spacing between successive crests of ridges increased in time. This phenomenon, morphodynamic pattern coarsening, is

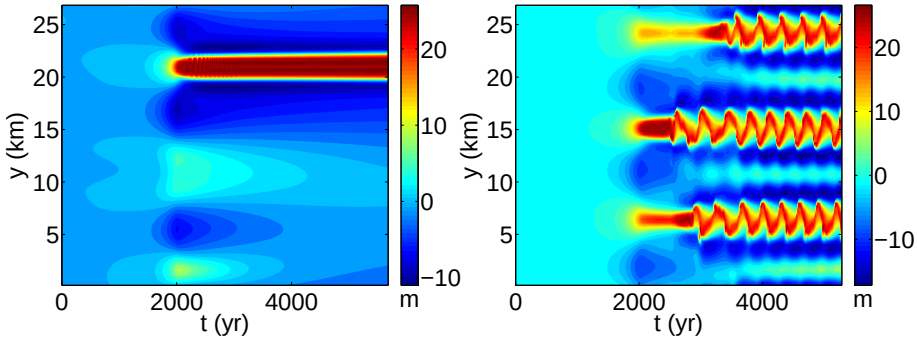

Figure 3.11: Time evolution of the bed level along a slice at $x = 3.2$ km in the experiments with subharmonics of the preferred bedform ($L_y = 3\lambda_p$), using a rectilinear M_2 background tidal current and $U_c = 0$. In (a) $L_x = 4$ km, no obvious meanders appear; in (b) $L_x = 8$ km, meanders appear. For other parameters see Table 3.1.

observed for other types of bedforms as well, such as sand bars in the nearshore zone (Garnier et al., 2006), shoreface-connected sand ridges (Calvete and de Swart, 2003; Nnafie et al., 2014b) and rippled scour depressions (Coco et al., 2007) on the inner continental shelf. In the present model, if subharmonics of the initially preferred bedform are considered, by using $L_y = I\lambda_p$ with I an integer larger than 1, coarsening of the ridges also occurs in the experiments in which no obvious meanders appear (Fig. 3.11a). Note that here the ridges do not migrate, and coarsening occurs as some ridges cease locally. If the bedforms migrate, merging of two parallel crests could happen due to different migration rates of the crests, as is found in the studies cited above (also see Appendix 3.C). In contrast, if meandering ridges appear, coarsening does not take place (Fig. 3.11b). Hence, it seems that introducing bottom modes with crests normal/oblique to that of the initially preferred bedform inhibits the coarsening of sand ridges, due to nonlinear interactions between those modes. This may contribute to the formation of multiple ridges aligning with each other in the field (apart from breaking of a ridge into two, as suggested by Smith, 1988), since in nature bottom modes with wave vectors in all horizontal directions exist. Note that other processes can slow down the coarsening, for instance, the presence of additional background tidal constituents, such as M_0 and M_4, besides M_2 (Roos and Hulscher, 2006) and sea level rise (Nnafie et al., 2014b).

Table 3.2: Observation at the Dutch banks and the Flemish banks and model input

	Parameter	Dutch Banks	Flemish Banks
Observation	Latitude Ω	52°40′ N	51°30′ N
	Wavelength (km)	5.7–9.8	4.5
	Orientation ϑ (°)	−25	−6
	Relative height h_{rel} (%)	26	61
	Asymmetry A	1.3	0.2
Model input	Mean water depth H (m)	28.9	28.7
	Residual flow velocity U_{M_0} (m s^{-1})	0.01	0
	Velocity amplitude of M_2, U_{M_2} (m s^{-1})	0.69	0.74
	Velocity amplitude of M_4, U_{M_4} (m s^{-1})	0.08	0.08
	Ellipticity of M_2, ϵ_{M_2}	−0.2	0.1
	Ellipticity of M_4, ϵ_{M_4}	−0.2	0.1
	Phase of M_2, ϕ_{M_2} (°)	0	0
	Phase of M_4, ϕ_{M_4} (°)	36.4	127.5
	Grain size d (mm)	0.25	0.45

3.4.5 *Comparison between modeled and observed tidal sand ridges*

Modeled tidal sand ridges are compared with two observed patches of ridges, viz. the Dutch Banks and the Flemish Banks in the southern North Sea. The observed characteristics of the ridges (after Roos et al., 2004) and the model input are listed in Table 3.2. The velocity amplitudes and phases of the tidal currents are based on the numerical work of van der Molen and de Swart (2001a). The values of the tidal ellipticity and the grain size are adopted from van Santen et al. (2011). The modeled initially preferred bedforms have wavelengths of 6.8 km and 5.6 km for input parameters that are representative for the Dutch and Flemish Banks, respectively, which qualitatively agree with the spacings between observed ridges. The crests of the modeled ridges are approximately 40° cyclonically rotated with respect to the principal current direction. The magnitudes of the modeled orientation angles are larger than those of the observed angles.

Fig. 3.12 and Fig. 3.13 show the observed and modeled ridge profiles for the Dutch Banks and the Flemish Banks, respectively. It is seen from Fig. 3.12 that the modeled ridge profiles between 6000 yr and 6500 yr (smaller than the global growth time, $\tau_g = 7300$ yr) for the Dutch Banks are similar to the observed ridge profiles. The corresponding relative height h_{rel} (23%–42%) from the modeled profiles is

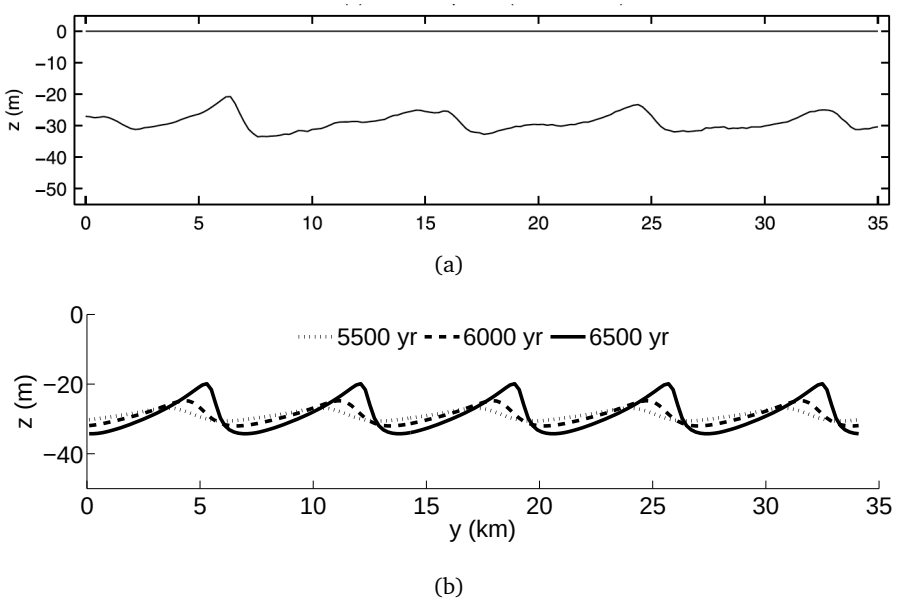

Figure 3.12: (a) Observed ridge profiles in the region of the Dutch Banks in the southern North Sea (after Roos et al., 2004). (b) Modeled ridge profiles at several times (input parameter values see Table 3.2). The bed level obtained in a domain with $L_y = 6.8$ km is used to cover a domain with L_y that is 5 times larger, and $L_x = 4$ km.

close to that retrieved from the field data, albeit the values of modeled and observed asymmetry A (defined in Eq. 3.10) differ. The same applies to the Flemish Banks (the modeled $\tau_g = 6600$ yr, and from 6000 yr to 6500 yr h_{rel} increases from 60% to 79%), while the location of the steeper side of the ridge with respect to the crests (indicated by the sign of A) is different from that in the field (Fig. 3.13). Hence, it is likely that those ridges are still growing.

There are several aspects that might explain the difference in the spacings of the modeled and observed ridges in Figs. 3.12 and 3.13. First, note that the observed spacings in Table 3.2 represent the dominant values obtained from Fourier analysis of the seabed topography in the regions of the Dutch Banks and the Flemish Banks. The spacing of the ridges itself in the field could vary even within a small domain as seen from Fig. 3.13a. Second, the background tidal forcing in the model consists of only one primary (M_2) constituent, its first overtide and the residual current, whereas in nature multiple tidal constituents are present. Third, in the model the domain size was fixed according to the spacing of the initially preferred bedform based on the present-day conditions, while in nature the spacing of the ridges could change in time due to changes in the sea level, tide and wave conditions. Some of these aspects will be investigated in the next chapter.

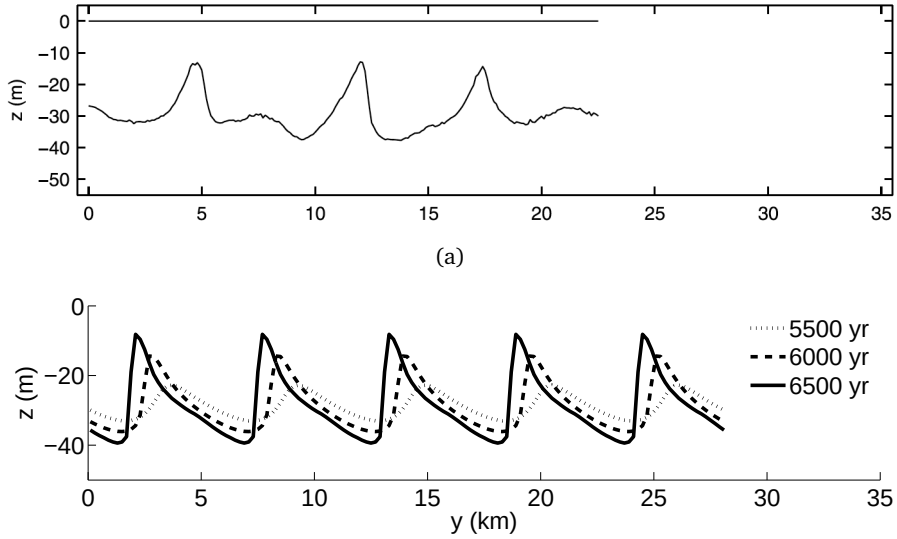

Figure 3.13: As in Fig. 3.12 but for the Flemish Banks. In (b), the bed level obtained in a domain with $L_y = 5.6$ km is used to cover a domain with L_y that is 5 times larger, and $L_x = 4$ km.

Different location of the steeper ridge side with respect to the crests between the modeled and observed ridges (Flemish Banks setting) could be due to that the phase difference $\Delta\phi$ between the tides M_2 and M_4 used in the model is different from that in the field. In Uehara et al. (2006), it was shown that the spatial pattern of sand transport in the area of the Flemish Banks is quite complicated according to the peak bed shear stress vectors in that area, i.e., the direction of the peak bed shear stress vectors varies by 180°. Results of further experiments using different values of $\Delta\phi$ show that the magnitude and sign of A vary with $\Delta\phi$. If the tidal current consists of only M_2 and M_4, increasing/decreasing the phase difference $\Delta\phi$ between M_2 and M_4 by π changes the sign of A. This means that the new ridge profiles are like those shown in Fig. 3.13b, except that the steeper and gentler sides with respect to the crests are reversed.

3.4.6 *Limitations of the model*

Several assumptions have been made in the present model. First, the vertical flow structure is neglected by employing the depth-averaged shallow water equations, so the model is unable to simulate sand waves (Hulscher, 1996). The difference between modeled and observed orientations of the bedforms could also be due to this assumption, since sand transport is determined by the near-bed currents, the direc-

tion of which may differ from that of depth averaged currents (e.g., Shapiro et al., 2004). Second, the mean sea level is assumed to be constant, while it has changed significantly over the last thousands of years. For example, it has been shown that the sea level for the continental shelves of Belgium and the Netherlands at 8 ka BP (thousands years before present) was about 15 m lower than the present sea level (Beets and van der Spek, 2000). Third, the tide and wave conditions have also changed during the last few thousands of years (Uehara et al., 2006; Neill et al., 2009) , but such changes are not taken into account here. Note that no phase difference of the background tidal forcing within the study domain is considered as it is assumed that the domain size is much smaller than the wavelength of principal tidal waves, and the way of including the wind wave stirring is parametric. Fourth, only bed load transport of sand is considered, while suspended load could also play a role in the long-term evolution of these bedforms if the current is strong and the grain size is small (Besio et al., 2006). Additionally, uniform grain size is assumed, while in nature multiple sand fractions are present (see e.g. Gao et al., 1994). Thus sorting processes (Walgreen et al., 2004) resulting in variation of mean grain size over the ridges are not accounted for. Last, the domain size is fixed and the principal current direction is prescribed such that the crests of the initially preferred bedform align with the x-axis. Natural selection of the wavelength and orientation of the bedforms could be possible if a 2D domain is used and its size is large enough. However, at the present stage the computational efficiency of the model hinders such kind of simulations.

3.5 CONCLUSIONS

Using a nonlinear morphodynamic model, the dynamics of finite-height tidal sand ridges in the shelf seas have been studied. The focus has been on the effect of considering topographies that vary in either one or two horizontal dimensions, tidal ellipticity and critical shear stress for sand erosion on shape and growth time of sand ridges.

For the range of parameter values that have been considered in this chapter, different results have been found between the cases using 1D and 2D configurations. Compared to the 1D case, in the 2D case it takes longer time for the ridges to reach a similar value of root mean square height h_{rms}. In the 1D case, the end state is a static equilibrium state, i.e., h_{rms} remains constant. In contrast, in the 2D case, the ridges reach a dynamic equilibrium state, if the minimum wavenumber of the bottom modes with crests normal to those of the preferred bedform is in the order or less than the wavenumber of the preferred bedform and the relative ridge height right after the global growth time is above 80%. This state is characterized by ridges with meandering crests that oscillate in time.

If elliptical tides and the critical shear stress for sand erosion are considered, tidal sand ridges with meandering crests are still observed in the 2D case. Regarding

elliptical tides, noticeable changes in the shape of ridges are observed. The minimum of the relative ridge height after the global growth time varies from 85% at $\epsilon = -0.2$ to 48% at $\epsilon = 0.4$, while the maximum of the relative ridge height is around 93% for all the values of ϵ considered in this chapter. The global growth time of the ridges varies non-monotonically with ellipticity. In contrast, if the critical bed shear stress is considered, the ridge shape hardly changes, and the global growth time increases compared to that in the case neglecting the critical bed shear stress. The modeled ridge profiles in the period 6000–6500 yr (smaller than the global growth time) are similar to the observed ridge profiles for the Dutch Banks and the Flemish Banks in the southern North Sea. This result suggests that the ridges at those locations might still be growing.

3.A VERIFICATION OF THE NUMERICAL MODEL (1D CONFIGURATION)

Here, it is verified whether the model is able to simulate finite-height tidal sand ridges that were obtained in an earlier study by Roos et al. (2004) (abbreviated as RHK04). As in RHK04, rectilinear tides and no critical bed shear stress for sand erosion are used, a 1D configuration is assumed, and the same formulations for the bottom shear stress and bed load are employed. A linearized formulation of $\vec{\tau}_b$ is used, which reads

$$\vec{\tau}_b = \rho r \vec{u}, \tag{3.A1}$$

where r is the linear friction coefficient. For sand transport, the bed load formulation used is

$$\vec{q} = \alpha_e u_e^2 \left(\vec{u} - \Lambda U \nabla h\right), \tag{3.A2}$$

where U is a constant velocity. The same parameter values as those in RHK04 are taken: $r = 2.5 \times 10^{-3}$ m s^{-1}, $\alpha_e = 4 \times 10^{-5}$ m^{-1} s^2, and $U = 1$ m s^{-1}. Suspended load is not considered. Values for the other parameters are shown in Table 3.1.

In the case that the background tidal forcing consists of more than one tidal constituent, following Vis-Star et al. (2008), the global migration rate of the bedforms is introduced. Recall that the crests of the initially preferred bedform are parallel to the x-axis. As most spatial variation of the bedforms is expected in the y-direction, only the migration rate in the y-direction is presented, i.e.

$$c_y = -\frac{1}{\overline{(\partial h/\partial y)^2}} \overline{\left(\frac{\partial h}{\partial y}\frac{\partial h}{\partial t}\right)}. \tag{3.A3}$$

3.A.1 *Comparison with results in RHK04*

Table 3.A1 shows the comparison of the characteristics of the initially preferred bedform and the corresponding equilibrium ridges obtained from the present model with those in RHK04. Exp. 0 is the reference case for Exps. 1 to 4, in which the semidiurnal tide M_2 is used, the Coriolis force is neglected and $U_w = 0.25$ m s^{-1}. Compared to Exp. 0, Exp. 1 includes the Coriolis force, Exp. 2 uses a larger near-bed wave stirring coefficient, i.e., U_w =0.5 m s^{-1}, Exp. 3 includes the residual flow M_0, and Exp. 4 includes the first overtide of M_2. The experiments for the finite-height ridges use a domain length $L_y = \lambda_p$, where λ_p is the wavelength of the initially preferred bedform. The wavelength λ_p and the orientation ϑ_p of the initially preferred bedform from the present model are close to those in RHK04.

From Table 3.A1, it is seen that the characteristics of the equilibrium ridges calculated with the present model agree well with those obtained by RHK04. Compared

Table 3.A1: Comparison of the characteristics of the initially preferred bedform and the corresponding equilibrium ridges obtained from the present model with those in RHK04

No.	Description	λ_p (km)		ϑ_p (°)		$\lvert z_{cr}\rvert$ (m)		$\lvert z_{tr}\rvert$ (m)		h_{rel} (%)		A		c_y (m yr^{-1})	
		R	P	R	P	R	P	R	P	R	P	R	P	R	P
0	Reference	8.4	8.6	−28	−29	5.0	4.7	37.2	37.4	87	87	0	0	0	0
1	With Coriolis	8.8	9.0	−36	−36	3.5	3.4	35.8	36.0	90	90	0	0	0	0
2	$U_w = 0.5$ m s^{-1}	8.5	9.0	−28	−30	7.1	7.0	39.7	40.0	82	83	0	0	0	0
3	%10 M_0	8.4	8.8	−29	−30	15.9	15.7	46.8	47.6	66	67	1.6	1.7	4.4	4.7
4	%10 M_4	8.1	8.4	−30	−30	11.6	11.6	45.0	45.2	74	74	1.5	1.6	3.2	3.4

Letters R and P mean results from RHK04 and from the present model, respectively. If multiple tidal constituents are used (Exps. 3 and 4), the sum of the current amplitudes is kept as 1 m s^{-1}, and the phase difference is 0. For instance, in Exp. 4, $U_{M_2} = 0.9$ m s^{-1} and $U_{M_4} = 0.1$ m s^{-1}.

to RHK04, the numerical model yields slightly smaller distances from the reference sea surface to the crest level $|z_{cr}|$, and slightly larger distances from the reference sea surface to the trough level $|z_{tr}|$. The differences in the relative height of the equilibrium ridge h_{rel} between the present model and that of RHK04 are marginal. Furthermore, the asymmetry A of the equilibrium ridge and the migration rate c_y of the ridges in the experiments with more than one tidal constituent (Exps. 3 and 4) are slightly larger than those in RHK04. The reasons for the differences in the characteristics of the initially preferred bedform and the equilibrium ridges are discussed below.

3.A.2 *Differences between the present results and those in RHK04*

There are two main reasons for the differences between the present results and those in RHK04. First, a rigid-lid approximation was used in the latter study, while the surface elevation due to the bedforms in the present model is time and space dependent. Second, the solutions (in the form of Fourier series) of the bed level and the topography-induced velocity in RHK04 were truncated in both the frequency domain and the topographic wavenumber domain. In the frequency domain, up to the second overtide of the basic constituent M_2 was considered, and in the wavenumber domain the largest topographic wavenumber resolved was typically 16 times of that of the initially preferred bedform. In contrast, in the present model, a large number of higher harmonics generated by tide-topography interactions are included automatically (largest harmonic is only limited by the time step), and the number of the Fourier components in space is determined by the number of grid points. For instance, the number of grid points in Exp. 0 is 43, thus the number of Fourier components in space is 43, and the largest topographic wavenumber is 21 times of that of the initially preferred bedform.

3.B ELLIPTICAL TIDE AND CRITICAL VELOCITY FOR SAND EROSION: 1D CONFIGURATION

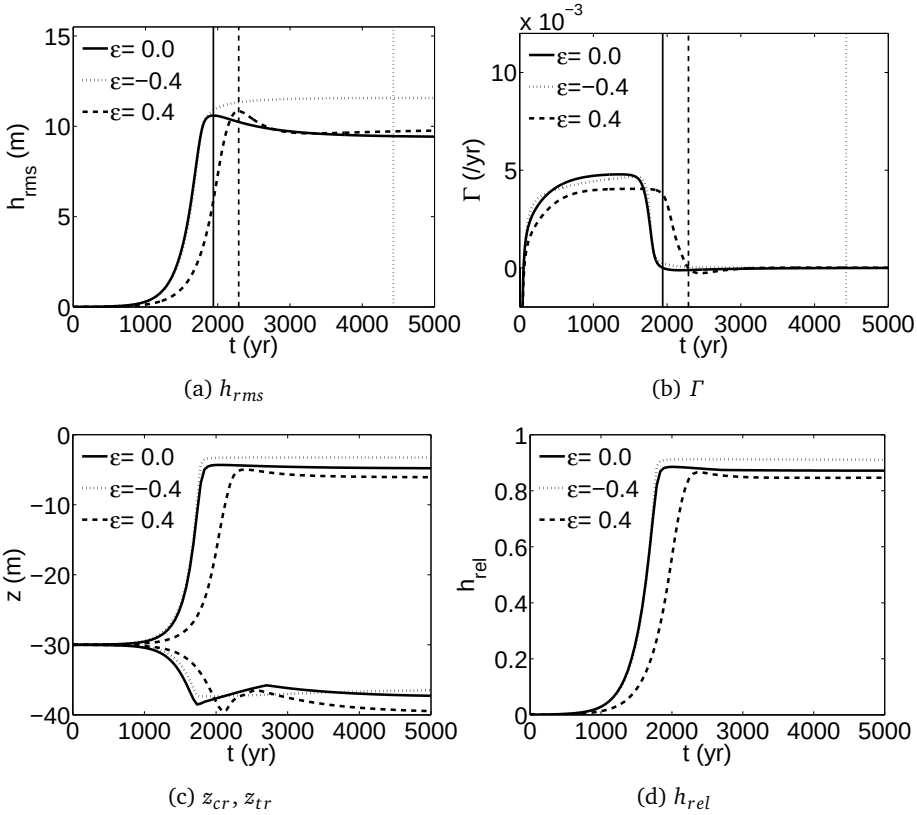

(a) h_{rms} (b) Γ

(c) z_{cr}, z_{tr} (d) h_{rel}

Figure 3.B1: Time evolution of (a) root mean square height h_{rms}, (b) global growth rate Γ, (c) crest level z_{cr} and trough level z_{tr}, and (d) relative ridge height h_{rel} of the bedforms, using an M_2 background tidal current with different values of ellipticity ϵ, $U_c = 0$ and a 1D configuration. The vertical lines mark the global growth time τ_g of the bedforms.

Fig. 3.B1 shows time series of the root mean square height h_{rms}, the global growth rate Γ, the crest level z_{cr} and trough level z_{tr}, and the relative ridge height h_{rel} for the experiments with a 1D configuration that consider elliptical tides. Only some of the results ($\epsilon = -0.4, 0, 0.4$) are shown. For all the experiments considered here, four different stages are distinguished. First, h_{rms} (Fig. 3.B1a) is small and hardly changes, while the global growth rate of the bedforms (Fig. 3.B1b) increases from negative to positive. This period corresponds to the period of the selection of

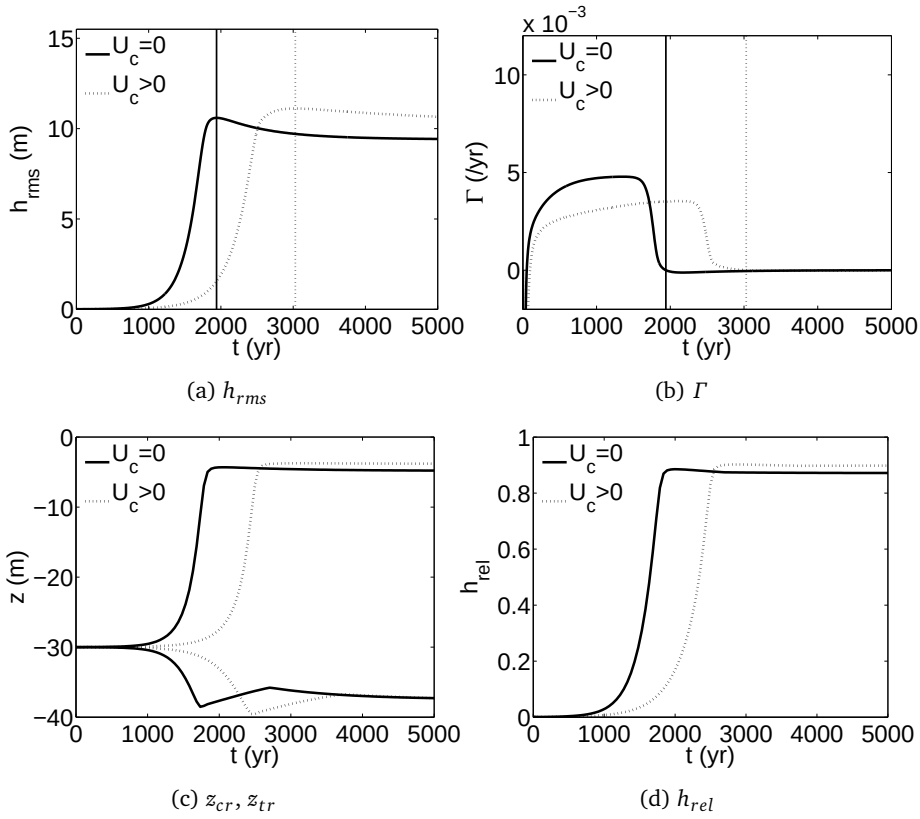

(a) h_{rms} (b) Γ

(c) z_{cr}, z_{tr} (d) h_{rel}

Figure 3.B2: As Fig. 3.B1 but for the case of $U_c > 0$ and a rectilinear M_2 background tide.

bottom modes, viz. only the amplitude of modes with positive growth rate will grow. Next, the global growth rate of the bedforms becomes nearly constant, and the root mean square height h_{rms} of the bedforms grows exponentially in time (Fig. 3.B1a). Hereafter, the global growth rate Γ decreases to 0 in a short period. In the final stage, Γ remains 0, and h_{rms} reaches a large value and does not change, viz. a static equilibrium state is obtained. The dependence of the global growth time τ_g on the tidal ellipticity appears to be non-monotonic, with the smallest $\tau_g \sim 1900$ yr found at $\epsilon = -0.2$. In the static equilibrium state, the distance from the reference sea level to the crest $|z_{cr}|$ increases as ϵ increases from -0.4 to 0.4, and the distance from the reference sea level to the trough $|z_{tr}|$ increases as ϵ increases from -0.2 to 0.4 (Fig. 3.B1c). The resulting h_{rel} (Fig. 3.B1d) decreases from 91% ($\epsilon = -0.4$) to 85% ($\epsilon = 0.4$).

Fig. 3.B2 shows the time evolution of h_{rms}, Γ, z_{cr}, z_{tr} and h_{rel} for the experiments considering the critical velocity U_c for sand erosion. Similar to the experiments

using elliptical tides, ridges reach a static equilibrium state. The most significant change in the characteristics of the bedforms when $U_c > 0$ (for undisturbed water depth $H = 30$ m, $U_c = 0.48$ m s^{-1}) is in the global growth time τ_g. If $U_c > 0$ is considered, an increase of 1100 yr in τ_g is observed, and the ridge profile is slightly spikier ($h_{rel} = 90\%$) than that in the case that $U_c = 0$ ($h_{rel} = 87\%$).

3.C ASYMMETRIC BACKGROUND TIDAL CURRENTS: 2D CONFIGURATION

The effect of considering background tidal currents with two constituents M_2 and M_4 in a 2D configuration on the characteristics of finite-height ridges is explored. The setup of the experiments is the same as that of Exp. 4 in Table 3.A1 except that the Coriolis force is considered and a 2D configuration is used. The velocity amplitudes of the constituents are $U_{M_2} = 0.9$ m s^{-1} and $U_{M_4} = 0.1$ m s^{-1}, and the phase difference between M_2 and M_4 is 0, so the background tidal current is rectilinear and asymmetric. Fig. 3.C1 shows the time evolution of the bed level of a slice along the y-direction (at $x = 3.2$ km) for the cases of asymmetric tidal currents with and without subharmonics of the initially preferred bedform. If subharmonics of the initially preferred bedforms are absent (Fig. 3.C1a), in the end the shape of the sand ridges is fixed, with $h_{rel} = 76\%$ and $A = -2.3$, and the ridges migrate in the negative y-direction with $c_y = 5$ m yr^{-1}. In the presence of subharmonics of the initially preferred bedforms (Fig. 3.C1b), coarsening of the ridges is observed. This

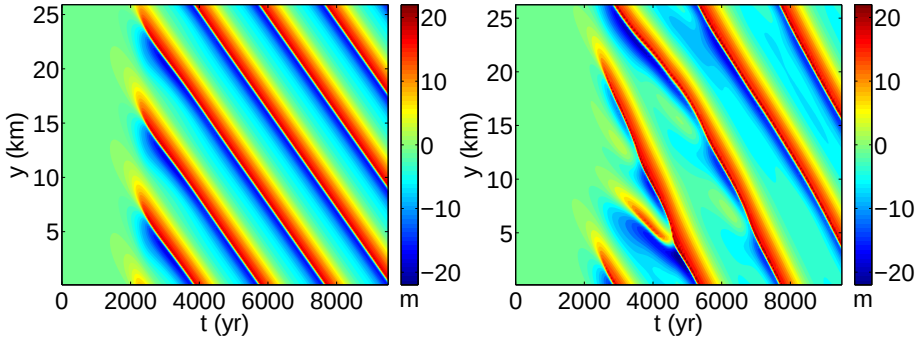

(a) $L_y = \lambda_p$ (b) $L_y = 3\lambda_p$

Figure 3.C1: Time evolution of the bed level of a slice along the y-direction (at $x = 3.2$ km) in the cases of using a rectilinear $M_2 + M_4$ background tidal current and (a) $L_y = \lambda_p$ and (b) $L_y = 3\lambda_p$. In (a) the bed level obtained in a domain with $L_y = 8.6$ km is used to cover a domain with L_y that is 3 times larger. In both cases, $L_x = 4$ km.

process is slower than that in the case in which only an M_2 tide is considered (see Section 3.4.4, within 5000 yr, only one ridge remains in a domain size $L_y = 3\lambda_P$).

Considering the fact that so far field data have not clearly revealed migration of tidal sand ridges, the value of c_y obtained here is large. Further experiments show that changing the velocity amplitude ratio or the phase difference between M_2 and M_4 can change the value of c_y significantly. Furthermore, results of experiments using different values of U_{M_4}/U_{max} ($U_{max} = 1$ m s^{-1}) with no phase difference between M_2 and M_4 and no subharmonics show that h_{rel} decreases as U_{M_4}/U_{max} increases within $[0, 0.5]$. As in the cases using only M_2, dynamic equilibrium is also observed if $h_{rel} > 0.8$ and bottom modes with crests normal to those of the preferred bedform have wavenumbers in the order of that of the preferred bedform.

4

EFFECT OF SEA LEVEL RISE AND TIDAL CURRENT VARIATION ON THE LONG-TERM EVOLUTION OF OFFSHORE TIDAL SAND RIDGES

4.1 INTRODUCTION

In Chapter 3, the long-term evolution of offshore tidal sand ridges subject to constant sea level and tidal conditions was modeled and the modeled ridges were shown to be always active. However, as was mentioned in Chapter 1, both the sea level and the characteristics of the tidal current change on the time scales of tidal sand ridges (Beets and van der Spek, 2000; Fleming et al., 1998; van der Molen and de Swart, 2001a; Uehara et al., 2006). The role of changing sea level and tidal conditions during the long-term evolution of tidal sand ridges has not been investigated yet. In particular, how active sand ridges react to the changing sea level and tidal conditions and why these bedforms become quasi-active/moribund are not fully understood.

Based on the considerations above, the aims of the research in this chapter are twofold. First, to quantify the effect of SLR and variation in the strength and principal direction of the tidal current on the characteristics (growth time and height) of active tidal sand ridges. Second, to explore the role of SLR and tidal current variation in the occurrence of quasi-active/moribund ridges. Note that the time scale considered is of order 10 ka, which represents that for the ridges in the southern North Sea and the Celtic Sea. Changes in the wave height and wave period are not investigated here, and unlimited availability of sand in the bed is assumed.

This chapter has been submitted as:
Yuan, B., de Swart, H. E., 2017. Effect of sea level rise and tidal current variation on the long-term evolution of offshore tidal sand ridges.

To fulfill these aims, an extended version of the model in Chapter 3 was used. The extension concerns the consideration of SLR and tidal current variation. The approach resembles that of Nnafie et al. (2014a), who studied the influence of SLR on dynamics of shoreface-connected sand ridges, which are large-scale bedforms observed on the shoreface. In that study, it was demonstrated that SLR is a key factor for the dynamics of those ridges.

In Section 4.2, first the morphodynamic model is briefly described, next the quantities for the characteristics of finite-height ridges and experiments design are introduced. Two specific default settings are considered, which are representative for the Dutch Banks in the southern North Sea and for ridges in the Celtic Sea. Results are shown in Section 4.3, followed by discussion in Section 4.4 and conclusions in Section 4.5.

4.2 MATERIAL AND METHODS

Based on the model in Chapter 3, changes in the sea level and tidal conditions are included in this chapter. A different formulation for the amplitude of the near-bed wave-orbital velocity u_w from that in Chapter 3 (Eq. 3.7) is used (see Eq. 4.A6 in Appendix 4.A). In a sketch (Fig. 4.1), the top view and side view of the model geometry are presented. In the top view, the tidal ellipse of the background current $\vec{u}_0$ is shown. In the side view, the time-varying sea level z_s, the undisturbed water depth H_0 and the crest and trough levels h_{cr} and h_{tr} with respect to the reference bottom level z_b are shown.

SLR is included in the model by considering changes in the mean sea level z_s with a rate of R but no change in the mean sea bottom level z_b (see Fig. 4.1), i.e.,

$$\frac{dz_b}{dt} = 0, \qquad \frac{dz_s}{dt} = \frac{dH}{dt} = R. \tag{4.1}$$

This means that the change in the mean water depth $H = z_s - z_b$ due to isostatic rebound (see e.g. Lambeck, 1995) is not taken into account, but it can be mimicked by adjustment of the value of R in the model. The rate R of SLR is assumed to be a piecewise linear function of time. Similarly, changes in the tidal current characteristics are considered by assuming the velocity amplitude and the principal direction of $\vec{u}_0$ to be piecewise linear in time. By choosing the sea level and tidal conditions at several time spots from reconstructed sea level curves (e.g. Behre, 2007) and tidal conditions (e.g. Uehara et al., 2006) and applying the above assumptions, the general characteristics of the sea level and the tidal current are captured.

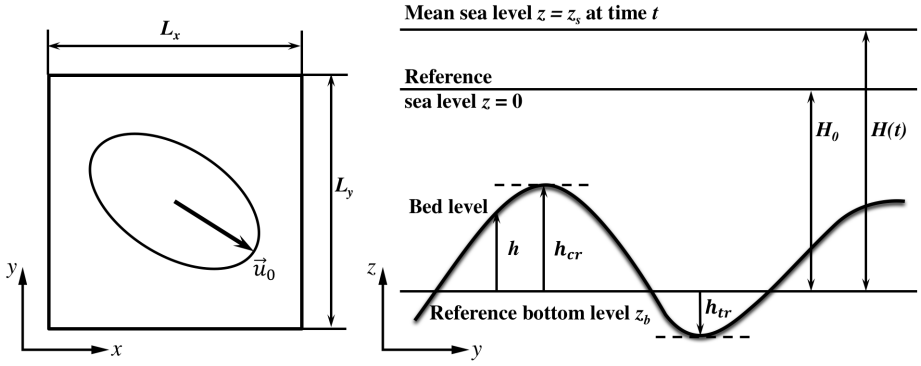

Figure 4.1: Top view (left) and side view (right) of the model geometry. In the top view, the tidal ellipse of the background current $\vec{u}_0$ is shown. In the side view, the bed level h with respect to the reference bottom level z_b, the reference sea level $z = 0$ (initial mean sea level), the time-varying mean sea level $z = z_s$, the initially undisturbed water depth H_0, and the crest and trough levels h_{cr} and h_{tr} with respect to z_b are also shown.

4.2.1 *Quantities to describe characteristics of finite-height bedforms*

Following Garnier et al. (2006), a global growth rate Γ of the bedforms is employed to describe the growth or decay of the amplitude of the bedforms, which reads

$$\Gamma = \frac{1}{(h_{rms}^2)} \frac{\partial}{\partial t} \left(\frac{1}{2} h_{rms}^2 \right). \tag{4.2}$$

Here, $h_{rms} = (\overline{h^2})^{\frac{1}{2}}$ is the root mean square height of the bedforms that indicates the variance of the bed level, with the overbar denoting spatial averaging.

Linear stability theory (Huthnance, 1982a) shows that initially the amplitudes of the bottom modes (Fourier modes of bottom perturbations) evolve exponentially in time. After the exponential growth stage, for a constant sea level and a constant tide and wave climate, the ridges reach a static equilibrium (Roos et al., 2004) or a dynamic equilibrium (see Chapter 3), i.e., Γ becomes 0 or oscillates around 0 in time. Based on these studies, for a changing sea level and tidal condition, a global growth time τ_g is defined as the time when Γ becomes no more than 1% of the maximum value of Γ after the exponential growth stage.

Furthermore, to characterize the height of the ridges, following Roos et al. (2004), the relative ridge height is used, which is the percentage of the maximum water depth (neglecting surface elevation) that the ridge height makes up in a cross-sectional (normal to crests) ridge profile:

$$h_{rel} = \frac{h_{cr} - h_{tr}}{H - h_{tr}}. \tag{4.3}$$

Here, $(h_{cr} - h_{tr})$ is the vertical distance between the crest and trough levels from the cross-sectional ridge profile, which represents the height of the ridge, with h_{tr} and h_{cr} being the trough and crest levels with respect to the fixed reference bottom level z_b (see Fig. 4.1).

4.2.2 *Design of the experiments*

To achieve the aims of this study, tidal sand ridges in the southern North Sea, specifically the Dutch Banks, are selected as a prototype of active sand ridges, while those in the Celtic Sea (Celtic Banks) are chosen to represent moribund ridges. The default parameter values are given in Table 4.1. Full information about tidal constituents during the Holocene or earlier is lacking, hence only the semidiurnal M_2 tide is considered. Table 4.2 lists the experiments with different rates R of SLR, initially undisturbed water depth H_0, velocity amplitude U and change $\Delta\varphi$ in the principal direction of the background tidal current $\vec{u}_0$ for the Dutch Banks and the Celtic Banks. Positive $\Delta\varphi$ means that the major axis of tidal ellipses rotates counterclockwise.

Table 4.1: Default parameter values in the experiments

Parameter	Value	Description
Φ	53° N/49° N	Latitude
ω_{M_2}	1.4×10^{-4} rad s^{-1}	Angular frequency of M_2 tide
g	9.81 m s^{-2}	Gravitational acceleration
Λ	2.0	Bed slope coefficient
p	0.4	Bed porosity
ν	1.4×10^{-6} m^2 s^{-1}	Kinematic viscosity of water
s	2.6	Density ratio between sand and water
d	0.25/0.4 mm	Grain size
μ_d	0.6	Dynamic friction coefficient
Δx	300 m	Grid size in the x-direction
Δy	300 m	Grid size in the y-direction
Δt	6–12 s	Time step
β	50–450	Morphological acceleration factor

If two values (e.g. 0.25/0.4 mm) are listed, the first one refers to the Dutch Banks and the second one refers to the Celtic Banks.

Table 4.2: Values of rate R of SLR, initially undisturbed mean water depth H_0, velocity amplitude U and change $\Delta\varphi$ in the principal direction of the background tidal current for the Dutch banks (Exps. 1–4) and the Celtic Banks (Exps. 5–9)

Exp. no.	R (mm/yr)	H_0 (m)	U (m/s)	$\Delta\varphi$ (°)
1	0, 0.5, 1.0, 1.5, 1.875, 2.5, 3.0	30	0.75	0
2	0.5, 1.0, 1.5, 1.875, 2.5, 3.0	10, 15, 20	0.75	0
3	1.875	15	0 ka: 0.50 2–∞ ka: 0.75 0.5	0
4	1.875	15	0 ka: 0.50 2–∞ ka: 0.75	0–2 ka: 15 2–∞ ka: 0
5	0–3 ka: 5.0 3–12 ka: 10.0 12–14 ka: 7.0 14–∞ ka: 1.0	15	0 ka: 1.25 8–10 ka: 0.75 12–∞ ka: 0.35	0–8 ka: 8 8–10 ka: 0 10–12 ka: 2 12–∞ ka: 0
6	1, 6.25	As Exp. 5	As Exp. 5	As Exp. 5
7	As Exp. 5	10, 20	As Exp. 5	As Exp. 5
8	As Exp. 5	As Exp. 5	0.67	As Exp. 5
9	As Exp. 5	As Exp. 5	As Exp. 5	0

If no time is specified, the values of the parameters are constant in time, 'ka' represents 1000 years, 0 ka corresponds to the starting time of simulation, and '–∞' means to the end of simulation.

For the Dutch Banks, in Exp. 1, different rates of SLR are considered and the background tidal current $\vec{u}_0$ is kept fixed. The initially undisturbed water depth H_0 and the velocity amplitude U of $\vec{u}_0$ are based on the present-day values. Constant rates R are used, which are chosen such that their values are below the maximum R based on the sea level curve from 8 ka BP of the southern North Sea (Behre, 2007), i.e., 8–7 ka BP: $\sim$ 5 mm/yr, 7–5 ka BP: $\sim$ 2.5 mm/yr, 5 ka BP to the present: $\sim$ 1 mm/yr. Note that a constant rate of SLR of 1.875 mm/yr corresponds to an increase of 15 m in the water depth in a period of 8 ka, which mimics the overall change of the sea level during the last 8 ka in the southern North Sea.

In Exp. 2, different initially undisturbed water depths H_0 are considered together with constant rates of SLR. The depth $H_0 = 15$ m corresponds to the mean water depth at 8 ka BP in the southern North Sea. As sand ridges may start growing for different H_0 and the water depth is not constant in the entire southern North Sea, different values of H_0 (10, 20 m) from 15 m are considered, and the choice of H_0 is further discussed later in this section. Furthermore, in Exp. 3 changes in the background tidal current amplitude U are included, which are derived from the model

results in Uehara et al. (2006). For comparison, a constant $U = 0.5$ m/s (representing the tidal condition at 8 ka BP in the southern North Sea) in time is also used. In Exp. 4 changes $\Delta\varphi$ in the principal current direction are considered, the values of which are obtained from modeled tidal ellipses from 7.5 ka BP to the present in the southern North Sea (van der Molen and de Swart, 2001a). In all the experiments, the ellipticity ϵ of the tidal ellipse (ratio between the minor and major axes of the tidal ellipse) is assumed to be constant in time ($\epsilon = -0.2$), which is justified by the comparison between the modeled tidal ellipses at 7.5 ka BP and at present in the southern North Sea. A negative value of ϵ means that the current velocity vector rotates in a clockwise sense.

From Neill et al. (2009), the representative wave height and wave period are chosen to be $H_w = 2.5$ m and $T_w = 6$ s. Fig. 4.2 shows the calculated amplitude U_e of the effective velocity, the critical velocity for sand erosion U_c and the amplitude of near-bed wave orbital velocity u_w as a function of mean water depth H, where $U = 0.5$ m/s and other parameter values are representative for the case of the Dutch Banks. For the considered time range and rates of SLR, the mean water depth is less than 100 m, in which U_e is always larger than U_c. Note that for water depths close to 0, as the depth decreases the wave height and wave period decrease (Young and Verhagen, 1996), and so does the amplitude of the tidal current. If that is accounted for, the solid curve for U_e in Fig. 4.2 will go down as H (close to 0) decreases and it will intersect the dashed curve for U_c. The intersection point gives a critical minimum depth H_{0c} below which no tidal sand ridges will form. Here, the interest is in the cases that initially the sandy bed is active, thus the chosen initial water depth H_0 is always larger than H_{0c}. It is shown in Appendix 4.A that by assuming a constant

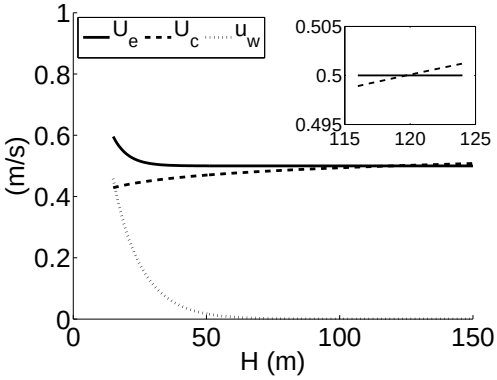

Figure 4.2: The amplitude U_e of the effective velocity (solid line), the critical velocity for sand erosion U_c (dashed line) and the amplitude of near-bed wave orbital velocity u_w (dotted line) as a function of mean water depth H for the settings of the Dutch Banks with $U = 0.5$ m/s. Insert: zoom in for H between 115 m and 125 m.

pressure gradient force $\vec{F}_p$ in time for small water depths, for $H = 15$ m, $U = 0.5$ m/s, $\epsilon = -0.2$ (Exp. 4) and the wind conditions in the considered regions, $H_{0c} \sim 10$ m. Furthermore, to a good approximation, H_w and T_w are kept constant for $H \geq H_{0c}$.

In the experiments for the Dutch Banks, the domain length and the initial principal direction of $\vec{u}_0$ are chosen based on the initially preferred bedform under the present-day conditions obtained from linear stability analysis. The initially preferred bedform under the present-day conditions has a spacing λ_p of 7.5 km, which is in the range of the present-day values (5.7–9.8 km from Roos et al., 2004), and its crests are 37° cyclonically oriented with respect to the principal current direction. Accordingly, the domain length in the y-direction L_y is chosen to be 7.5 km, and initially the major axis of $\vec{u}_0$ is 37° anticyclonically rotated with respect to the x-axis. In the default setting, the domain length L_x is chosen equal to L_y. The sensitivity of the results to L_x and L_y is discussed in Section 4.4.3.

Regarding the Celtic Banks, the consensus is that their formation started at the Last Glacial Maximum lowstand, i.e, roughly at the time 20 ka BP (Scourse et al., 2009, and references therein). Several experiments using the conditions that mimic those for the Celtic Banks are conducted to investigate the role of SLR and tidal current variation on the occurrence of quasi-active/moribund ridges.

In Exp. 5 (see Table 4.2), both SLR and changes in the strength and principal direction of the tidal current are considered. The rate R of SLR in the Celtic Sea is adopted from Fleming et al. (1998) and Shennan et al. (2006), and in total the water depth increases by 125 m in 20 ka. The background tidal current amplitude U is based on the results of Uehara et al. (2006) (contours of U at 16, 12, 10, 8, 0 ka BP in the northwest European shelf seas were shown). A linear trend of U during 20–12 ka BP is assumed to obtain U at 20 ka BP. The ellipticity ($\epsilon = -0.4$) and the change in the principal current direction are based on the model results in Belderson et al. (1986). An initially undisturbed water depth of 15 m is used. The representative wave height and wave period are chosen to be $H_w = 3$ m and $T_w = 7$ s according to the findings in Neill et al. (2009).

The possible occurrence of quasi-active/moribund ridges for different values of R, H_0, U and $\Delta\varphi$ is examined in Exps. 6–9. In Exp. 6, $R = 1$ mm/yr represents the present-day condition (Shennan et al., 2006), and $R = 6.25$ mm/yr is the average rate of SLR for an increase of 125 m of water depth in 20 ka. In Exp. 7, different values of H_0 are used, and the choice of the values follows from the same argument (critical initial water depth) for the Dutch Banks. Exp. 8 uses a constant value of U (0.67 m/s) in time, which is the time-averaged velocity amplitude in Exp. 5. Finally, Exp. 9 neglects changes in the principal current direction.

For the Celtic Banks, the domain length L_y is chosen to be close to the observed spacing of the Celtic Banks at present, i.e., 15 km, which is approximately three times of the wavelength of the initially preferred bedform in Exp. 5. The principal current direction (37° anticyclonically rotated with respect to the x-axis) is

chosen such that the crest lines of the initially preferred bedform in Exp. 5 are parallel to the x-axis. The focus here is to gain insight into why active ridges become quasi-active/moribund, rather than to investigate the characteristics of quasi-active/moribund ridges in detail. For this reason, and because 2D (topography varies in both x- and y-directions) computations are very demanding in time, a 1D configuration (topography varies only in the y-direction) is employed.

4.3 RESULTS

4.3.1 *Active ridges subject to SLR only: sensitivity behavior to R*

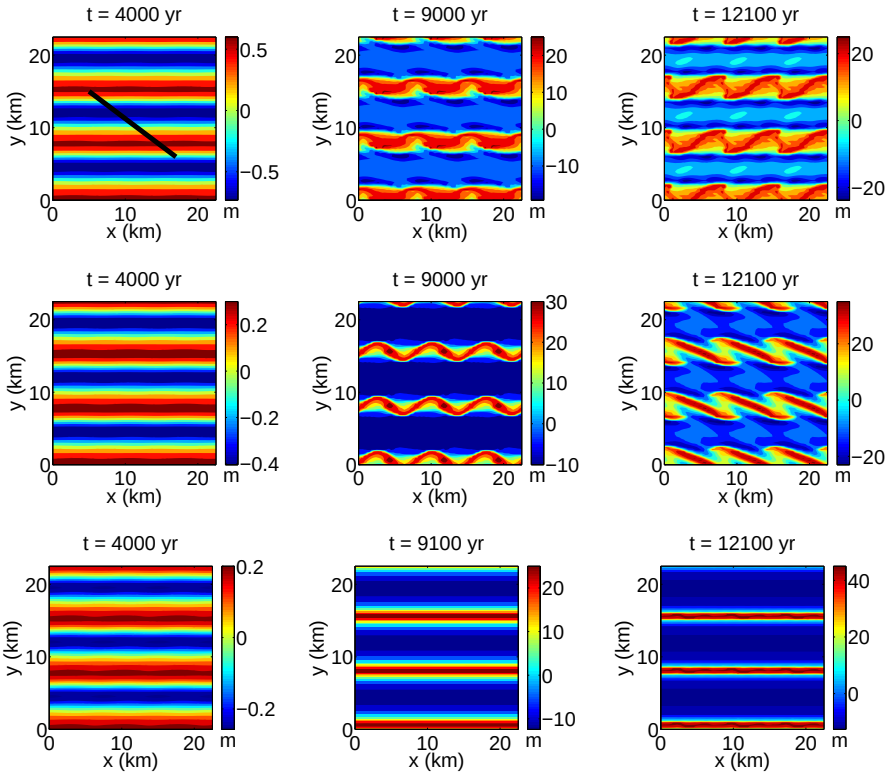

Figure 4.3: Snapshots of bed level h at different times for different rates R of SLR with an initially undisturbed water depth $H_0 = 30$ m and $U = 0.75$ m/s (Exp. 1). From top to bottom panels, $R = 0$, 1 and 1.875 mm/yr, respectively. The bed level obtained in the domain of 7.5 km×7.5 km is used to cover a domain with a size 3×3 times larger. The black line indicates the principal direction of the background tidal current $\vec{u}_0$.

Fig. 4.3 shows snapshots of the bed level at different times for different rates R of SLR with an undisturbed water depth H_0 of 30 m (Exp. 1). Spatially meandering crests are found in the case that SLR and tidal current variation are not considered (top panels). For relatively small rates of SLR of 1 mm/yr (middle panels), 0.5 mm/yr and 1.5 mm/yr (not shown), meandering crests still occur, but in the end the crests break (from one crest into two) and become stationary, and they are rotated with respect to the x-axis and become almost straight. Moreover, the spacing of the ridges decreases. In contrast, non-rotated straight crests parallel to the x-axis are observed for $R = 1.875$ mm/yr (bottom panels) and $R = 2.5$, 3 mm/yr (not shown) during the entire simulation period. The reasons for the presence of meandering crests, rotated and non-rotated straight crests in the end state are discussed in Section 4.4.1.

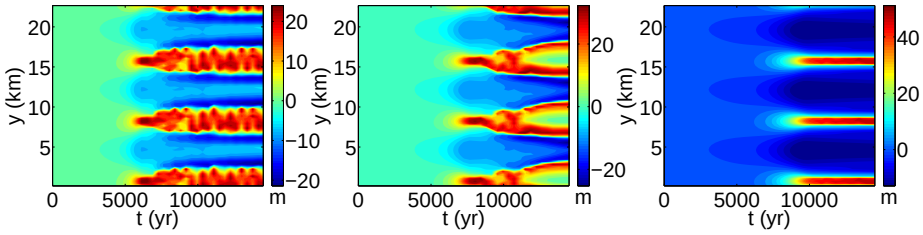

(a) $R = 0$ **(b)** $R = 1$ mm/yr **(c)** $R = 1.875$ mm/yr

Figure 4.4: Time evolution of the bed level along a transect at $x = 0.6$ km for different rates R of SLR with an initially undisturbed water depth $H_0 = 30$ m and $U = 0.75$ m/s (Exp. 1). (a) $R = 0$, (b) $R = 1$ mm/yr and (c) $R = 1.875$ mm/yr. The bed level obtained in the domain with $L_y = 7.5$ km is used to cover a domain with L_y that is 3 times larger.

In Fig. 4.4, the time evolution of the bed level along a transect in the y-direction is shown for different rates R of SLR with $H_0 = 30$ m (Exp. 1). Fig. 4.4a reveals that for $R = 0$ the meandering crests oscillate in time and shift in the y-direction. Similar behavior of the crests is seen for $R = 1$ mm/yr before $t = 10$ ka (Fig. 4.4b), while afterwards, the oscillation of the crests ceases. In the case that $R = 1.875$ mm/yr (Fig. 4.4c), the crest lines maintain their initial orientation.

Fig. 4.5 presents, for several rates R of SLR in Exp. 1, the time evolution of the characteristics of the ridges, i.e., the root mean square height h_{rms}, the global growth rate Γ, crest level with respect to the mean sea level $(h_{cr} - H)$ and relative ridge height h_{rel}. For a larger R, the global growth time τ_g and the root mean square height h_{rms} at time $t > \tau_g$ are larger, while the maximum global growth rate Γ is smaller. For $R = 3$ mm/yr, the global growth time has not been reached yet before the end of the simulation ($t = 15$ ka). In the cases that $R > 0$, the crest levels keep pace with the rising sea level, while the relative ridge height h_{rel} at time $t = \tau_g$ hardly changes ($h_{rel} \sim 90\%$).

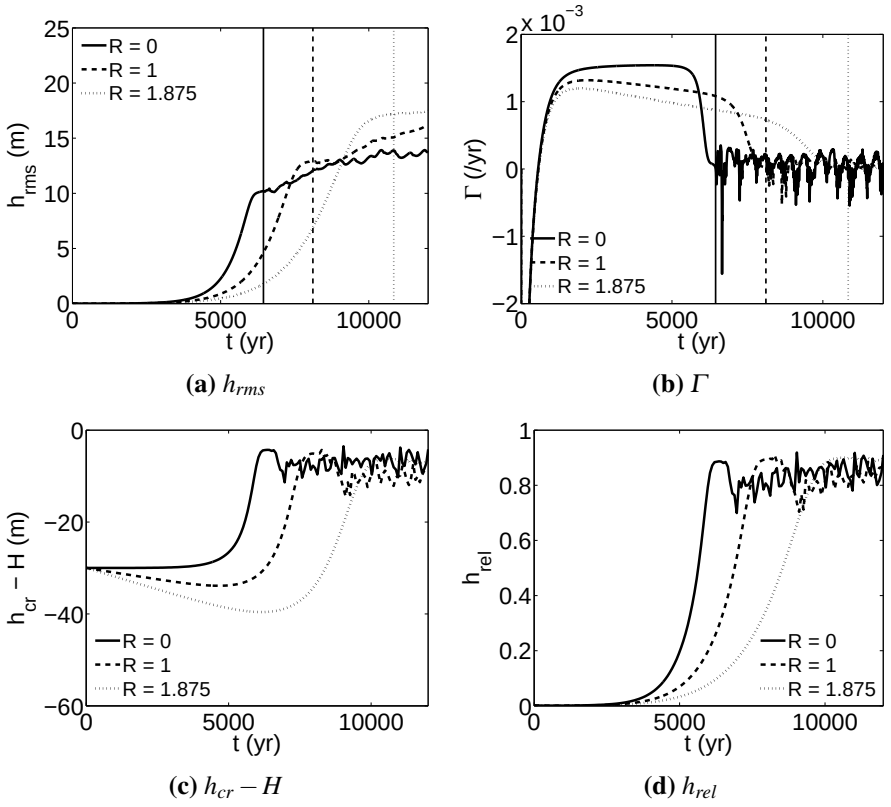

Figure 4.5: Time evolution of (a) the root mean square height h_{rms}, (b) the global growth rate Γ, (c) crest level with respect to the mean sea level $(h_{cr} - H)$, and (d) relative ridge height h_{rel} of the ridges for different rates R of SLR (unit: mm/yr) in Exp. 1. (c) and (d) are related to the bed level along a transect at $x = 0.6$ km. The vertical lines indicate the global growth time.

4.3.2 *Active ridges subject to SLR only: sensitivity behavior to H_0*

Fig. 4.6 shows the time evolution of the bed level along a transect in the y-direction for different values of the initially undisturbed water depth H_0 with a constant rate of SLR $R = 1.875$ mm/yr. It is seen that the spacing of the initially preferred bedform for $H_0 = 10$ m is smaller than that for relatively large depths $H_0 = 15$, 20 m. In all the cases, tidal sand ridges with spatially meandering crests occur (not shown), and the crests oscillate in time after the exponential growth stage. For $H_0 = 20$ m, the oscillation of the crests lasts for approximately 5 ka, afterwards it ceases and the orientation and spacing of the ridges change (the latter is not shown, as is seen in middle panels of Fig. 4.3). Changes in the orientation and spacing of the ridges are

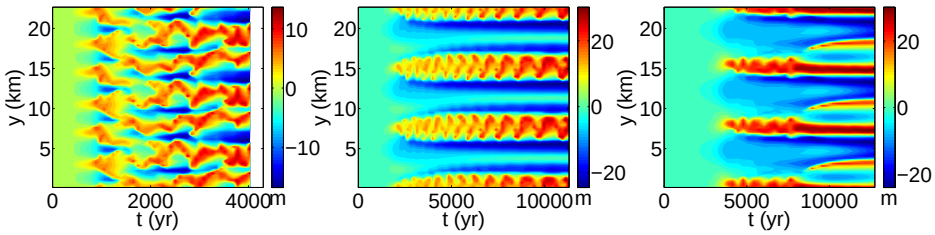

(a) $H_0 = 10$ m **(b)** $H_0 = 15$ m **(c)** $H_0 = 20$ m

Figure 4.6: As Fig. 4.4 but for different initially undisturbed water depth H_0 and a fixed rate of SLR $R = 1.875$ mm/yr (Exp. 2).

also found for $H_0 = 15$ m with $R = 3$ mm/yr and $H_0 = 20$ m with $R = 2.5$, 3 mm/yr (not shown).

Fig. 4.7 shows the global growth time τ_g and the root mean square height h_{rms} at time $t = \tau_g$ against the rate of SLR for different initial water depths H_0 (Exp. 2). As H_0 increases from 10 m to 30 m, the global growth time τ_g and the root mean square height h_{rms} at time $t = \tau_g$ increase significantly. For instance, for $R = 1.875$ mm/yr, $\tau_g = 0.9$, 2.2, 4.2, 11.0 ka for H_0 =10, 15, 20, 30 m respectively, and h_{rms} at time $t = \tau_g$ increases from 5 m to 17 m.

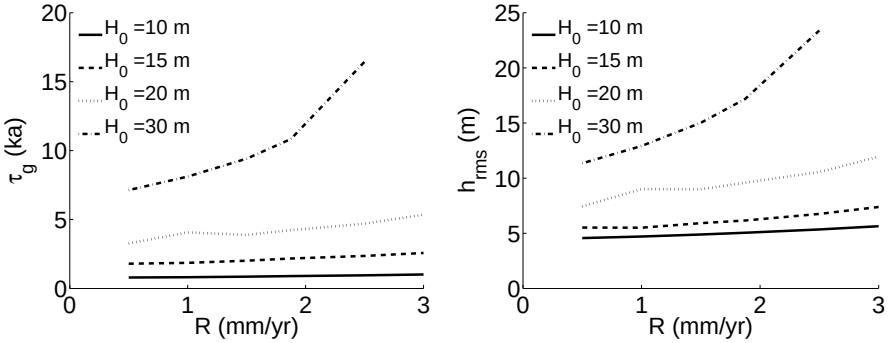

(a) **(b)**

Figure 4.7: (a) The global growth time τ_g and (b) the root mean square height h_{rms} at time $t = \tau_g$ against the rate of SLR for different water depths H_0 (Exp. 2). For comparison, the results for $H_0 = 30$ m (Exp. 1) are also presented.

4.3.3 *Active ridges subject to SLR and tidal current variation*

Based on the Holocene tidal conditions in the southern North Sea from van der Molen and de Swart (2001a), variation in the velocity amplitude and the principal direction of the background tidal current is considered in Exp. 3 and Exp. 4, respectively. The rate of SLR is kept fixed at $R = 1.875$ mm/yr and the initially undisturbed water depth is 15 m. Compared to the results of Exp. 2 (using a constant $U = 0.75$ m/s, $H_0 = 15$ m and $R = 1.875$ mm/yr), the time evolution of h_{rms}, Γ, h_{cr} and h_{rel} in Exp. 3 (using time-varying U) and Exp. 4 (not shown) is similar. The main difference in the results of Exps. 2–4 (using the same H_0 and R) is in the global growth time τ_g, i.e., τ_g is approximately 40% larger in Exps. 3–4 (using time-varying U) than that in Exp. 2. In addition, considering changes in the principal current direction (Exp. 4) results in sand ridges with a spacing of approximately 3.8 km all the time (not shown). In all the simulations of Exps. 3–4, except the one using a constant $U = 0.5$ m/s in Exp. 3, in the end meandering crests occur that oscillate in time. For the case of a constant $U = 0.5$ m/s in Exp. 3, the ridges grow quite slowly: h_{rms} is smaller than 1 m after a simulation time of 20 ka.

4.3.4 *Quasi-active/moribund ridges due to SLR and tidal current variation*

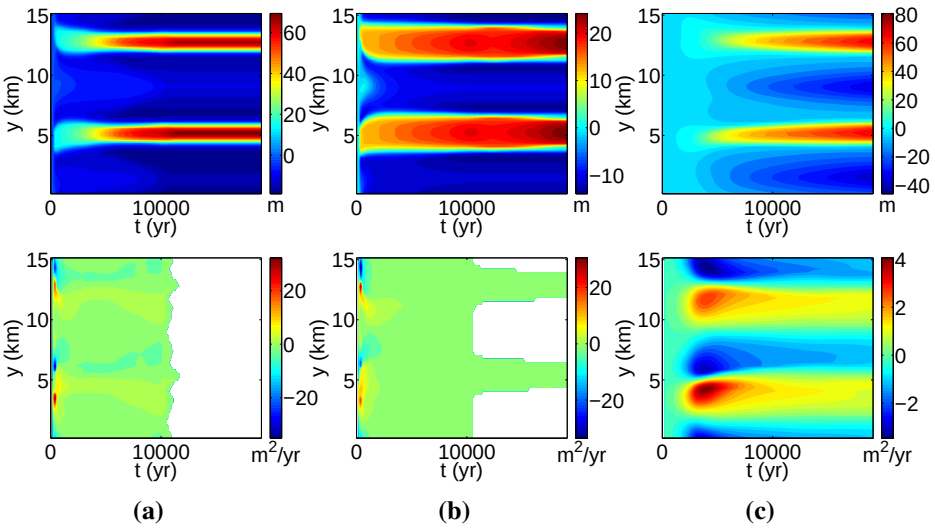

Figure 4.8: Time evolution of the bed level h (top panels) and tidally averaged sand transport along a transect in the y-direction $\langle q_y \rangle$ (bottom panels) in (a) Exp. 5, (b) Exp. 6 with $R =$ 1 mm/yr and (c) Exp. 8 with $U = 0.67$ m/s. For $\langle q_y \rangle$, white color means $\langle q_y \rangle = 0$.

Using the conditions that mimic those for the Celtic Banks, Exp. 5 is conducted to investigate the transition of ridges from active to quasi-active/moribund. The sensitivity of the occurrence of quasi-active/moribund ridges to R, H_0, U and $\Delta\varphi$ is examined in Exps. 6–9, respectively. To determine if a ridge is active, quasi-active or moribund, sand transport on the ridge is a direct measure. Fig. 4.8a shows the time evolution of the bed level h and tidally averaged sand transport $\langle q_y \rangle$ along a transect in the y-direction for Exp. 5. Two ridges appear within the domain of 15 km long. At time $t \sim 10.5$ ka, $\langle q_y \rangle$ becomes 0 in the regions near the troughs, while it still changes near the crests, i.e., the ridges become quasi-active. After time $t \sim 11.5$ ka, in the whole domain $\langle q_y \rangle = 0$, i.e., the ridges turn moribund.

Quite similar results as those in Exp. 5 are found in Exp. 6 using a constant rate of SLR $R = 6.25$ mm/yr (not shown). Fig. 4.8b shows the time evolution of h and $\langle q_y \rangle$ in Exp. 6 using $R = 1$ mm/yr. Quasi-active ridges are observed but no moribund ridges occur. For $t \leq 20$ ka, the regions near the crests are always active ($\langle q_y \rangle \neq 0$), whereas the regions near the troughs turn inactive ($\langle q_y \rangle = 0$) at time $t \sim 10.5$ ka, and the area of the inactive regions increases as the sea level rises. This suggests that quasi-active ridges will turn moribund in the end, but in a much longer period compared to that in Exp. 6 using $R = 6.25$ mm/yr, in which moribund ridges are observed within 12 ka.

For different values of initially undisturbed water depth H_0 (Exp. 7), transition from active ridges to quasi-active and moribund ridges still occurs at similar times as those in Exp. 5. From Fig. 4.8c, which shows the time evolution of h and $\langle q_y \rangle$ in Exp. 8, it appears that if the variation of the velocity amplitude is not considered, before $t = 20$ ka the sandy bed is always active everywhere. Changes in the principal current direction (Exp. 9) do not affect the occurrence of quasi-active/moribund ridges.

4.4 DISCUSSION

4.4.1 *Meandering crests, rotated and non-rotated straight crests*

The initial formation of tidal sand ridges has been explained by linear stability theory (Huthnance, 1982a). This concerns the study of the stability of a basic state, which is characterized by a spatially uniform background tidal current over a flat bottom, with respect to infinitesimal bottom perturbations. The latter are composed of Fourier modes (or bottom modes) that have an arbitrary wavelength and crest orientation with respect to the principal current direction. It was shown that for a strong tidal current (above 0.5 m/s), sand ridges form as a result of the joint action of the background tidal current and the residual current generated by tide-topography interactions. These results confirmed those of earlier qualitative studies by Zimmerman

(1980, 1981) and Robinson (1981), in which it was demonstrated that a residual current is generated by torques due to bottom friction and Coriolis force around a ridge that is obliquely oriented with respect to the principal current direction. In addition, the strongest residual current is found if the ridge is cyclonically rotated with respect to the principal current direction. Fig. 4.9 shows a sketch of the background tidal current, the residual current and the total current over a bottom mode during flood and ebb. In that case, the residual current acts with the background tidal current upstream of the ridge while it acts against the current downstream. Consequently, sand transport upstream of the crests is larger than that downstream, and so net accumulation of sand occurs above the crests, and thus growth of the ridge. The stronger the residual current, the faster the height of the ridge grows, as was shown for the case of a rectilinear background tidal current by Hulscher et al. (1993). The intensity of the residual current is maximum if the spacing of the ridges is of the order of the tidal excursion length, i.e, the distance that water particles travel in a tidal period.

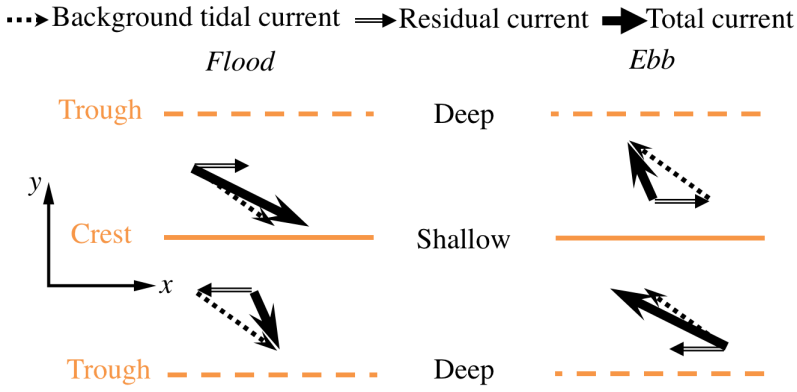

Figure 4.9: Sketch of the background tidal current, residual current and total current over a bottom mode during flood and ebb in the Northern Hemisphere. The bottom mode is simplified as crest (solid) and trough (dash) lines.

After some time from the beginning, the bottom mode of which the amplitude grows fastest (called the preferred mode/bedform) becomes dominant. This results in the presence of ridges of small heights with straight crests, as is seen in left panels of Fig. 4.3. Interestingly, for the chosen domain size for the Dutch Banks, the model results in Section 4.3 reveal that the behavior of ridges in the end state depends on the initial water depth H_0 and the rate R of SLR. Three different types of behavior in the end state are observed (see Fig. 4.3, right panels), i.e., meandering crests that oscillate in time, and straight crests that are either rotated or non-rotated with respect to the crests of the initially preferred bedform (or the x-axis). Fig. 4.10 shows the presence of meandering crests, rotated and non-rotated straight crests in the end state for different values of R and H_0 (from Exps. 1–2 and additional experiments

like Exp. 2 but $H_0 = 25$ m). It is seen that meandering crests occur for relatively small H_0, while non-rotated straight crests occur for relatively large H_0. For rotated straight crests, they are observed for small R with relatively large H_0 or relatively large R with intermediate H_0.

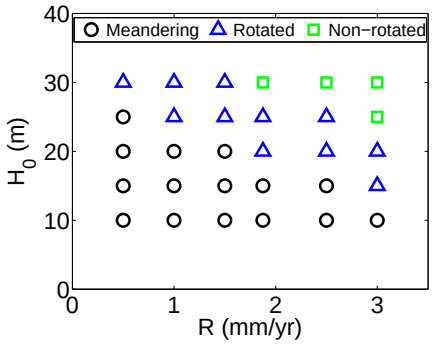

Figure 4.10: Presence of meandering crests (circle), rotated (triangle) and non-rotated (square) straight crests with respect to the x-axis in the end state for different values of rate R of SLR and initially undisturbed water depth H_0, using the settings of the Dutch Banks and a domain of 7.5 km×7.5 km.

Regarding meandering crests that oscillate in time, it was discussed in Chapter 3 that they are due to nonlinear interactions between the preferred bedform and bottom modes with crests normal/oblique to those of the preferred bedform. In particular, meandering crests occur if the domain length L_x is larger than the spacing of the initially preferred bedform λ_p, and the relative ridge height h_{rel} at the global growth time is above 80%. In relatively shallow waters (less than 50 m), the value of h_{rel} is inversely related to the amplitude of near-bed wave orbital velocity u_w, as stronger waves erode more sand at the crests. For the experiments setup, a larger L_x means that more bottom modes with crests normal/oblique to those of the initially preferred bedform are included in the domain.

Regarding the cases in which the end state is characterized by rotated straight crests with respect to the x-axis, it turns out that in the period before the end state, time-varying meandering crests occur. Moreover, the meandering crests show breaking behavior, i.e., a single crest breaks into two which are inclined with respect to the original crest (see middle panels of Fig. 4.3). The presence of meandering crests indicates that the amplitudes of bottom modes with crests normal/oblique to those of the initially preferred bedform become larger. The reason for this behavior is the following. If SLR is included, as the mean water depth H increases, the magnitude of the residual current generated by torques due to friction and Coriolis force decreases. This is because the frictional torque is proportional to H^{-2}, whereas the Coriolis

torque, the additional torque related to quadratic bed shear stress and dissipation of residual vorticity are all proportional to H^{-1} (Zimmerman, 1980; Robinson, 1981). To check whether changes in the residual current occur in the model, Fig. 4.11 shows the residual current over the topography in Exp. 1 with a constant rate of SLR of 1 mm/yr at different simulation times. A decrease in the magnitude of the residual current after around 10 ka in that experiment is indeed observed. A weaker residual current gives rise to smaller growth rates of the bottom modes, and thus overall a smaller global growth rate or a larger global growth time. As changes in the amplitudes of the bottom modes become slower, the nonlinear interactions between the bottom modes also weaken, which is manifested as a decrease in the amplitude of the oscillation of the crests (distance that the crests shift in the y-direction). Consequently, the alternate breaking and merging behavior of the crests ceases. The dominant bottom mode determines whether in the end state the crests are oblique or parallel to those of the initially preferred bedform. In the cases of relatively large H_0

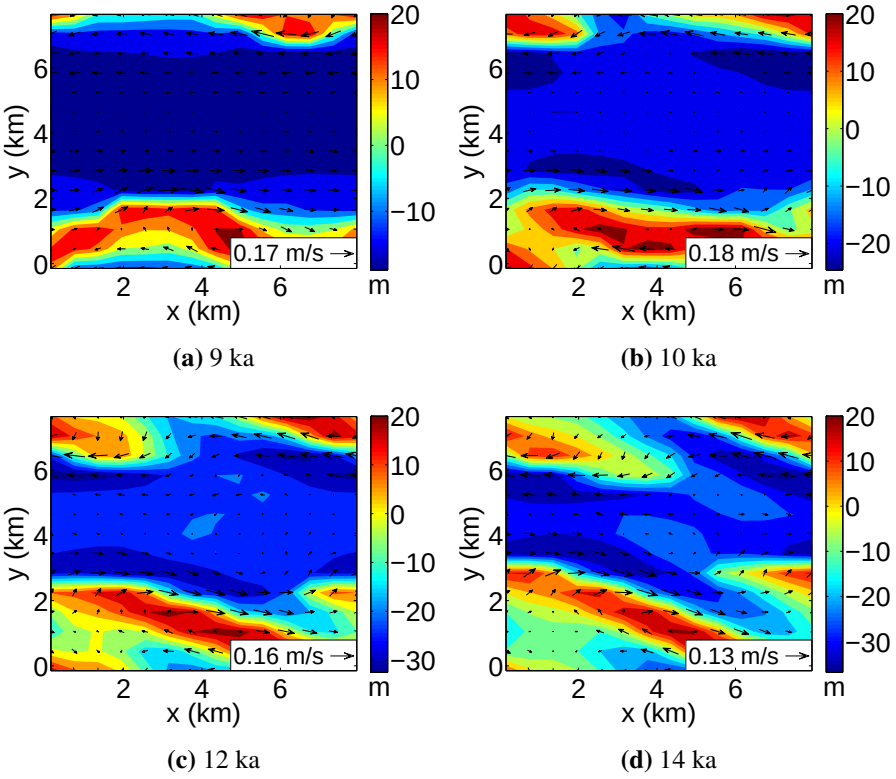

(a) 9 ka **(b)** 10 ka

(c) 12 ka **(d)** 14 ka

Figure 4.11: The residual current (vectors) over the topography (color map) in Exp. 1 with a constant rate of SLR of 1 mm/yr at different simulation times. The values in the white box indicate the maximum magnitude of the residual current.

(above 30 m) and relatively large R (above 2 mm/yr) for the considered domain size in Exp. 1, the nonlinear interactions between the bottom modes are so weak such that no meandering crests occur at all.

4.4.2 *Key for the transition from active to quasi-active/moribund ridges*

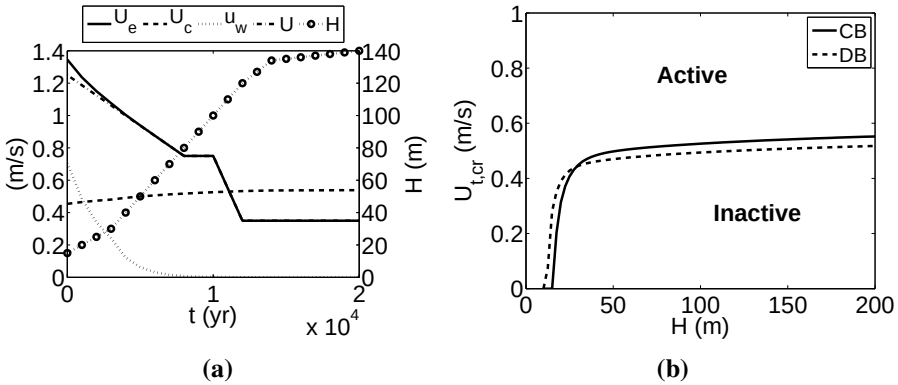

Figure 4.12: (a) Time evolution of the amplitude U_e of the effective velocity calculated as $U_e = (U^2 + 0.5u_w^2)^{1/2}$ (solid line) for a prescribed tidal current amplitude U (dot-dashed line), the critical velocity for sand erosion U_c (dashed line) and the amplitude of near-bed wave orbital velocity u_w (dotted line), using the mean water depth H (dot-circle line). (b) Critical amplitude of tidal current $U_{t,cr} = (U_c^2 - 0.5u_w^2)^{1/2}$ that determines whether the sandy bed is active or inactive locally in different water depths H under a constant wave climate. The wave climate and the grain size for the Celtic Banks (CB, solid line) and the Dutch Banks (DB, dashed line) were employed.

For the settings of the Celtic Banks, in Exp. 5 active ridges become quasi-active at the simulation time $t \sim 10.5$ ka and subsequently moribund at $t \sim 11.5$ ka. Fig. 4.12a shows the time evolution of the amplitude U_e of the effective velocity calculated as $U_e = (U^2 + 0.5u_w^2)^{1/2}$, the critical velocity for sand erosion U_c and the amplitude of the near-bed wave orbital velocity u_w using the mean water depth H of Exp. 5. The time when U_e becomes smaller than U_c agrees with the time when the ridges become quasi-active/moribund. In contrast, in Exp. 6 for a relatively small constant rate of SLR (1 mm/yr), it takes much longer time for the ridges to become moribund. The reason is that by prescribing U in time, as H increases, U_c increases while u_w and U_e decrease (Fig. 4.12a), thus the time that U_e reaches U_c is shorter if H increases faster (larger R). For the setting of the Dutch Banks, the insert in Fig. 4.2 also indicates that if the tidal current amplitude is kept at 0.5 m/s, as the sea level rises, ridges will become quasi-active and moribund in the long term.

Note that as H increases, u_w approaches 0, which means that the amplitude U_e of the effective velocity is approximately equal to the tidal current amplitude U, and the change in U_c is minor (Figs. 4.2 and 4.12a). Thus if U is noticeably larger than U_c, the time for U_e to become smaller than U_c will be extremely long. As is seen in Fig. 4.8c ($U = 0.67$ m/s, $U_c \sim 0.5$ m/s), there is no sign that the ridges will turn quasi-active on the considered time scale.

The above observation reveals that if initially the velocity amplitude U of the tidal current is noticeably larger than the critical velocity for sand erosion U_c, the key for the transition from active to quasi-active ridges is a decrease in U such that U_e becomes less than U_c. If initially U is just above U_c, SLR alone will also give rise to quasi-active ridges. Further for quasi-active ridges to turn completely moribund, the associated time depends inversely on the rate of SLR (see Figs. 4.8a-b). Using the wave climate and the grain size for the Celtic Banks and the Dutch Banks, Fig. 4.12b shows the critical tidal current amplitude $U_{t,cr}$ calculated by $U_{t,cr} = (U_c^2 - 0.5u_w^2)^{1/2}$, which determines if the sandy bed in different water depths is active or inactive. It is seen from Fig. 4.12b that typically quasi-active/moribund ridges occur if U is below 0.5 m/s in a water depth above around 50 m, while active ridges occur in areas where U is above 0.5 m/s.

4.4.3 *Sensitivity of the results to domain length*

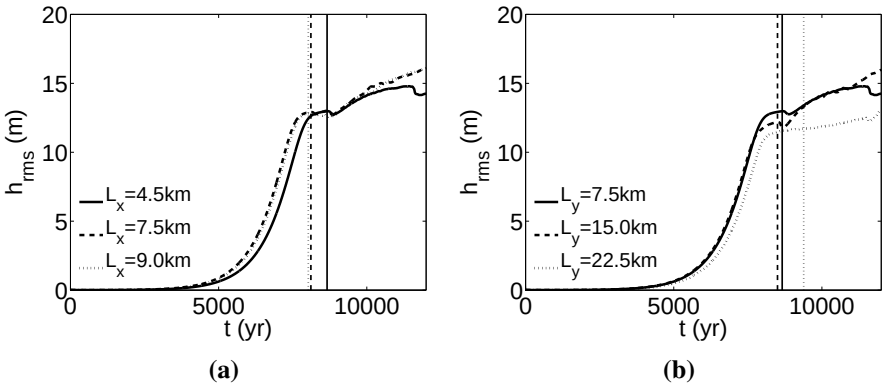

Figure 4.13: As Fig. 4.5a but for sensitivity of the results of Exp. 1 using $R = 1$ mm/yr to (a) L_x ($L_y = 7.5$ km) and (b) L_y ($L_x = 4.5$ km).

In the previous sections, for the Dutch Banks the domain length in the y-direction L_y was chosen to be equal to the spacing of the initially preferred bedform ($\lambda_p = 7.5$ km) under the present-day condition, and L_x was set equal to L_y. For the Celtic Banks, a 1D configuration was used and L_y was chosen based on the observed spa-

cing (15 km). Additional experiments were conducted to examine the sensitivity of the results of Exps. 1–5 to the domain length.

For Exp. 1, the experiment with the present-day setting $R = 1$ mm/yr, $H_0 = 30$ m, and $U = 0.75$ m/s was chosen as the reference case. First, L_y was fixed to 7.5 km and different values of L_x were used, i.e., $L_x = 3$, 4.5, 6, 9 km. Fig. 4.13a shows the root mean square height h_{rms} against time for different L_x. For the default setting ($L_y = L_x = 7.5$ km), the global growth time τ_g is 8.1 ka and h_{rms} at time τ_g is 12.9 m. For different values of L_x, the relative changes in τ_g and h_{rms} at time τ_g are within 12% and 4%, respectively. Figs. 4.14a–c show the time evolution of the bed level along a transect at $x = 0.6$ km for different values of L_x. In all the cases, except the one in which $L_x = 3$ km, during the growth phase meandering crests occur that oscillate in time, and in the end state rotated straight crests are observed (not shown, similar to what is displayed in middle panels of Fig. 4.3). The reason that straight crests occur in the case $L_x = 3$ km is that L_x is smaller than λ_p, as was discussed in Section 4.4.1.

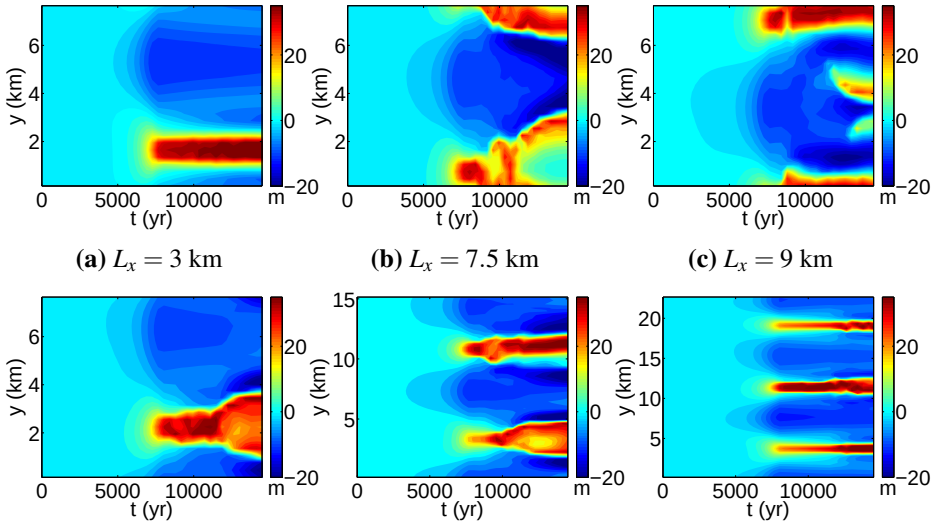

(a) $L_x = 3$ km **(b)** $L_x = 7.5$ km **(c)** $L_x = 9$ km

(d) $L_y = 7.5$ km **(e)** $L_y = 15$ km **(f)** $L_y = 22.5$ km

Figure 4.14: As Fig. 4.4b but with no extension in the y-direction for (a)-(c) different length L_x ($L_y = 7.5$ km), (d)-(f) different length L_y ($L_x = 4.5$ km) in Exp. 1 using $R = 1$ mm/yr. Note the differences in scales in the plots d–f.

Next, different values of L_y were used. Integer times of λ_p were considered, such that the initially preferred bedform would fit in the domains, i.e., $L_y = 15$, 22.5 km ($L_x = 4.5$ km was chosen for reasons of computational efficiency). Fig. 4.13b shows the root mean square height h_{rms} against time for different L_y. Compared to the

results using $L_x = 4.5$ km and $L_y = 7.5$ km, for different values of L_y, the relative changes in τ_g and h_{rms} at time τ_g are within 9% and 14%, respectively. Figs. 4.14d–f show the time evolution of the bed level along a transect at $x = 0.6$ km for different values of L_y. Changes in the orientation and spacing of the ridges still occur for $L_y =$ 15 km (not shown). In the case of $L_y = 22.5$ km, two meandering crests together with a non-rotated straight crest (at $y \approx 4$ km) occur at the end of simulation time $t = 15$ ka (not shown). In all the cases with different values of L_x and L_y, the relative ridge height h_{rel} is approximately 90% at time $t = \tau_g$. The above analysis reveals that if a larger domain is used, the behavior of the ridges may differ from that in a smaller domain, especially if more bottom modes with crests normal/oblique to those of the initially preferred bedform are included (a larger L_x). The reason is that the intensity of the nonlinear interactions is enhanced by including more bottom modes.

In Exps. 2–4, different initial values of undisturbed water depth H_0 and tidal current amplitude U were used, but the domain size was kept fixed. Thus, in these cases L_y was not equal to the wavelength of the initially preferred bedform. Linear stability analysis revealed that for $H_0 = 10$, 15, 20 m with $U = 0.75$ m/s (Exp. 2), the initially preferred bedform has a spacing of 3.9, 5.1 and 6.3 km, respectively, and for $H_0 = 15$ m with $U = 0.5$ m/s (Exps. 3 and 4), the initially preferred bedform has a spacing of 4.5 km. For the above conditions the crests are all $37 \pm 1°$ cyclonically rotated with respect to the principal direction of the background tidal current. To examine the consequence of choosing a fixed L_y, additional simulations were carried out in which L_y was equal to the spacing of the initially preferred bedform λ_p. This was done for Exp. 2 using $R = 1.875$ mm/yr and Exps. 3–4 using time-varying U. The results were compared with those of Exps. 2–4 using $L_y = 7.5$ km and $R = 1.875$ mm/yr. The relative differences in τ_g and h_{rms} at time τ_g are all within 20% and 18%, respectively. The features of meandering crests and rotated straight crests in the end state in the experiments using $L_y = \lambda_p$ are similar to those in the experiments using a fixed L_y of 7.5 km (not shown). Another difference for Exp. 4 using different L_y is that only one crest occurs in the domain with $L_y = 4.5$ km, while two crests occur in the domain with $L_y = 7.5$ km.

For Exp. 5, a larger domain with $L_y = 30$ km was used. Four ridges appear in the domain, with a spacing in the range of 5–10 km, and a height of 60–100 m. Similar to the results using $L_y = 15$ km, the ridges become quasi-active at simulation time $t \sim 10.5$ ka and moribund at $t \sim 11.5$ ka.

4.4.4 *Comparison between modeled and observed tidal sand ridges*

In Roos et al. (2004), from Fourier analysis of the present-day seabed topography in the area of the Dutch Banks, the dominant spacing of tidal sand ridges in the area was shown to be in the range of 5.7–9.8 km, the height of the ridges is around 8 m and the relative ridge height is around 26%. The settings of Exp. 4 (Table 4.2) in the

simulation period from $t = 0$ to $t = 8$ ka mimic the overall changes in the sea level and the tidal current in the area of the Dutch Banks from 8 ka BP to the present. The modeled ridges have a spacing of approximately 4 km, they reach their global growth time at $t = 4$ ka and their relative height is around 85% afterwards. At $t = 8$ ka, the height of the ridges is approximately 40 m.

The southeastern sand ridges in the Celtic Sea have a spacing of around 15 km and are 20–50 m high, the water depth above the crests is around 110 m (Belderson et al., 1986), and the relative height is 15%–31%. The settings of Exp. 5 (Table 4.2) represent the changes in the sea level and the tidal current during the last 20 ka for the Celtic Banks. For $L_y = 15$ km, the model yields a spacing of 7.5 km and the ridge height is 90 m ($h_{rel} = 57\%$), and for $L_y = 30$ km, the modeled spacing is 5–10 km and the ridge height is between 60–100 m ($h_{rel} = 38\% - 63\%$).

The differences in the spacing, the growth stage (before or after the global growth time) and the height between modeled and observed ridges are due to several reasons, some of which have already been discussed in Chapter 3, i.e., simplification in the composition of tidal constituents and fixed domain size. Besides these reasons, other reasons are discussed below.

First, the uncertainty in the amplitude U of the tidal current and the strong sensitivity of the ridge height to U contribute to those differences. For the Dutch Banks, compared to the case of a constant current amplitude of 0.75 m/s (Exp. 2 using $H_0 = 15$ m and $R = 1.875$ mm/yr), using a constant current amplitude of 0.5 m/s (Exp. 3) significantly slows down the growth of the ridges. In Exp. 3 ($U = 0.5$ m/s), at the simulation time 8 ka the ridge height is less than 1 m (not shown). It is thus plausible that the observed Dutch Banks are still in the growth stage, while in the model setting of Exp. 4 the growth rate of the ridges was overestimated. The latter strongly depends on the chosen values of the tidal current amplitude U, the rate R of SLR and the initial water depth H_0. As is seen in Fig. 4.7a, the global growth time increases as R or H_0 increases, especially for the latter one.

Second, the formulation of the effective velocity $u_e = (|\vec{u}|^2 + 0.5u_w^2)^{1/2}$ follows that of Roos et al. (2004), whereas different expressions of u_e are present in other studies. For instance, the formulation of Soulsby-Van Rijn in Soulsby (1997) for u_e is $u_e = \left(|\vec{u}|^2 + (0.009/C_d)u_w^2\right)^{1/2}$ for monochromatic waves, where C_d is the drag coefficient. It turns out that, using the latter formulation, the contribution of wave stirring to u_e, i.e., the coefficient in front of u_w^2, is approximately 9 times larger for a water depth of 15 m, which means a 3 times larger wave height in the latter case. Since u_w approaches 0 as the water depth increases (see e.g. Fig. 4.2), different formulations of u_e affect the evolution of sand ridges in shallow waters (less than 50 m). Using $u_e = \left(|\vec{u}|^2 + (0.009/C_d)u_w^2\right)^{1/2}$ for Exps. 4 and 5, both the initially preferred bedforms have a spacing of 9.6 km, and compared to the results using $u_e = (|\vec{u}|^2 + 0.5u_w^2)^{1/2}$, their initial growth rates decrease, especially for the Dutch Banks (by approximately 60%).

Also, only bed load sand transport was considered in the present model; a modified formulation of Fredsøe and Deigaard (1992) was used and the coefficients in this formulation (including the bed slope coefficient Λ) were not tuned. Soulsby (1997) showed that using different formulations for bed load sand transport yields transports rates that vary by a factor of more than 4. Roos et al. (2004) found that, by using a formulations for suspended load transport instead of bed load transport or by increasing Λ, the value of h_{rel} became smaller in the end state. Furthermore, it was assumed that erodibility of the bottom was not obstructed by e.g. rocky structures. Limited availability of sand prevents the ridge height from keeping increasing, and thus it accelerates the process that active ridges turn quasi-active/moribund.

Finally, the wave conditions are assumed to be constant in time. In reality, wave heights and wave periods change on both large (decades and centuries) and small (days to months) time scales. Roos et al. (2004) showed that in waters with depths less than 50 m, as the amplitude of near-bed wave orbital velocity increases, the relative ridge height decreases. As was shown in Neill et al. (2009), the present-day peak annual significant wave height H_s (10–15 m) and peak annual peak wave period T_p (18–19 s) in the Celtic Sea are much larger than the annual root mean square values of H_s (3–4 m) and T_p (7–8 s), and the same applies to the southern North Sea. Houthuys et al. (1994) presented an example that showed the effect of short-term variation of wave conditions (due to storm) on tidal sand ridges. They observed that changes in the surface level of sand waves (rhythmic bedforms with a spacing in the order of 100 m) on top of the Middelkerke Bank in the southern North Sea reached up to 1.2 m after successive storms within 3 months.

Note that the bed shear stress (see Eq. 3.1) is calculated using the tidal current alone, whereas waves also contribute to the bed shear stress. The effect of the additional contribution of wind waves to the bed shear stress is similar to an increase in the linear friction coefficient as in Roos et al. (2004), which results in a smaller spacing and a larger growth rate.

To summarize, there are quantitative differences between modeled and observed ridges, but the model results are highly sensitive to the chosen values of the parameters. Note that there are also many similarities between modeled and observed ridges. Similar successive ridges, as seen in the middle right panel of Fig. 4.3 (model results), are observed in the area of Norfolk Banks (Hearty Knoll, Winterton Ridge, Hammond Knoll and Hasborough Sand) in the southern North Sea (Caston, 1972). The spacings between these observed ridges (especially Hearty Knoll, Winterton Ridge and Hammond Knoll, approximately 3.5 km) are smaller than those of the ridges observed further offshore. The model results, which show breaking behavior of crests and decreases in the spacing of the ridges under SLR, suggest that the formation of these observed successive ridges with relatively small spacings may be related to changes in the sea level. Also, the reason why active ridges become quasi-active shown in this study could explain the evolution of other offshore sand ridges, such

as those in the eastern Yellow Sea (Park et al., 2006) and the East China Sea (Liu et al., 2007).

4.5 CONCLUSIONS

The dynamics of tidal sand ridges subject to changes in the sea level and tidal conditions in the long term are studied by using a nonlinear morphodynamic model. The focus has been on the sensitivity of the growth time and height of active ridges to SLR and tidal current variation, as well as on the reason why active ridges become quasi-active/moribund. Two basic settings have been examined, which mimic the situations of the Dutch Banks and the Celtic Banks.

Generally active tidal sand ridges occur if the velocity amplitude of the tidal current U is large (typically above 0.5 m/s). For active ridges, considering SLR makes the root mean square height h_{rms} of the ridges keep on increasing. For larger fixed rate of SLR, the global growth time τ_g becomes larger, so does h_{rms} at time $t = \tau_g$. For a smaller initial U, τ_g is larger. If variation in the principal current direction is accounted for, changes in the growth time and height of the ridges are minor. For the parameter setting used in this study, in a fixed domain, three types of behavior of active ridges in the end state are observed: meandering crests that oscillate in time, and straight crests that are either rotated or non-rotated with respect to the crests of the initially preferred bedform. The final behavior of the ridges depends on the initial conditions (depth, tidal current amplitude), changes in the sea level and tidal current amplitude and the number of bottom modes in the domain.

Within the considered time range (20 ka), assuming a constant wave climate (wave height and wave period), if initially the tidal current amplitude U is noticeably larger than the critical velocity for sand erosion U_c, a decrease in U such that U becomes approximately smaller than U_c plays a key role in the occurrence of quasi-active ridges. In the case that initially $U \sim U_c$, SLR alone will also give rise to quasi-active ridges. The time scale for quasi-active ridges to turn further moribund is inversely proportional to the rate of SLR. Modeled sand ridges qualitatively agree with observed sand ridges, but spacings are underestimated and heights are overestimated.

4.A CRITICAL WATER DEPTH FOR FORMATION OF RIDGES

To obtain the critical water depth close to 0, below which tidal sand ridges do not form, the characteristics of waves and tidal currents in water depths close to 0 need to be obtained. Following Young and Verhagen (1996), the wave energy E relates to the water depth H, wind speed U_{10} at a height of 10 m above the water surface and fetch length F by

$$\frac{g^2E}{U_{10}^4} = 3.64\times10^{-3}\left[\tanh A_1 \tanh\left(\frac{B_1}{\tanh A_1}\right)\right]^{1.74}, \tag{4.A1}$$

with

$$A_1 = 0.493\left(\frac{gH}{U_{10}^2}\right)^{0.75}, \qquad B_1 = 3.13\times10^{-3}\left(\frac{gF}{U_{10}^2}\right)^{0.57}. \tag{4.A2}$$

The significant wave height H_s is thus calculated as $H_s = 4\sqrt{E}$. The peak wave period T_p is calculated from

$$\frac{U_{10}}{gT_p} = 0.133\left[\tanh A_2 \tanh\left(\frac{B_2}{\tanh A_2}\right)\right]^{-0.37}, \tag{4.A3}$$

with

$$A_2 = 0.331\left(\frac{gH}{U_{10}^2}\right)^{1.01}, \qquad B_2 = 5.215\times10^{-4}\left(\frac{gF}{U_{10}^2}\right)^{0.73}. \tag{4.A4}$$

To obtain the velocity amplitude of the background tidal current in a water depth close to 0, it is assumed that the pressure gradient force $\vec{F}_p$ remains constant in time for small water depths. Using Eq. 2.3 and applying Lorentz linearization of the bed shear stress (Zimmerman, 1982), the following equations for (u, v) on a flat bottom are derived

$$\frac{\partial u}{\partial t} - fv = F_{px} - \frac{rUu}{H}, \qquad \frac{\partial v}{\partial t} + fu = F_{py} - \frac{rUv}{H}. \tag{4.A5}$$

Here, $r = \frac{8}{3\pi}C_dU$ is the linear friction coefficient, U is the velocity amplitude (a function of H), and F_{px} and F_{py} are the components of $\vec{F}_p$ in the x- and y-directions. Writing $(u, v, F_{px}, F_{py}) = \Re\{(\hat{u}, \hat{v}, \hat{F}_{px}, \hat{F}_{py})e^{-\mathrm{i}\omega t}\}$, where $\Re$ means real part, $\mathrm{i} = \sqrt{-1}$ and the symbol $\hat{}$ indicates the complex amplitude, a system for the complex amplitudes of the flow $(\hat{u}, \hat{v})$ is derived. From the assumption that $\vec{F}_p$ is constant in time and using the conditions at certain location, e.g. the area of the Dutch Banks ($H = 15$ m, $U = 0.5$ m/s and $\epsilon = -0.2$, as in Exp. 4), $(\hat{F}_{px}, \hat{F}_{py})$ are calculated.

Consequently, the system for $(\hat{u}, \hat{v})$ is closed, and for any H, the velocity amplitude U is obtained.

To obtain the effective velocity u_e given by $u_e = (|\vec{u}|^2 + 0.5u_w^2)^{1/2}$, following Soulsby (2006), the amplitude of the depth-dependent wave-induced near-bed orbital velocity u_w is parameterized as

$$u_w = \frac{H_w}{2}\left(\frac{g}{\tilde{D}}\right)^{\frac{1}{2}} \exp\left\{-\left[\frac{4.41}{T_w}\left(\frac{\tilde{D}}{g}\right)^{\frac{1}{2}}\right]^{2.45}\right\}. \tag{4.A6}$$

Here, H_w and T_w represent the wave height and wave period of a monochromatic wave, respectively. The reason to use Eq. 4.A6 instead of the physical formulation of u_w from linear wave theory is that the physical formulation of u_w is an implicit function of water depth and iteration is required to obtain u_w.

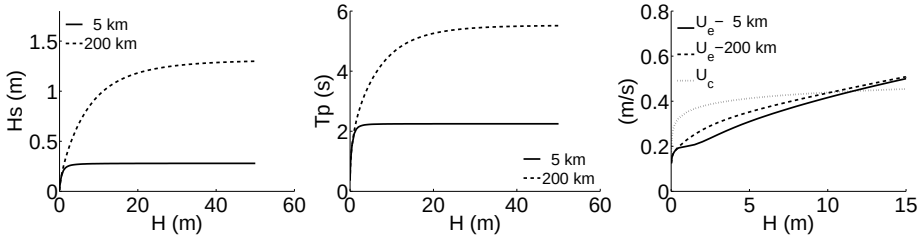

(a) H_s **(b)** T_p **(c)** U_e

Figure 4.A1: (a) Significant wave height H_s and (b) peak wave period T_p versus water depth H for a range of fetch length (5–200 km, see legend) and a constant wind climate $U_{10} = 8$ m/s, calculated from Eqs. 4.A1–4.A4. (c) Amplitude U_e of the effective velocity $u_e = (|\vec{u}|^2 + 0.5u_w^2)^{1/2}$ and critical velocity for sand erosion U_c versus H, with u_w calculated from Eq. 4.A6 using H_s and T_p in (a) and (b) as the wave height H_w and period T_w, and U obtained from the assumption that the pressure gradient force $\vec{F}_p$ is constant and the same as that at 8 ka BP in the southern North Sea (Exp. 4).

Figs. 4.A1a and b show the significant wave height H_s and peak wave period T_p versus water depth H for a wide range of fetch length (5–200 km) and a constant wind climate $U_{10} = 8$ m/s that represent the wind climate in the North Sea (Grabemann and Weisse, 2008). It is seen that for H larger than 10 m, H_s and T_p can be assumed to be constant. Fig. 4.A1c shows the amplitude U_e of the effective velocity $u_e = (|\vec{u}|^2 + 0.5u_w^2)^{1/2}$ versus H by using H_s and T_p in Figs. 4.A1a and b as the wave height H_w and period T_w, and assuming that $\vec{F}_p$ is constant in time and is the same as that at 8 ka BP in the southern North Sea (see settings of Exp. 4). A critical water depth H_{0c} (below which no sand transport occurs) of approximately 10 m is found, which is not sensitive to the choice of H_s and T_p for that setting.

5

SUMMARY AND OUTLOOK

5.1 SUMMARY

Tidal sand ridges are large-scale bedforms with horizontal dimensions of several kilometers, heights of 5–50 meters, and their crests are cyclonically (5°–30°) rotated with respect to the principal direction of the tidal current. They occur in the offshore area of shelf seas that have a wide range of water depths (10–200 m). Based on their present-day behavior, tidal sand ridges are classified as 'active' (sand transport everywhere), 'quasi-active' (sand transport in parts of the ridge area) and 'moribund' (sand transport nowhere). They evolve on a timescale of centuries due to tide-topography interactions and they are shaped by wind waves. During their evolution, ridges are also affected by changes in sea level, strength and direction of the tidal current.

Although linear and nonlinear dynamics of tidal sand ridges have been the topics of a few model studies, there are still several aspects of the dynamics of the ridges which deserve further investigation. A literature survey resulted in three specific research questions (see Section 1.5 in Chapter 1). The first one concerns the initial formation of these bedforms. In particular, the effect of different formulations of bed shear stress and sand transport, tidal ellipticity and different tidal constituents on the characteristics of these bedforms (growth rate, wavelength, orientation of the preferred bedforms) has not been thoroughly explored. This topic was systematically examined in Chapter 2.

Also with respect to the nonlinear evolution of tidal sand ridges, several aspects remain unexplored (see research question 2 in Chapter 1, Section 1.5). They concern the sensitivity of the characteristics of finite-height ridges (their shape and growth time) to either 1D or 2D configurations (topography varies in one/two horizontal dimensions) with unlimited sand, tidal ellipticity and critical bed shear stress for sand erosion. These aspects were examined in Chapter 3, in which constant sea level and tidal conditions were assumed.

In reality, the characteristics of the sea level and the tidal current change on the growth time scales of tidal sand ridges, while how these changes affect the evolution of sand ridges has not been investigated (see research question 3 in Chapter 1, Section 1.5). Chapter 4 extended the work in Chapter 3 to study the effect of changes in the sea level and the amplitude and principal direction of the tidal current on the growth time and height of active tidal sand ridges. Besides, the role of sea level rise and tidal current variation in the presence of quasi-active/moribund ridges was explored.

To improve the understanding of those aspects of the initial formation and long-term evolution of tidal sand ridges mentioned above, an idealized nonlinear morphodynamic model was developed and used. The model described a coupled system of tidally forced depth-averaged currents and the erodible sandy bed in the offshore area of shelf seas. Compared to the previous models, several advantages of the present model are identified. In particular, the model accounts for topography that varies in two horizontal dimensions, elliptical tidal currents that are composed of different tidal constituents, critical bed shear stress for sand erosion, SLR and tidal current variation. Summaries of the results and conclusions in Chapter 2 to Chapter 4 are presented in Section 5.1.1 to Section 5.1.3, respectively.

5.1.1 *Effect of formulations of bed shear stress, sand transport and tidal forcing on growth characteristics of tidal sand ridges*

The results in Chapter 2 show that the formulations for bed shear stress and slope-induced sand transport are not critical for the initial formation of tidal sand ridges. For these ridges, under rectilinear tidal currents, increasing the critical velocity for sand erosion decreases the growth rate and the wavelength of the preferred bedform significantly, while the orientation angle slightly decreases. Besides tidal sand ridges, long bed waves are also found if the critical velocity for sand erosion is slightly smaller than the tidal current amplitude. The dependence of the growth rate, wavelength and the orientation of the preferred bedform on the tidal ellipticity is non-monotonic. A decrease in tidal frequency results in a preferred bedform with a larger wavelength and a smaller orientation angle, while its growth rate hardly changes. In the case of joint diurnal and semidiurnal tides, or spring-neap tides, the characteristics of the bedforms are determined by the dominant tidal constituent. The model results also provide a possible explanation for the fact that the Dutch Banks have a larger wavelength than that of the Flemish Banks in the southern North Sea.

5.1.2 *Effect of 1D/2D configurations, elliptical tidal currents and critical bed shear stress on finite-height behavior of tidal sand ridges*

The results in Chapter 3 show that in the case of a 1D configuration, the root mean square height h_{rms} of tidal sand ridges first grows exponentially and hereafter saturates. In the end, ridges in static equilibrium are obtained, i.e., h_{rms} remains constant. In contrast, when the configuration is 2D, ridges are found with spatially meandering crests that oscillate in time. Initially the bedforms are composed of a finite number of bottom modes. The meanders occur if bottom modes with crests normal to those of the initially preferred bedform exist, and their topographic wavenumbers are in the order of that of the preferred bedform or smaller. In addition, the vertical distance between the crest and trough levels should be larger than around 80% of the maximum water depth. Generally, the global growth time, i.e., the time at which h_{rms} stops increasing after the exponential growth stage of the bedforms, is slightly larger for a 2D than for a 1D configuration.

The shapes of the ridges are sensitive to the tidal ellipticity, while they are hardly sensitive to the critical bed shear stress. The global growth time varies non-monotonically with the tidal ellipticity, and it increases if the critical bed shear stress is included. Comparison between the model results and field observations suggests that the model is able to simulate the gross characteristics of the Dutch Banks and the Flemish Banks in the southern North Sea and that these ridges may still be growing.

5.1.3 *Finite-height behavior of tidal sand ridges subject to SLR and tidal current variation*

The results in Chapter 4 reveal that generally active tidal sand ridges occur if the tidal current amplitude is larger than 0.5 m/s. For these ridges, with increasing rates of sea level rise, their growth time becomes longer, and the root mean square height keeps on increasing. A smaller initial tidal current amplitude gives rise to a larger growth time, while changes in the principal current direction have a minor effect on the characteristics of the ridges.

On the considered time scale, assuming a constant wave climate, quasi-active tidal sand ridges occur mainly as a result of a decreasing tidal current amplitude such that the effective velocity (in the sense of stirring sand) becomes smaller than the critical velocity for sand erosion. The ridges further become moribund on a time scale that depends inversely on the rate of sea level rise. Modeled ridges are compared with the observed ridge. A few similarities are found and quantitative differences are explained.

5.2 OUTLOOK

The present model study has provided new insight into several aspects of linear and nonlinear dynamics of tidal sand ridges. With regard to future research, several extensions are suggested.

First, replacing prescribed background tidal currents, as was done in this thesis, by tidal currents from larger scale models in which sea level rise is taken into account, would add more realism. One possibility is to 'nest' the present model in models like that of Uehara et al. (2006). In this way, detailed output of tidal currents from paleotidal simulations serves as input for the present model. Alternatively, including a module of bottom evolution (through sand transport) in large scale models that simulate paleotides could be considered.

Second, improving the modeling of waves including variation of wave conditions is important. It has been shown that wave conditions change both in the long term and in the short term, and these changes affect the evolution of the ridges, especially the short-term extreme wave conditions (Houthuys et al., 1994). Improvement in modeling the waves can be achieved by prescribing long-term (decades to centuries) and seasonal variations in the wave height and wave period as well as sudden events (storms). The latter can be parameterized as events that are computed from a given probability distribution. Furthermore, note that the way of including the stirring of sand by wind waves was parametric. To gain insight into the effect of wave transformation on the long-term evolution of the ridges, wave models such as the wave transformation model in Caballeria et al. (2002) or spectral wave models like SWAN (Booij et al., 1999) are needed.

Third, in the present model several aspects that relate to sand transport could be improved, which are listed below. To explore the effect of both bed load and suspended load on the long-term evolution of sand ridges, a challenge is to account for suspended load based on the characteristics of the flow and the sediment (Soulsby, 1997). Roos et al. (2004) considered both bed load and suspended load to study the nonlinear dynamics of tidal sand ridges, and they found that using suspended load leads to lower and more rounded crests than those using bed load. Note that in that study bed load and suspended load were included in an isolated way by prescribing coefficients that control the relative importance of bed load and suspended load. Another challenge is to take into account a mixture of sand of different sizes, as in Walgreen et al. (2004) and Roos et al. (2007), such that knowledge of the grain size variation over finite-height ridges (instead of ridges with small heights in previous studies) will be obtained. Besides, considering the availability of sand according to the thickness of local erodible seabed is an interesting topic, which may provide better description of the characteristics of sand ridges. Huthnance (1982a) showed that the cross-sectional profiles of the ridges are sensitive to the availability of sand.

In addition, limited source of sand prevents ridges from keeping pace with SLR, thus accelerates the process that active ridges turn quasi-active/moribund.

Fourth, it is quite a challenge to examine the natural evolution of the wavelength and orientation of the bedforms in the long term. This could be addressed by using a considerably large 2D domain. To do such kind of simulations, computational efficiency of the present model needs to be improved, possibly by using parallel computation as in e.g. the non-hydrostatic wave-flow model SWASH (Zijlema et al., 2011).

Fifth, to gain further insight into transient response of finite-height ridges to interventions (van Lancker et al., 2010), it is worthwhile to use the present model to study the long-term behavior of finite-height ridges subject to sand extraction. Several studies (Idier et al., 2010, and references therein) have been conducted to investigate the impact of offshore sand extraction on the local hydrodynamic and morphodynamic conditions. However, those studies either were limited in computation efficiency for simulations longer than a century or they employed simplified topography, i.e., a 1D configuration or a 2D configuration with perturbations of small amplitudes. Sand extraction could be applied in the same way as that of Nnafie et al. (2014b), in which the effect of sand extraction on shoreface-connected sand ridges was investigated.

Last, there is a potential to apply the present model to ridges at locations other than the European shelf seas, such as the shelf seas of China (Liu et al., 1998) and the Australian shelf seas (Harris, 1994). Attention needs to be paid to suspended load transport of sand, sediment input and outflow from rivers. This holds in particular for areas like the Yellow Sea and the East China Sea on the continental shelf of China, where generally the grain size is less than 0.25 mm, and which receive large amounts of sediment and fresh water from big rivers. Knaapen (2009) shows from observation that interaction between the tidal current and outflow of a river affects the formation of sand ridges. It is feasible to account for sediment input and outflow from rivers in the present model by adjustment of its boundary conditions. Besides tidal sand ridges, the present model can also be used to unravel the nonlinear behavior of long bed waves as observed by Knaapen et al. (2001) and van Dijk et al. (2011) (see also Chapter 2), where their initial formation was studied). This can be achieved by conducting a nonlinear stability analysis for cases that the maximum current velocity is slightly above the critical velocity for sand erosion.

BIBLIOGRAPHY

Bailard, J. A., Inman, D. L., March 1981. An energetics bedload model for a plane sloping beach: local transport. Journal of Geophysical Research 86 (C3), 2035–2043.

Beets, D. J., van der Spek, A. J. F., 2000. The Holocene evolution of the barrier and the back-barrier basins of Belgium and the Netherlands as a function of late Weichselian morphology, relative sea-level rise and sediment supply. Geologie en Mijnbouw / Netherlands Journal of Geosciences 79 (1), 3–16.

Behre, K. E., 2007. A new Holocene sea-level curve for the southern North Sea. Boreas 36, 82–102.

Belderson, R. H., Pingree, R. D., Griffiths, D. K., 1986. Low sea-level origin of celtic sea sand banks-evidence from numerical modelling of M_2 tidal streams. Marine Geology 73, 99–108.

Berné, S., Lericolais, G., Marsset, T., Bourillet, J. F., De Batist, M., 1998. Erosional offshore sand ridges and lowstand shorefaces: examples from tide-and wave-dominated environments of France. Journal of Sedimentary Research 68 (4).

Berné, S., Trentesaux, A., Stolk, A., Missiaen, T., De Batist, M., 1994. Architecture and long term evolution of a tidal sandbank: the Middelkerke Bank (southern North Sea). Marine Geology 121 (1-2), 57–72.

Besio, G., Blondeaux, P., Vittori, G., 2006. On the formation of sand waves and sand banks. Journal of Fluid Mechanics 557, 1–27.

Blondeaux, P., 2001. Mechanics of coastal forms. Annual Review of Fluid Mechanics 33, 339–370.

Blondeaux, P., de Swart, H. E., Vittori, G., 2009. Long bed waves in tidal seas: an idealized model. Journal of Fluid Mechanics 636, 485–495.

Booij, N., Ris, R., Holthuijsen, L. H., 1999. A third-generation wave model for coastal regions: 1. model description and validation. Journal of geophysical research: Oceans 104 (C4), 7649–7666.

Borsje, B. W., Roos, P. C., Kranenburg, W. M., Hulscher, S. J. M. H., 2013. Modeling tidal sand wave formation in a numerical shallow water model: The role of turbulence formulation. Continental Shelf Research 60, 17–27.

Boyd, S. E., Limpenny, D. S., Rees, H. L., Cooper, K. M., 2005. The effects of marine sand and gravel extraction on the macrobenthos at a commercial dredging site (results 6 years post-dredging). ICES Journal of Marine Science 62, 145–162.

Caballeria, M., Coco, G., Falqués, A., Huntley, D. A., 2002. Self-organization mechanisms for the formation of nearshore crescentic and transverse sand bars. Journal of Fluid Mechanics 465, 379–410.

Calvete, D., de Swart, H. E., 2003. A nonlinear model study on the long-term behavior of shore face–connected sand ridges. Journal of Geophysical Research 108 (C5), 3169, doi:10.1029/2001JC001091.

Carbajal, N., Montaño, Y., 2001. Comparison between predicted and observed physical comparison between predicted and observed physical features of sandbanks. Estuarine, Coastal and Shelf Science 52, 425–443.

Caston, V. N. D., 1972. Linear sand banks in the southern North Sea. Sedimentology 18, 63–78.

Coco, G., Murray, A. B., 2007. Patterns in the sand: From forcing templates to self-organization. Geomorphology 91 (3), 271–290.

Coco, G., Murray, A. B., Green, M. O., Thieler, E. R., Hume, T. M., 2007. Sorted bed forms as self-organized patterns: 2. complex forcing scenarios. Journal of Geophysical Research 112 (F03016), doi:10.1029/2006JF000666.

Collins, M. B., Shimwell, S., Gao, S., Powell, H., Hewitson, C., Taylor, J. A., 1995. Water and sediment movement in the vicinity of linear sandbanks: the Norfolk Banks, southern North Sea. Marine Geology 123, 125–142.

Davies, A. M., Furnes, G. K., 1980. Observed and computed M_2 tidal currents in the North Sea. Journal of Physical Oceanography 10, 237–257.

Degrendele, K., Roche, M., Schotte, P., Lancker, V. V., Bellec, V., Bonne, W., 2010. Morphological evolution of the Kwinte Bank central depression before and after the cessation of aggregate extraction. Journal of Coastal Research SI (51), 77–86.

Deigaard, R., Drønen, N., Fredsøe, J., Jensen, J. H., Jørgensen, M. P., 1999. A morphological stability analysis for a long straight barred coast. Coastal Engineering 36, 171–195.

Dias, F., Kharif, C., 1999. Nonlinear gravity and capillary-gravity waves. Annual Review of Fluid Mechanics 31, 301–346.

Dodd, N., Blondeaux, P., Calvete, D., de Swart, H. E., Falqués, A., Hulscher, S. J. M. H., Rozynski, G., Vittori, G., 2003. Understanding coastal morphodynamics using stability methods. Journal of Coastal Research 19 (4), 849–865.

Dyer, K. R., Huntley, D. A., 1999. The origin, classification and modelling of sand banks and ridges. Continental Shelf Research 19, 1285–1330.

Fleming, K., Johnston, P., Zwartz, D., Yokoyama, Y., Lambeck, K., Chappell, J., 1998. Refining the eustatic sea-level curve since the Last Glacial Maximum using far- and intermediate-field sites. Earth and Planetary Science Letters 163, 327–342.

Fredsøe, J., Deigaard, R., 1992. Mechanics of coastal sediment transport. World Scientific.

Gallagher, E. L., 2011. Computer simulations of self-organized megaripples in the nearshore. Journal of Geophysical Research: Earth Surface 116, F01004, doi:10.1029/2009JF001473.

Gao, S., Collins, M. B., Lanckneus, J., Moor, G. D., Lancker, V. V., 1994. Grain size trends associated with net sediment transport patterns: An example from the Belgian continental shelf. Marine Geology 121, 171–185.

Garnier, R., Calvete, D., Falqués, A., Caballeria, M., 2006. Generation and nonlinear evolution of shore-oblique/transverse sand bars. Journal of Fluid Mechanics 567, 327–360.

Grabemann, I., Weisse, R., 2008. Climate change impact on extreme wave conditions in the north sea: an ensemble study. Ocean Dynamics 58 (3-4), 199–212.

Harris, P., 1994. Comparison of tropical, carbonate and temperate, siliciclastic tidally dominated sedimentary deposits: examples from the australian continental shelf. Australian Journal of Earth Sciences 41 (3), 241–254.

Houbolt, J., 1968. Recent sediments in the southern bight of the North Sea. Geologie en Mijnbouw 47 (4), 245–273.

Houthuys, R., Trentesaux, A., De Wolf, P., 1994. Storm influences on a tidal sandbank's surface (Middelkerke Bank, southern North Sea). Marine Geology 121 (1-2), 23–41.

Hulscher, S. J. M. H., 1996. Tidal-induced large-scale regular bed form patterns in a three-dimensional shallow water model. Journal of Geophysical Research 101 (C9), 20727–20744.

Hulscher, S. J. M. H., de Swart, H. E., de Vriend, H. J., 1993. The generation of offshore tidal sand banks and sand waves. Continental Shelf Research 13 (11), 1183–1204.

Huthnance, J. M., 1982a. On one mechanism forming linear sand banks. Estuarine, Coastal and Shelf Science 14, 79–99.

Huthnance, J. M., 1982b. On the formation of sand banks of finite extent. Estuarine, Coastal and Shelf Science 15, 277–299.

Idier, D., Astruc, D., 2003. Analytical and numerical modeling of sandbanks dynamics. Journal of Geophysical Research 108, C3 3060, doi:10.1029/ 2001JC001205.

Idier, D., Hommes, S., Brière, C., Roos, P. C., Walstra, D.-J. R., Knaapen, M. A. F., Hulscher, S. J. M. H., 2010. Morphodynamic models used to study the impact of offshore aggregate extraction: a review. Journal of Coastal Research SI (51), 39–52.

Kenyon, N. H., Belderson, R. H., Stride, A. H., Johnson, M. A., 1981. Offshore tidal sand-banks as indicators of net sand transport and as potential deposits. Special Publication International Association of Sedimentology 5, 257–268.

Klein, M. D., Schuttelaars, H. M., 2005. Morphodynamic instabilities of planar beaches: sensitivity to parameter values and process formulations. Journal of Geophysical Research 110 (F04S18), doi:10.1029/2004JF000213.

Knaapen, M. A. F., 2009. Sandbank occurrence on the Dutch continental shelf in the North Sea. Geo-Marine Letters 29, 17–24.

Knaapen, M. A. F., Hulscher, S. J. M. H., de Vriend, H. J., 2001. A new type of sea bed waves. Geophysical Research Letters 28 (7), 1323–1326.

Komarova, N. L., Newell, A. C., 2000. Nonlinear dynamics of sand banks and sand waves. Journal of Fluid Mechanics 415, 285–321.

Kubicki, A., Manso, F., Diesing, M., 2007. Morphological evolution of gravel and sand extraction pits, Tromper Wiek, Baltic Sea. Estuarine, Coastal and Shelf Science 71, 647–656.

Lambeck, K., 1995. Late Devensian and Holocene shorelines of the British Isles and North Sea from models of glacio-hydro-isostatic rebound. Journal of the Geological Society 152 (3), 437–448.

Lesser, G., Roelvink, J., Van Kester, J., Stelling, G., 2004. Development and validation of a three-dimensional morphological model. Coastal engineering 51 (8), 883–915.

Liu, Z., Berné, S., Saito, Y., Yu, H., Trentesaux, A., Uehara, K., Yin, P., Liu, J. P., Li, C., Hu, G., Wang, X., 2007. Internal architecture and mobility of tidal sand ridges in the East China Sea. Continental Shelf Research 27 (13), 1820–1834.

Liu, Z., Xia, D., Berné, S., Wang, K., Marsset, T., Tang, Y., Bourillet, J., 1998. Tidal deposition systems of China's continental shelf, with special reference to the eastern Bohai Sea. Marine Geology 145, 225–253.

Miller, M. C., McCave, I. N., Komar, P. D., 1977. Threshold of sediment motion under unidirectional currents. Sedimentology 24, 507–527.

Neill, S. P., Scourse, J. D., Bigg, G. R., Uehara, K., 2009. Changes in wave climate over the northwest European shelf seas during the last 12,000 years. Journal of Geophysical Research 114, C06015, doi:10.1029/2009JC005288.

Nelson, T. R., Voulgaris, G., 2015. A spectral model for estimating temporal and spatial evolution of rippled seabeds. Ocean Dynamics 65 (2), 155–171.

Nnafie, A., de Swart, H. E., Calvete, D., Garnier, R., 2014a. Effects of sea level rise on the formation and drowning of shoreface-connected sand ridges, a model study. Continental Shelf Research 80, 32–48.

Nnafie, A., de Swart, H. E., Calvete, D., Garnier, R., 2014b. Modeling the response of shoreface-connected sand ridges to sand extraction on an inner shelf. Ocean Dynamics 64, 723–740.

Off, T., 1963. Rhythmic linear sand bodies caused by tidal currents. Bulletin of the American Association of Petroleum Geologists 47, 324–341.

Park, S.-C., Lee, B.-H., Han, H.-S., Yoo, D.-G., Lee, C.-W., 2006. Late Quaternary stratigraphy and development of tidal sand ridges in the eastern Yellow Sea. Journal of Sedimentary Research 76 (9), 1093–1105.

Pattiaratchi, C., Collins, M., 1987. Mechanisms for linear sandbank formation and maintenance in relation to dynamical oceanographic observations. Progress in Oceanography 19, 117–176.

Price, T., Ruessink, B., Castelle, B., 2014. Morphological coupling in multiple sandbar systems-a review. Earth Surface Dynamics 2 (1), 309.

Pugh, D. T., 1996. Tides, Surges and Mean Sea-Level (reprinted with corrections). John Wiley & Sons Ltd.

Robinson, I., 1981. Tidal vorticity and residual circulation. Deep Sea Research 28A (3), 195–212.

Roebert, T. J., 2014. Optimization of offshore wind farm power cable routing. Master's thesis, University of Twente.

Roelvink, J. A., 2006. Coastal morphodynamic evolution techniques. Coastal Engineering 53, 277 – 287.

Roos, P. C., Hulscher, S. J. M. H., 2006. Nonlinear modeling of tidal sandbanks: Wavelength evolution and sand extraction. In: Smith, J. M. (Ed.), Proceedings of the 30th International Conference on Coastal Engineering (ICCE2006). San Diego, US, pp. 2761–2771.

Roos, P. C., Hulscher, S. J. M. H., de Vriend, H. J., 2008. Modelling the morphodynamic impact of offshore sandpit geometries. Coastal Engineering 55, 704–715.

Roos, P. C., Hulscher, S. J. M. H., Knaapen, M. A. F., 2004. The cross-sectional shape of tidal sandbanks: modelling and observation. Journal of Geophysical Research 109, F02003, doi:10.1029/2003JF000070.

Roos, P. C., Hulscher, S. J. M. H., Peters, B., Nemeth, A., 2001. A simple morphodynamic model for sand banks and large-scale sand pits subject to asymmetrical tides. In: Ikeda, S. (Ed.), Proceedings of the 2nd IAHR Symposium on River, Coastal and Estuarine Morphodynamics. IAHR, Hokkaido, Japan, pp. 91–100.

Roos, P. C., Wemmenhove, R., Hulscher, S. J. M. H., Hoeijmakers, H. W. M., Kruyt, N. P., 2007. Modeling the effect of nonuniform sediment on the dynamics of offshore tidal sandbanks. Journal of Geophysical Research 112, F02011, doi:10.1029/2005JF000376.

Ryan, W. B. F., Carbotte, S. M., Coplan, J., O'Hara, S., Melkonian, A., Arko, R., Weissel, R., Ferrini, V., Goodwillie, A., Nitsche, F., Bonczkowski, J., Zemsky, R., 2009. Global multi-resolution topography synthesis. Geochemistry Geophysics Geosystems 10 (Q03014), doi:10.1029/2008GC002332.

Sanders, J. A., Verhulst, F., Murdock, J., 2007. Averaging Methods in Nonlinear Dynamical Systems, 2nd Edition. Springer Science & Business Media.

Scourse, J., Uehara, K., Wainwright, A., 2009. Celtic Sea linear tidal sand ridges, the Irish Sea Ice Stream and the Fleuve Manche: palaeotidal modelling of a transitional passive margin depositional system. Marine Geology 259 (1), 102–111.

Seminara, G., 1998. Stability and morphodynamics. Meccanica 33, 59–99.

Shapiro, G. I., van der Molen, J., de Swart, H. E., 2004. The effect of velocity veering on sand transport in a shallow sea. Ocean Dynamics 54, 415–423.

Shennan, I., Bradley, S., Milne, G., Brooks, A., Bassett, S., Hamilton, S., 2006. Relative sea-level changes, glacial isostatic modelling and ice-sheet reconstructions from the British Isles since the Last Glacial Maximum. Journal of Quaternary Science 21 (6), 585–599.

Shore Protection Manual, 1984. Shore Protection Manual. Coastal Engineering Research Center, US Army Corps of Engineers, Washington DC, USA.

Simpson, J. H., Sharples, J., 2012. Introduction to the Physical and Biological Oceanography of Shelf Seas. Cambridge University Press.

Smith, D. B., 1988. Stability of an offset kink in the North Hinder Bank. In: P. L. De Boer, A. Van Gelder, S. D. N. (Ed.), Tide-Influenced Sedimentary Environments and Facies. D. Reidel Publishing Company, Dordrecht, pp. 65–78.

Soulsby, R. L., 1997. Dynamics of Marine Sands: A Manual for Practical Applications. Thomas Telford, London.

Soulsby, R. L., 2006. Simplified calculation of wave orbital velocities. Tech. Rep. TR-155, HR Wallingford Ltd.

Soulsby, R. L., Whitehouse, R. J. S., 1997. Threshold of sediment motion in coastal environments. In: Proceedings Pacific Coasts and Ports 1997 Conference, Christchurch. University of Canterbury, New Zealand, Wallingford, pp. 149–154.

Soulsby, R. L., Whitehouse, R. J. S., 2005. Prediction of ripple properties in shelf seas. Mark 2 predictor for time evolution. Tech. Rep. TR155 Release 2.0, HR Wallingford Ltd, UK.

Spencer, T., Brooks, S. M., Evans, B. R., Tempest, J. A., Möller, I., 2015. Southern North Sea storm surge event of 5 December 2013: water levels, waves and coastal impacts. Earth-Science Reviews 146, 120–145.

Stride, A. H., Belderson, R. H., Kenyon, N. H., Johnson, M. A., 1982. Offshore tidal deposits: sand sheet and sand bank facies. In: Stride, A. H. (Ed.), Offshore Tidal Sands: Processes and deposits. Chapman and Hall, London, pp. 95–125.

Talmon, A., Struiksma, N., Mierlo, M. V., 1995. Laboratory measurements of the direction of sediment transport on transverse alluvial-bed slopes. Journal of Hydraulic Research 33 (4), 495–517.

Tambroni, N., Blondeaux, P., 2008. Sand banks of finite amplitude. Journal of Geophysical Research 113, C10028, doi:10.1029/2007JC004658.

Toffoli, A., Fernandez, L., Monbaliu, J., Benoit, M., Gagnaire-Renou, E., Lefevre, J. M., Cavaleri, L., Proment, D., Pakozdi, C., Stansberg, C. T., Waseda, T., Onorato, M., 2013. Experimental evidence of the modulation of a plane wave to oblique perturbations and generation of rogue waves in finite water depth. Physics of Fluids 25, 090701.

Trentesaux, A., Stolk, A., Berne, S., 1999. Sedimentology and stratigraphy of a tidal sand bank in the southern North Sea. Marine Geology 159, 253–272.

Uehara, K., Scourse, J. D., Horsburgh, K. J., Lambeck, K., Purcell, A. P., 2006. Tidal evolution of the northwest European shelf seas from the Last Glacial Maximum to the present. Journal of Geophysical Research 111, C09025, doi:10.1029/2006JC003531.

van Dalfsen, J. A., Essink, K., Madsen, H. T., Birklund, J., Romero, J., Manzanera, M., 2000. Differential response of macrozoobenthos to marine sand extraction in the North Sea and the Western Mediterranean. ICES Journal of Marine Science 57, 1439–1445.

van der Molen, J., de Swart, H. E., 2001a. Holocene tidal conditions and tide-induced sand transport in the southern North Sea. Journal of Geophysical Research 106 (C5), 9339–9362.

van der Molen, J., de Swart, H. E., 2001b. Holocene wave conditions and wave-induced sand transport in the southern North Sea. Continental Shelf Research 21, 1723–1749.

van Dijk, T., van der Tak, C., de Boer, W., Kleuskens, M., Doornenbal, P., Noorlandt, R., Marges, V., 2011. The scientific validation of the hydrographic survey policy of the Netherlands Hydrographic Office, Royal Netherlands Navy. Tech. Rep. 1201907-000-BGS-0008, Deltares.

van Dijk, T. A. G. P., van Dalfsen, J. A., Lancker, V. V., van Overmeeren, R. A., van Heteren, S., Doornenbal, P. J., 2012. Benthic habitat variations over tidal ridges, North Sea, the Netherlands. In: Harris, P. T., Baker, E. K. (Eds.), Seafloor Geomorphology as Benthic Habitat-GeoHAB Atlas of Seafloor Geomorphic Features and Benthic. Elsevier Inc, pp. 241–249.

van Gaalen, J. F., Kruse, S. E., Coco, G., Collins, L., Doering, T., 2011. Observations of beach cusp evolution at Melbourne Beach, Florida, USA. Geomorphology 129 (1), 131–140.

van Lancker, V. R., Bonne, W., Garel, E., Degrendele, K., Roche, M., den Eynde, D. V., Bellec, V., Brière, C., Collins, M. B., Velegrakis, A. F., 2010. Recommendations for the sustainable exploitation of tidal sandbanks. Journal of Coastal Research 51, 151–164.

van Santen, R. B., de Swart, H. E., van Dijk, T. A. G. P., 2011. Sensitivity of tidal sand wavelength to environmental parameters: A combined data analysis and modelling approach. Continental Shelf Research 31, 966–978.

Velegrakis, A. F., Ballay, A., Poulos, S., Radzevicius, R., Bellec, V., Manso, F., 2010. European marine aggregates resources: origins, usage, prospecting and dredging techniques. Journal of Coastal Research SI (51), 1–14.

Vis-Star, N. C., de Swart, H. E., Calvete, D., 2008. Patch behaviour and predictability properties of modelled finite-amplitude sand ridges on the inner shelf. Nonlinear Processes in Geophysics 15, 943–955.

Walgreen, M., Calvete, D., de Swart, H. E., 2002. Growth of large-scale bed forms due to storm-driven and tidal growth of large-scale bed forms due to storm-driven and tidal currents: a model approach. Continental Shelf Research 22, 2777–2793.

Walgreen, M., de Swart, H. E., Calvete, D., 2004. A model for grain-size sorting over tidal sand ridges. Ocean Dynamics 54, 374–384.

Warren, I., Bach, H., 1992. MIKE 21: a modelling system for estuaries, coastal waters and seas. Environmental Software 7 (4), 229–240.

Yang, C., 1989. Active, moribund and buried tidal sand ridges in the East China Sea and the southern Yellow Sea. Marine Geology 88, 97–116.

Yool, A., Fasham, M. J., 2001. An examination of the "continental shelf pump" in an open ocean general circulation model. Global Biogeochemical Cycles 15 (4), 831–844.

Young, I., Verhagen, L., 1996. The growth of fetch limited waves in water of finite depth. part 1. total energy and peak frequency. Coastal Engineering 29 (1-2), 47–78.

Zijlema, M., Stelling, G., Smit, P., 2011. SWASH: an operational public domain code for simulating wave fields and rapidly varied flows in coastal waters. Coastal Engineering 58 (10), 992–1012.

Zimmerman, J., 1980. Vorticity transfer by tidal currents over an irregular topography. Journal of Marine Research 38 (4), 601–630.

Zimmerman, J., 1982. On the lorentz linearization of a quadratically damped forced oscillator. Physics Letters A 89 (3), 123–124.

Zimmerman, J. T. F., 1981. Dynamics, diffusion and geomorphological significance of tidal residual eddies. Nature 290 (5807), 549–555.

SAMENVATTING

Getijdezandbanken zijn grootschalige bodemvormen met hoogtes van 5–50 meter. De afstand tussen opeenvolgende zandbanken bedraagt 5–10 km en hun kammen zijn zo'n 5–30° cyclonaal (antikloks op het noordelijk halfrond) gedraaid ten opzichte van de richting van de dominante getijstroom. Ze zijn te vinden op het continentale plat, in waterdieptes van 10–200 m. Gebaseerd op hun huidige gedrag zijn getijdezandbanken geclassificeerd als 'actief' (overal zandtransport), 'gedeeltelijk actief' (zandtransport op bepaalde plekken rondom de zandbank) en 'inactief' (geen zandtransport). De zandbanken groeien, op een tijdschaal van honderden jaren, als gevolg van getij-topografie interactie en ze worden mede gevormd door windgolven. Zowel veranderingen van zeeniveau als veranderingen in de sterkte en richting van getijstroom beïnvloeden de ontwikkeling van de zandbanken.

Hoewel er meerdere modelstudies gedaan zijn naar de initiële vorming (lineaire dynamica) en lange-termijn gedrag (niet-lineaire dynamica) van getijdezandbanken, zijn er nog steeds aspecten die aandacht verdienen. Een literatuurstudie resulteerde in drie specifieke onderzoeksvragen (zie Sectie 1.5 in Hoofdstuk 1). De eerste betreft de initiële ontwikkeling van de zandbanken. Met name het effect van verschillende formuleringen van de bodemschuifspanning (lineaire/niet-lineaire) en het zandtransport (kritische bodemschuifspanning voor zanderosie en helling-geïnduceerd zandtransport), de ellipticiteit van de getijstroming en de rol van verschillende getijcomponenten op de eigenschappen van de zandbanken (groeisnelheid, golflengte, oriëntatie van kammen) zijn niet goed onderzocht. Dit onderwerp is systematisch bestudeerd in Hoofdstuk 2.

Ook wat betreft de lange-termijn ontwikkeling van de getijdezandbanken blijven meerdere aspecten onderbelicht (zie onderzoeksvraag 2 in Hoofdstuk 1, Sectie 1.5). Dat betreft met name de verschillen in de eigenschappen van de zandbanken (hun hoogte, vorm en groeitijd) wanneer, in plaats van een 1D configuratie (topografie verschilt in één dimensie) een 2D-configuratie wordt gebruikt. Parameters die zijn gevariëerd zijn de getij-ellipticiteit en de kritische bodemschuifspanning voor zanderosie. Dit is onderzocht in Hoofdstuk 3, waar voldoende beschikbaarheid van zand, alsmede een constant zeeniveau en getij-condities zijn aangenomen.

In werkelijkheid variëren de karakteristieken van het zeeniveau en de getijstroming op dezelfde tijdsschaal als de groei van getijdezandbanken, maar het is nog niet onderzocht hoe deze de evolutie van zandbanken beïnvloeden (zie onderzoeksvraag 3 in Hoofdstuk 1, Sectie 1.5). Hoofdstuk 4 borduurt voort op het werk in Hoofdstuk 3 door de effecten van verandering in zeeniveau en de amplitude en dominante richting van de stroming op de groeitijd, vorm en hoogte van de actieve getijdezand-

banken te kwantificeren. Verder is ook de rol van zeespiegelstijging en de variatie in getijstroming in de buurt van gedeeltelijk actief/inactief zandbanken onderzocht.

Om meer inzicht te verkrijgen in de processen die verantwoordelijk zijn voor de initiële vorming en op lange-termijn ontwikkeling van getijdezandbanken, is een geïdealiseerd, niet-lineair, morfodynamisch model ontwikkeld en gebruikt. Het model beschrijft tussen de door het getij geforceerde diepte-gemiddelde stroming, windgolven en de erodeerbare zandbodem op het continentale plat. Vergeleken met eerdere modellen heeft dit model meerdere voordelen. In het bijzonder beschrijft het model een topografie die varieert in twee horizontale richtingen, elliptische getijstromingen ten gevolge van verschillende getijcomponenten (dubbeldaags, enkeldaags), een kritische bodemschuifspanning voor zanderosie, zeespiegelstijging en variaties in sterkte getijstroming als gevolg van zeespiegelveranderingen. Daarbij is aangenomen dat het golfklimaat (hoogte, periode, richting van de golven) onveranderd blijft. Een samenvatting van de resultaten en conclusies in Hoofdstuk 2 tot Hoofdstuk 4 worden hieronder gepresenteerd in de volgende secties.

Effect van formuleringen van bodemschuifspanning, zandtransport en getijdeforcering op de initiële vorming van getijdezandbanken

Uit de resultaten in Hoofdstuk 2 volgt dat de modelformuleringen van bodemschuifspanning en helling-geïnduceerd zandtransport niet kritisch zijn voor de initiële formatie van getijdezandbanken. Bij niet-elliptische getijstromingen zorgt een verhoging van de kritische stroom snelheid voor zanderosie (zie Eq. 2.15) voor een significante verlaging van de groeisnelheid en de golflengte van het voorkeurs-bodempatroon. Behalve getijdezandbanken zijn er ook 'long bed waves' gevonden wanneer de kritische snelheid voor zanderosie iets kleiner is dan de amplitude van de getijdestroomsnelheid. De mate waarin veranderingen in de getij-ellipticiteit de groeisnelheid, de golflengte en de oriëntatie van de kammen van de zandbanken beïnvloeden is niet monotoon. Forcering met een enkeldaags i.p.v. dubbeldaags getij resulteert in een voorkeurspatroon met een langere golflengte en een kleinere oriëntatie hoek, terwijl zijn groeisnelheid nauwelijks veranderd. In het geval van forcering d.m.v een combinatie van een enkeldaags en dubbeldaags getij, of forcering van een dubbeldaags getij met een springtij-doodtij variatie, zijn de karakteristieken van de bodempatronen bepaald door de dominante getijcomponent. De modelresultaten geven ook een mogelijke verklaring voor het feit dat de Nederlandse zandbanken langere golflengtes hebben dan de Vlaamse zandbanken, als gevolg van verschillen in getijstroomkarakteristieken (grootte en ellipticiteit).

Effect van 1D/2D-configuraties, elliptische getijstroming en kritische bodemschuifspanning op de hoogte, vorm en groeitijdschaal van de getijdezandbanken

De resultaten in Hoofdstuk 3 laten zien dat in het geval van een 1D-configuratie, de domein-gemiddelde hoogte h_{rms} van de getijdezandbanken eerst exponentieel groeit en vervolgens verzadigt, d.w.z het systeem bereikt in een statisch evenwicht. Echter, wanneer de configuratie 2D is, blijkt dat in de eindtoestand de kammen van de zandbanken te meanderen in de ruimte en deze meanders fluctueren periodiek in de tijd (dynamisch evenwicht). Initieel bestaan de bodempatronen uit een eindig aantal bodem modes. De meanders ontstaan wanneer de modelconfiguratie bodemmodi toelaat met kammen loodrecht op die van de mode die het initiële voorkeurspatroon bepaalt, en met topografische golfgetallen die van dezelfde orde of kleiner zijn als die van het voorkeurspatroon. Verder moet de gemiddelde verticale afstand tussen de top en dal niveau van de zandbanken groter zijn dan ongeveer 80% van de maximale waterdiepte. Dit percentage wordt kleiner bij toenemende hoogte van windgolven, omdat deze golven zand eroderen van de kammen. In het algemeen is de globale groeitijd, i.e., de tijd waarop h_{rms} stopt met groeien na de exponentiële groeifase van de bodempatronen, iets groter in een 2D dan in een 1D configuratie.

De vormen van deze banken zijn gevoelig voor de getij-ellipticiteit, terwijl ze vrijwel ongevoelig zijn voor de kritische bodemschuifspanning. De globale groeitijd varieert niet monotoon met getij-ellipticiteit, en deze wordt groter wanneer de kritische bodemschuifspanning wordt meegenomen. Vergelijk van de gemodelleerde met waargenomen zandbanken laat zien dat het model de eigenschappen van de Nederlandse banken en de Vlaamse banken in het zuidelijk deelvan de Noordzee kan simuleren en dat deze banken mogelijk nog steeds groeien.

Lange-termijn van getijdezandbanken ander invloed van zeespiegelstijging en variaties in de getijdestroomsnelheid

Gebruikmakend van gegevens uit andere studies m.b.t. gereconstrueerde zeeniveau and gemodelleerde getijstromingen in het gebied van de Nederlandse zandbanken en de Keltische zandbanken. zijn in Hoofdstuk 4 de effecten daarvan op getijdezandbanken onderzocht. De resultaten geven aan dat in het algemeen actieve getijdezandbanken ontstaan wanneer de amplitude van de getijdestroomsnelheid groter is dan 0.5 m/s. Wanneer de zeespiegel sneller stijgt wordt de groeitijd van de zandbanken langer en de blijft hun domein-gemiddelde hoogte h_{rms} meegroeien met het gemiddelde zeeniveau. Een kleinere initiële getij stroom snelheidsamplitude (gedurende de initiële groeifase van de zandbanken) zorgt voor een langere groeitijd, terwijl veranderingen in de dominante stroomrichting een klein effect hebben op de karakteristieken van de banken.

Op de beschouwde tijdschaal (10000 jaar), aannemende dat er een constant golfklimaat is, ontstaan gedeeltelijk actief getijdezandbanken voornamelijk als een gevolg van afnemende getijstroom snelheid amplitudes zodat de effectieve snelheid (wat betreft 'geroerd' zand) kleiner wordt dan de kritische snelheid voor zanderosie (zie Fig. 4.8). De banken worden moribund op een tijdschaal die omgekeerd evenredig is met de snelheid van de zeespiegelstijging. Vergelijk van gemodelleerde met waargenomen zandbanken laat zien dat, in het bijzonder bij de Keltische banken, golflengtes worden onderschat en bankhoogtes worden overschat. In dit kader is het belangrijk om op te merken dat in het model geen afregeling heeft plaatsgevonden en dat de resultaten zeer gevoelig zijn voor de sterktes van getijstroming en door windgolven geïnduceerde erosie van zand.

Vooruitblik

De huidige studie heeft nieuwe inzichten opgeleverd met betrekking tot de initiële vorming en lange-termijn niet-lineaire dynamica van getijdezandbanken. Met betrekking tot toekomstig onderzoek zijn verschillende uitbreidingen mogelijk. Ten eerste behoeft de formulering van golven verbetering; ook moet op tijdschalen van vele eeuwen rekening worden gehouden met veranderingen in het golfklimaat. Ten tweede is het belangrijk om de formulering voor zandtransport uit te breiden; in het model is alleen bodemtransport verdisconteerd, maar voor sterke getijstromingen en fijn zand is ook zwevend stof transport significant. Ten derde is het een uitdaging om de ontwikkeling van bodemvormen in een groter domein te onderzoeken. Daarvoor dient de computationele efficiëntie van het huidige model te worden verbeterd (bv. parallellisatie). Tot slot is het interessant om het huidige model toe te passen op getijdezandbanken in de kustzeeën van China en Australië. Daarnaast kan het huidige model worden gebruikt om het niet-lineaire gedrag van 'long bed waves' te onderzoeken.

总结

在许多拥有沙底的沿海离岸区域，可观测到不同类型有节律的底床地形。这些地形的空间间距（相邻波峰的平均距离）从几米到十几公里不等。其中，潮成沙脊是目前观测到的离岸区域内尺度最大的底床地形。一般情况下，潮成沙脊的空间间距为5–10公里，其高度为5–50米，其波峰线相对于潮流主方向正气旋偏转5°–30°，其演进时间尺度为百年。可观测到这些沙脊的浅海的水深从10米到200米不等。根据当前底床的运动特征，潮成沙脊被归类为“活跃”（沙脊各处都有泥沙输运）、“准活跃”（部分沙脊有泥沙输运）和“衰亡”（无泥沙输运）沙脊。沙脊的形成主要是由于潮汐与底床相互作用，而风浪会影响沙脊的形态；此外，海平面上升和潮流条件的变化也会影响沙脊的长期演进。对许多实际问题而言，如海沙挖掘的策略规划、海洋生态系统平衡的维持及水下结构稳定性评估，获取更多关于上述地形的动力学知识十分必要。

目前已有一些针对潮成沙脊的线性和非线性动力学的研究，然而仍有一些方面值得进一步探索，文献回顾引出了本文的三个研究问题。第一个问题（见第一章第1.5节的研究问题一）涉及到这些地形的初始形成，尤其是不同底床剪应力公式、不同泥沙输运公式、潮汐椭率和不同潮汐分量对地形初始形成特征（初始最速生长模态的生长率、间距、偏向）的影响。第二章对该问题进行了解答。

关于潮成沙脊的非线性演进的一些方面也尚未被探索（见第一章第1.5节的研究问题二）。这些方面涉及有限高度沙脊的特征（形态及生长时间）对一维和二维地形（地形在水平面上单向和两向变化）、潮汐椭率和泥沙输运的临界剪应力的敏感性。第三章研究了上述问题，其中海平面和潮汐条件被设定为不随时间变化。

实际情形下，在潮成沙脊的演进时间尺度上，海平面和潮汐的特征都会改变，然而这些变化如何影响沙脊的演进尚不明确（见第一章第1.5节的研究问题三）。在第三章的基础上，第四章研究了海平面和潮流流速幅值及主方向的变化对活跃沙脊生长时间和高度的影响。此外，第四章还探索了海平面上升和潮汐变化在活跃沙脊演变为准活跃／衰亡沙脊的过程中所扮演的角色。

为增进上述关于潮成沙脊初始形成和长期演进方面的理解，本文开发并运用了一个理想的非线性地貌动力数值模型。该模型描述了一个浅海离岸区域中在潮汐作用下水深平均的水流与可侵蚀沙底相互耦合的系统。与前人模型相比，该模型具有多个优点。具体而言，当前模型考虑了水平二维地形、可由多个潮汐分量构成的椭

圆潮流、泥沙输运的临界剪应力、海平面上升和潮汐变化。以下三小节分别总结了第二到第四章的结果和结论。

一. 不同底床剪应力公式、泥沙输运公式、潮汐力对潮成沙脊初始形成特征的影响

第二章的研究结果表明，对于潮成沙脊的初始形成，底床剪应力公式和底坡引起的输沙并不关键。在直线往复潮流作用下，增大输沙的临界流速会减小初始最速生长模态的生长率和间距。当输沙的临界流速稍小于潮流的流速幅值时，除潮成沙脊外，长底床波也会出现。 沙脊的初始生成特征（生长率、间距、偏向）对潮汐椭率的依赖性是非单调的。减小分潮的频率，沙脊的间距变大，偏向角变小，而生长率基本不变。 在多个潮汐分量的作用下，底床特征由主要潮流分量确定。本文模拟结果还给出了位于北海南部的荷兰沙脊（Dutch Banks）比佛兰芒沙脊（Flemish Banks）间距大的可能原因。

二. 水平一维和二维地形、椭圆潮流和输沙临界剪应力对有限高度的潮成沙脊的影响

第三章的结果显示，一维地形下，初始时沙脊的均方根高度h_{rms}呈指数增长。最终沙脊达到静态平衡，即h_{rms}不再随时间变化。相比而言，二维地形下，沙脊波峰线可能呈蜿蜒状，且随时间变化。初始时，地形是由有有限个底床模态（傅立叶模态）构成。蜿蜒沙脊出现的条件是存在波峰线与初始最速模态波峰线相交的底床模态，且这些底床模态的波数近似于或小于初始最速模态的波数；此外，沙脊的高度（波峰波谷间的垂向距离）需占最大水深的80%以上。大体而言，二维情形下的全局增长时间τ_g（从初始到h_{rms}停止指数增长的时间间隔）比一维情形下的稍大。

沙脊的剖面形状对潮汐椭率较敏感，而对泥沙输运的临界剪应力并不敏感。沙脊的全局增长时间τ_g随潮汐椭率非单调变化，考虑泥沙输运的临界剪应力时的τ_g比不考虑时要大。 与现场观测的潮成沙脊相比，模拟结果可体现北海南部沙脊的总体特征，结果还显示这些沙脊可能仍在生长。

三. 海平面上升和潮汐变化对有限高度的潮成沙脊的影响

第四章的结果显示，一般情况下，活跃潮成沙脊出现在潮流流速幅值大于0.5m/s的区域。对这些沙脊而言，海平面上升速率增大时，沙脊的全局增长时间

变长，均方根高度持续增长。潮流流速幅值相对较小时，全局增长时间较大，而潮流主方向的变化对沙脊的特征影响不大。

在本文考虑的时间尺度下，如波浪条件不变，准活跃潮成沙脊的主要成因是潮流流速幅值的减小，以至于有效流速（从搅动泥沙的意义上）变得比输沙的临界流速小。随着海平面的上升，这些沙脊会进一步变成衰亡沙脊，该过程的时间尺度与海平面上升的速率成反比。模拟的潮成沙脊与观测的沙脊相比有许多相似的特征。对于模拟与观测结果之间定量的差异，本文也给出了详尽的解释。

ACKNOWLEDGMENTS

Time flies. Back to 2012, at that time I had no idea how life would be for someone doing their PhD in a foreign country. After more than four years of working in the Netherlands, I am glad to have a thesis in the present form, while I have to say that it was not an easy job. Here I would like to thank these people, my supervisors, my family and friends, whose support made it possible for me to finish the PhD.

Huib, thank you for accepting me as a 'halfway' PhD at the beginning of 2014. You patiently guided me into the world of rhythmic bedforms in shelf seas and offered me many opportunities to be on track quickly. Your enthusiasm in teaching, critical thinking in research and rigorousness in writing and presenting impressed me a lot, and will have a long-term positive impact on my career. Although we did have conflicts several times, especially in terms of writing and presenting, we managed to reach agreements and solve the problems. Also thank you for your warm welcome and your kindness in arranging traffic cards and bicycles when I arrived at the Netherlands. I appreciate that a lot.

Leo, thank you for giving me a chance to do a PhD in Utrecht. Your passion on discovering internal waves in nature inspired me. It is quite some travel from Texel to Utrecht, but you arranged a meeting for me in Utrecht almost every week. Thanks a lot for your understanding and your kindness to give me suggestions when I decided to make a 'detour' during the PhD. It was a pity that the new type of equipment you proposed for reconstructing the flow for internal waves in the field did not become real. I hope you can build the equipment in the future.

Carles, as a supervisor and a friend, it is really great to have you here in Utrecht. Thank you for sharing your valuable ideas during work. I enjoyed the Catalan culture, the dish and rice you brought here, and most importantly, the time I spent with the Catalan friend. Speaking of colleagues who works/worked in the Catalan region (in Universitat Politècnica de Catalunya, UPC), I would like to thank Daniel, Roland, Francesca, Àngels and Jaime as well. Daniel and Roland, thank you for developing the 'Morfo' program which is the basis of the model I used in this thesis, albeit the language of the comment lines in the program is a mixture of English, Catalan and French. Daniel, thank you for making the program run with a proper compiler. Also thank you all for your warm welcome during my short stay in UPC.

Thank you, dear members of IMAU coastal group. Niels, it was really nice of you to pick up Wei, Bo and me on the first day we arrived at the Netherlands, and also to help us with moving within Utrecht later. Thanks a lot for your help and you kindness, and I appreciate your positive feedbacks on my work during the group meetings. Abdel, thanks for introducing me to the IMAU running group when I came

here and inviting me to the ‘tea break’. Also thanks for your guidance in the model Morfo56. Wim, you (and Niels) are always active in the group meetings and never hesitate to share your opinions, which impresses me and inspires me to think and speak more. You also gave me a big favor to let me use server, which shortened the time to finish the thesis enormously. Erik, thank you for sharing a few tips in using programming languages and computers. It is nice to have you as an office mate, as well as some imaginary/real animals you drew, like the puzzled penguin in a piece of jigsaw puzzle on the drawing board (still there when I wrote this down). Bo and Wei, thank you very much for your company during the last few years. We had great times in sharing food, traveling, chatting etc. Also thanks for your feedbacks on my work. Klaas, thank you for sharing ideas in the 3D model for offshore bedforms. Caption Tjebbe, thank you for inviting me to the sailing trip on the boat ‘Gudsekop’. It was really a nice experience to go with the wind in spring. Miguel, Konstantinos and Stavros, it was great to play basketball together with you guys. Those times add lots of fun to my PhD life.

Thank you, my dear office mates Aimée, Malou, Claudia and André. Aimée and Malou, thank you for your warm welcome and help when I came to the room 664, and thanks for your tolerance and kindness to let me stay. Claudia, thank you for your invitations to enjoy the nice sunset from our window and to bicycle trips. Also thanks for sharing music and all kinds of stories. André, thanks for making the office more lively by bringing more penguins (bookmarks) from Antarctic and more plants to create a jungle in the office. Also thank you for checking almost every morning if I am fine during the days of wrapping up the thesis. Here, I would also like to thank many other people, Joseph, Dewi, Maria, Lisa, Alex, Erik (Mulder), Daniele, Michael, Sudhanshu and other IMAUers, your company enriches my life.

谢谢殷樽、綮一、陈炜、顾昕、康明、东龙等友人，你们为我在这里的生活添加了许多色彩和中国元素。最后，谢谢刘博在这几年的陪伴，也谢谢我的父母和姐姐在远方的理解和支持。

CURRICULUM VITAE

Bing Yuan

- 2014.02-2017.07: PhD research, Utrecht University.
  - Supervisor: Prof. dr. H.E. de Swart.
  - Subject: Modeling the dynamics of large-scale bedforms in shelf seas.
- 2012.10-2014.02: PhD research, Utrecht University.
  - Supervisor: Prof. dr. L.R.M. Maas.
  - Subject: Internal waves.
- 2009.09-2012.03: Master in Fluid Mechanics, Tianjin University.
  - Supervisor: Prof. dr. Jianhua Tao.
  - Subject: Finite volume model for coupled surface and subsurface flow.
- 2005.09-2009.07: Bachelor in Engineering Mechanics, Tianjin University.
  - Supervisor: dr. Jian Sun.
  - Subject: Analysis of tidal harmonic constants and its application.
- 1987.09: Born in Xiaogan, Hubei province, China.

This document was typeset using `classicthesis` developed by André Miede.